Nanostructured polymer- and metal surfaces

Antireflective and colour functionality

Christiansen, Alexander Bruun

Publication date:
2014

Document Version
Publisher's PDF, also known as Version of record

Technical University of Denmark

Nanostructured polymer- and metal surfaces

Antireflective and colour functionality

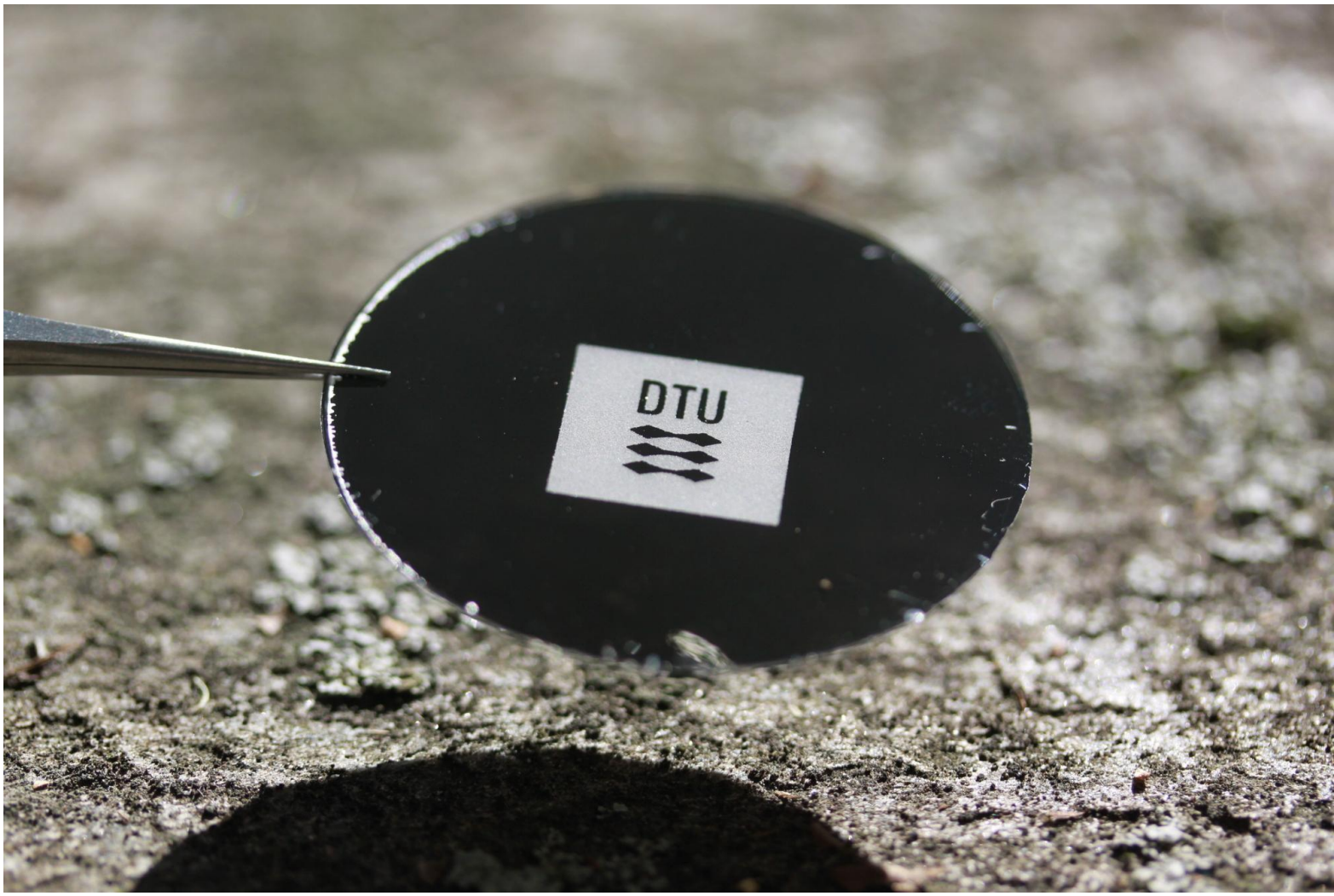

Alexander Bruun Christiansen

Ph.D. Thesis

March 2014

Supervisors:
Prof. Anders Kristensen, DTU Nanotech
Prof. N. Asger Mortensen, DTU Fotonik

DTU Nanotech
Department of Micro- and Nanotechnology

Abstract

This Ph.D. thesis explores the optical properties of nanostructured dielectric and metallic surfaces. Focusing on scalable fabrication methods for antireflective nanostructures, this experimental study has resulted in the proof of concept of inexpensive, large area antireflective nanostructures, as well as structural enhancement of light absorption in thin metal films, deposited on nanostructured substrates.

Large areas of nanostructures were realized using the black silicon (BSi) method: a mask less reactive ion etching process, resulting in tapered nanostructures with tunable dimensions, on wafer scale. The BSi structures were replicated into the UV curable organic-inorganic hybrid polymer Ormocomp, in order to further assess the optical properties of the structures. BSi structures with lateral dimensions of around 1 μm would selectively scatter specific bands of wavelengths, resulting in a structural colour filter for specularly transmitted light.
By reducing the height and lateral size, the structures enter a regime where scattering of visible light becomes insignificant. In this regime, the BSi structures were shown to be antireflective. An empirical relation between the characteristic length scale of the nanostructured surface, and the wavelength at which scattering becomes significant, was shown. The result is thus a design criterion for the use of random nanostructures for non-scattering antireflective surfaces.

Antireflective BSi nanostructures were fabricated using injection moulding in polypropylene. A Ni shim was electroplated from a BSi master, and inserted in an injection moulding tool. The reflectance of the injection moulded parts was reduced from 4.5 % to 2.5% in the visible spectrum. The reflectance was calculated from the gradient in the refractive index from AFM data, using effective medium theory, and the measured and theoretical reflectance showed good agreement.

Binary antireflective nanostructures were fabricated in Ormocomp by replication from a Si master which was patterned using fast e-beam lithography. The reflectance was decreased from 4% down to 1%.

Finally, the optical properties of thin metal films deposited on nanostructured surfaces was studied. When a metal film was deposited on BSi structures in Ormocomp, the reflectance of the metal film was lowered significantly, and the absorption was increased. In contrast to their reflective planar counterparts, these thin metal films appear completely black. Two effects causing the increased absorption were suggested: a gradient effect, causing the metal film to be antireflective, and that the structured surface allows for coupling to surface plasmons in the metal film.

Resumé

Denne Ph.d.-afhandling undersøger de optiske egenskaber for nanostrukturerede dielektriske og metalliske overflader. Med fokus på skalérbare metoder til fabrikation af antireflekterende nanostrukturer, har dette eksperimentelle studie resulteret i proof-of-concept af billige antireflekterende strukturer på store arealer, samt strukturel forøgelse af absorption af lys i tynde metal film, deponeret på nanostrukturerede substrater.

Nanostrukturer over store overflader blev fremstillet ved af Black Silicon (BSi) metoden: en umaskeret reaktiv ion æts, som resulterer i tilfældigt orienterede, spidse nanostrukturer med justerbare dimensioner. Disse BSi strukturer blev replikeret i det UV hærdende materiale Ormocomp, for at kunne karakterisere de optiske egenskaber af nanostrukturerne. BSi strukturer med laterale dimensioner omkring 1 μm viste kraftig spredning af lys, og virkede som strukturelle farve-filtre for direkte transmitteret lys. Ved at reducere strukturernes laterale strørrelse, kunne spredning af lys fra overfladen mindskes til et insignifikant niveau. I dette regime virkede BSi strukturerne antireflekterende. En empirisk relation mellem nanostrukturernes karakteristiske længde-skala, og den bølgelængde hvorved lys begynder at blive spredt, blev vist. Dette resultat giver således et designkriterie for brugen af tilfældige nanostrukturer til ikke-spredende antireflekterende overflader.

De antireflekterende BSi nanostrukturer blev også fremstillet i en sprøjtestøbe process. En Ni shim blev elektroplateret fra en BSi skive, og brugt som indsats i en sprøjtestøbe form. Reflektansen af de sprøjtestøbte emner blev reduceret fra 4.5% til 2.5% i det synlige spektrum. Reflektansen blev beregnet fra gradienten i det refraktive index vha. effektiv medium teori, baseret på data fra atomic force mikroskopi. Den målte og beregnede reflektans viste god overensstemmelse.

Binære antireflekterende strukturer blev fremstillet i Ormocomp, ved replikation fra en Si skive, som blev struktureret vha. hurtig elektronstråle litografi. Reflektansen blev reduceret fra 4% ned til 1% i det synlige spektrum.

De optiske egenskaber af tynde metal film deponeret på nanostrukturerede overflader blev undersøgt. Når en metal film blev deponeret på BSi nanostrukturer i Ormocomp, blev reflektansen mindsket voldsomt, og absorptionen forøget. I modsætning til plane metal film, fremstod disse nanostrukturerede metaloverflader helt sorte. To effekter som forårsager den forøgede absorption blev foreslået: en gradient effekt som mindsker reflektansen fra overfladen, samt at den strukturerede overflade tillader lys at koble til overflade-plasmoner i metallet.

Preface

This thesis is submitted in partial fulfilment of the requirements for obtaining the Philosophiae Doctor (Ph.D.) degree at the Technical University of Denmark (DTU). The work presented here has been carried out at the Department of Micro and Nanotechnology (DTU Nanotech) in the Optofluidics group and in the DTU Danchip clean-room facilities.

The project was supervised by Prof. Anders Kristensen to whom I am grateful for his continued enthusiasm and support during the last three years. A great deal of what I have learned about science and innovation, I owe to him and my co-supervisor N. Asger Mortensen. I would like to thank my colleagues in the Optofluidics group, both present and former, who have always been happy to share their vast knowledge about clean-room fabrication, optics, and life in general. I am particularly thankful for the motivational support of my office mate Pétur G. Hermannsson. I am also thankful for having had the opportunity to supervise Toke Tobiasen, and Gideon P. Caringal, and George, Ben, Elwin, Matthew, and Michael from University of Waterloo, Canada.

I would like to thank my colleagues at DTU Nanotech and Fotonik with whom I have shared many interesting conversations and festive moments, and the always professional and helpful staff at Danchip, for having (almost always) allowed me to pursue my ideas.

Throughout the project I have enjoyed the company and close collaboration with my fellow Ph.D. students, Jeppe S. Clausen, Emil Højlund-Nielsen, and Emil Søgaard. I would also like to thank the industrial partners in both Nanoplast and Plast4Future. The collaboration, and continued interest from these partners was a great motivation throughout the project. I also owe my thanks to the skilled metrologists at DFM, and the groups of Ole Sigmund and Rafael Taboryski.

I gratefully acknowledge the Danish National Advanced Technology Foundation for funding the PhD project via the NanoPlast project, and Otto Mønsted Fonden for financial support for travels.

I thank my family and friends for still being there, despite my utter neglect for the last three years. Finally I would like to thank Claudia Caviglia - I am happy that we could share our time as Ph.D. students, and I look forward to our future endeavours.

Alexander Bruun Christiansen
31 March 2014

List of publications

Journal papers

- Jeppe Sandvik Clausen, **Alexander Bruun Christiansen**, Jørgen Garnæs, Niels Asger Mortensen, and Anders Kristensen.
  Color effects from scattering on random surface structures in dielectrics, Opt. Express, vol. 20, no. 4, pp. 4376-81, Feb. 2012.
  Contribution: Design of experiment, fabrication, characterization, optical measurements, and writing the manuscript.

- **Alexander Bruun Christiansen**, Jeppe Sandvik Clausen, Niels Asger Mortensen, and Anders Kristensen.
  Minimizing scattering from antireflective surfaces replicated from low-aspect-ratio black silicon, Appl. Phys. Lett., vol. 101, no. 13, p. 131902, 2012.
  Contribution: Design of experiment, fabrication, characterization, optical measurements, analysis and writing the manuscript.

- **Alexander Bruun Christiansen**, Jeppe Sandvik Clausen, Niels Asger Mortensen, and Anders Kristensen.
  Injection moulding antireflective nanostructures, Accepted for publication in Microelectron. Eng.
  Contribution: Design of experiment, fabrication, characterization, optical measurements, analysis and writing the manuscript.

- **Alexander Bruun Christiansen**, Gideon Peter Caringal, Jeppe Sandvik Clausen, Niels Asger Mortensen, and Anders Kristensen.
  Black metal thin films by moth-eye nanostructures, manuscript in preparation.
  Contribution: Design of experiment, fabrication, characterization, optical measurements, analysis and writing the manuscript.

- **Alexander Bruun Christiansen**, Jeppe Sandvik Clausen, Emil Højlund-Nielsen, Niels Asger Mortensen, and Anders Kristensen.
  Binary antireflective nanostructures, manuscript in preparation.
  Contribution: Design of experiment, fabrication, characterization, optical measurements, analysis and writing the manuscript.

Conference proceedings

- **Alexander Bruun Christiansen**, Emil Højlund-Nielsen, Jeppe Sandvik Clausen, Gideon Peter Caringal, Niels Asger Mortensen, and Anders Kristensen. *Imprinted and injection-molded nano-structured optical surfaces*, in Proc. SPIE 8818, Nanostructured Thin Films VI, 2013, vol. 8818, p. 881803.
  Contribution: Section 3: antireflective nanostructures, and section 5: angle-dependent color effects by diffraction grating pixels.

Conference contributions

- **Alexander Bruun Christiansen**, Jiri Cech, Anders Kristensen, Rafael J. Taboryski. *Fabrication of nanostructures on double-curved PMMA surfaces by thermal imprint with PDMS stamp*, poster presented at The 55th International Conference on Electron, Ion, and Photon Beam Technology and Nanofabrication, Las Vegas, Nevada, USA (2011).

- **Alexander Bruun Christiansen**, Jeppe Sandvik Clausen, Emil Højlund-Nielsen, Niels Asger Mortensen, and Anders Kristensen.
  Large area color effects in polymer replica of black silicon, poster presented at The 10th International Conference on Nanoimprint and Nanotechnology (NNT), Jeju, South Korea (2011).

- Jiri Cech, **Alexander Bruun Christiansen**, Rafael J. Taboryski.
  Stamp deformation during nanopattern thermal imprinting on a double-curved substrate, poster presented at 37th International Conference on Micro and Nano Engineering (MNE), Berlin, Germany (2011).

- **Alexander Bruun Christiansen**, Jeppe Sandvik Clausen, Niels Asger Mortensen, and Anders Kristensen.
  Antireflective nanostructures replicated from black silicon, poster presented at the International Symposium on Nanoscale Pattern Formation at Surfaces, Copenhagen, Denmark (2013).

- **Alexander Bruun Christiansen**, Jeppe Sandvik Clausen, Niels Asger Mortensen, and Anders Kristensen.
  Injection moulding antireflective nanostructures, poster presented at The 39th International Conference on Micro and Nano Engineering (MNE), London, Great Britain (2013).

- Emil Højlund-Nielsen , Jeppe Sandvik Clausen, **Alexander Bruun Christiansen**, Tine Greibe, Niels Asger Mortensen, and Anders Kristensen.
  Fast-writing E-beam for large arrays of nano-holes, poster presented at The 39th International Conference on Micro and Nano Engineering (MNE), London, Great Britain (2013).

Patents

- **Alexander Bruun Christiansen**, Anders Kristensen, and Niels Asger Mortensen, *A nanostructured surface for grey scale colouring*, DK Patent Appl. No. PA 2013 70657. Published 12 Nov 2013.

- Jeppe Sandvik Clausen, Niels Asger Mortensen, Anders Kristensen,Emil H]øjlund-Nielsen, Claus Jeppesen, and **Alexander Bruun Christiansen**, *CONFIDENTIAL TITLE*, EP Patent Appl. No. 13182666.1. Not yet published.

Other relevant publications

- Jeppe Sandvik Clausen, **Alexander Bruun Christiansen**, Anders Kristensen, and Niels Asger Mortensen.
  Enhancing the chroma of pigmented polymers using antireflective surface structures, Appl. Opt. 52, 7832-7837 (2013).
  Contribution: Design and fabrication of antireflective Si masters.

Contents

List of abbreviations

ABS	acrylonitrile butadiene styrene
AFM	atomic force microscope
APA	anodic porous alumina
AR	antireflective
BSi	black silicon
COC	cyclic olefin copolymer
EBL	electron-beam lithography
EMT	effective medium theory
FDTS	perfluorodecyltrichlorosilane
MVD	molecular vapour deposition
NIL	nano imprint lithography
NSOM	near-field scanning optical microscope
PDMS	polydimethylsiloxane
PMMA	poly(methyl methacrylate)
PP	polypropylene
PSD	power spectral density
RCWA	rigorous coupled-wave analysis
RIE	reactive ion etching
SEM	scanning electron microscope
SPP	surface plasmon polariton
TEM	transmission electron microscope
UV	ultraviolet

1
Introduction

1.1 Introduction

1.1.1 Technological background

While mankind has only recently discovered the possibilities of nanostructured materials, the astounding effects that nanostructures can have on e.g. surface properties have been utilized by nature for a long time. This became clear to scientists in the 1960s, as a result of the advances within electron microscopy. With the dramatic increase in resolving power, the scientists could go beyond the diffraction limit of optical microscopes, and found that there was indeed plenty of room at the bottom. They found vast arrays of nanostructures on the eyes of moth, intricate three-dimensional formations on the scales of butterfly wings, and complex, hierarchical micro- and nanostructures on the leaves of the lotus flower. But how do these insects and plants benefit from nanostructures? And how can human beings learn from them, for our own advantage? In the next few pages, some of the properties of nanostructured surfaces will be introduced, along with the scope of this thesis.

Antireflective nanostructures

In 1962 Bernhard and Miller[1] reported the finding of arrays of nanostructures with a period of around 200 nm, on the cornea of several types of moth, butterflies, and flies. In 1967 Bernhard further investigated these structures (See Fig. 1.1 (a)), and used up-scaled models and microwave illumination to show that the structures worked to reduce the reflectance of light from the cornea surface[2]. In 1973 Clapham *et al.* showed the first artificially fabricated moth-eye structures, using laser-interference lithography. From modelling they showed the relation between reflectance and the normalized height of the structures, d/λ, with d being the height of the structures, and λ the wavelength of the light. The curve is shown in Fig. 1.1 (b). A critical feature of such structures is that the period of the array has to be below around 200 nm in order to avoid diffraction - such structures are generally referred to as sub-wavelength structures.

Structural colours

Some insects also rely on nanostructures to create vivid colours. Most famous is the Morpho butterfly with its characteristic blue colour, which is shown in Fig. 1.2 (a)[4;5]. The high reflectivity and angle independent colour is enabled by nanostructures which resemble Bragg mirrors, as seen in Fig. 1.2 (b). The periodicity of the lamellar structures provide the

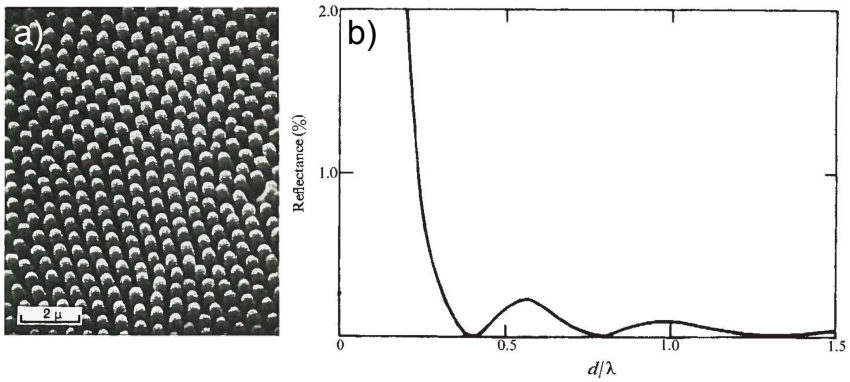

Figure 1.1: Antireflective moth-eye structures. a) Scanning electron microscope (SEM) image of the nanostructures on the eyes of a night moth. From Bernhard[2]. b) Calculated reflectance of moth-eye nanostructures as function of d/λ. From Clapham *et al.*[3].

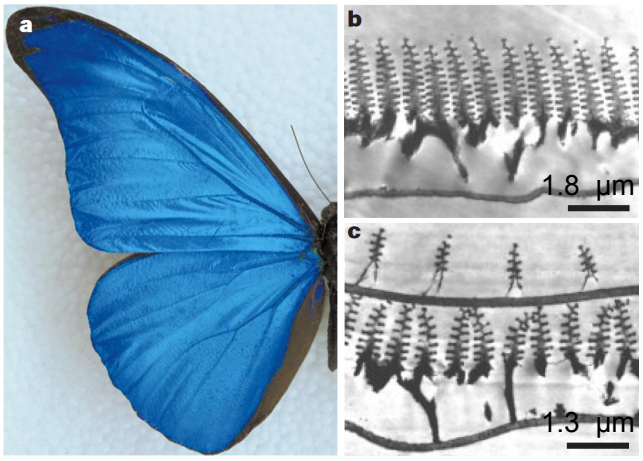

Figure 1.2: Structural colours in butterfly wings. a) Photograph of the Morpho Rhetenor wing. b-c) Transmission electron microscope (TEM) images, showing cross sections of the wing scales. The lamellar structure work as Bragg mirrors, reflecting only blue wavelengths of light. The structural variations act to diffuse the reflected light, giving the wing a homogeneous blue colour, independent of viewing angle. The figure is from Vukusic *et al.*[5].

blue colour, while small variations in the structures act to diffuse the reflected light and give an almost angle independent colour.

The field of structural colours goes back to Hooke (1665) and Newton (1730) who studied the structural colours of insects and peacock feathers. Later Rayleigh (1888) shed light on the physical mechanisms behind the phenomena, and the field is still very much alive[6–10].

Metal nanostructures

In recent years the progress has moved beyond just mimicking nature, and started venturing into whole new areas of nanotechnology. While insects are restricted to using organic materials, scientists have begun to investigate also the properties of metallic nanostructures. This has lead to the scientific fields of plasmonics and meta materials.
A famous example of the surprising effects of plasmonics was the discovery of extraordinary optical transmission through sub-wavelength hole arrays[11]. The observed transmittance

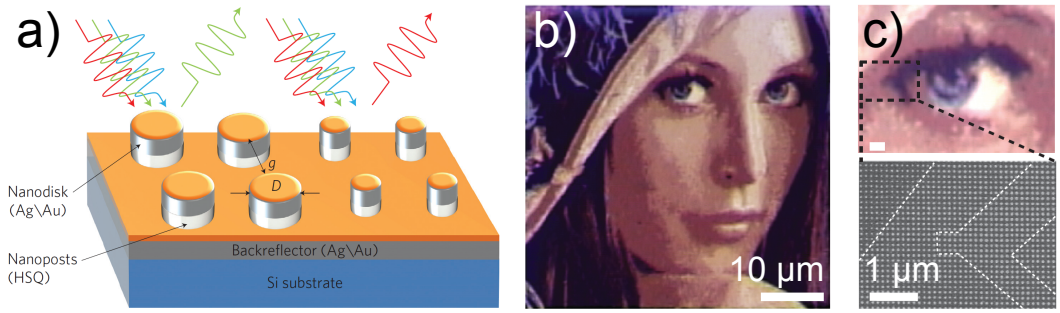

Figure 1.3: Plasmonic structural colours. a) Sketch of the principle of plasmonic colours. Metal is deposited on an array of nano pillars of different dimensions. Localized surface plasmons can be excited in the resulting metal disc on top of the pillars. The resonances can be controlled by varying the dimensions of the discs. b) Optical micrograph showing different colours, from nanodiscs of varying dimensions. c) Comparison of the visual effect in an optical microscope (top), and a scanning electron micrograph of the nanodisc array (bottom).

was orders of magnitude higher than expected from standard aperture theory. The surprising phenomenon was explained by the coupling of light with plasmons in the surface of the nanostructured metal film.

A recent advance in plasmonic structural colours was shown by Kumar *et al.*[12], where a surface of metal discs of 20 nm thickness, and diameters of 50-100 nm act as dipoles that only absorb specific wavelengths of the incoming light, while the other wavelengths are allowed to propagate or be reflected. The result is a way of controlling the colour of the reflected light, as shown in Fig. 1.3. The colour of the surface can be controlled by varying the sizes of the nanodiscs, enabling pixel sizes of down to 250×250 nm^2.

Metals are especially interesting as they are great light absorbers, but at the same time, highly reflective. This gives a potential for dramatic changes in the optical properties of metal surfaces by nanostructuring. Nanostructures can decrease the reflectance of metal films, and consequently increase the absorbance, and can allow coupling between the incoming light and surface plasmons in the metal. Figure 1.4 shows a 100 nm thick aluminium film, deposited on a structured substrate. Instead of the mirror-like surface of planar metal films, the surface appears black and white. The dark areas are nanostructured, which decreases the reflectance of the surface, and increases the absorbance. The white area of the DTU logo is microstructured, giving a high, diffuse reflectance. This shows the dramatic effects that surface structures can have on thin metal films - a phenomenon which will be discussed in this thesis.

Moth-eye structures in commercial products

The nanostructures introduced above are not used in many commercial products today, mainly due to high production costs. There are however examples of the use of moth-eye antireflective (AR) nanostructures in some commercially available products.

Canon is using moth-eye structures in their EF 24 mm f/1.4L II USM lens[13;14], based on the formation of a porous aluminium oxide[15] layer on the inside of the first optical element of the lens (See Fig. 1.5 (a)). The wide angle lens requires a very high curvature of the lens, resulting in high incident angles of the incoming light. Maintaining a low reflectance for a wide range of incoming angles is hard to achieve using conventional thin film coatings, but is one of the advantages of the moth-eye nanostructures. The lens is a high-end product with a retail price in Denmark of around €1600 (March, 2014).

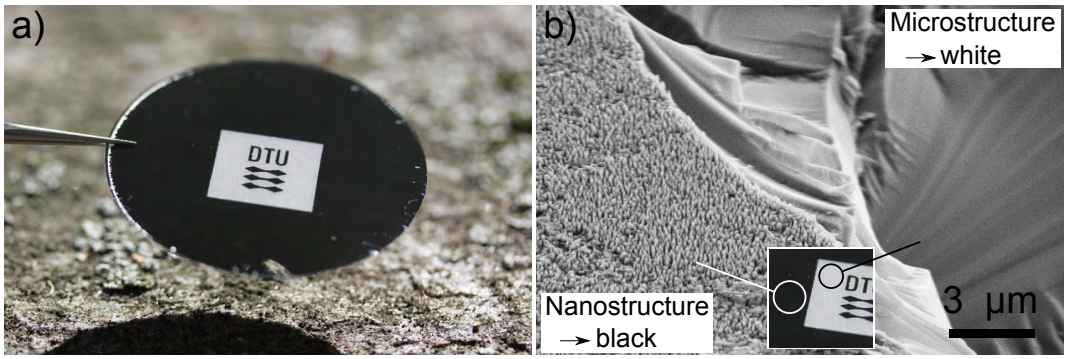

Figure 1.4: Absorbing metal thin film. a) Photo of a 100 nm Al film deposited on a structured dielectric substrate. The dark areas are nanostructured, while the white area of the DTU logo is microstructured. b) SEM image of the Si master used to cast the substrate. The nanostructured area is seen on the left, and the microstructured area is seen on the right. The nanostructures are formed by black silicon reactive ion etching. The microstructures are formed by powder blasting of the Si master.

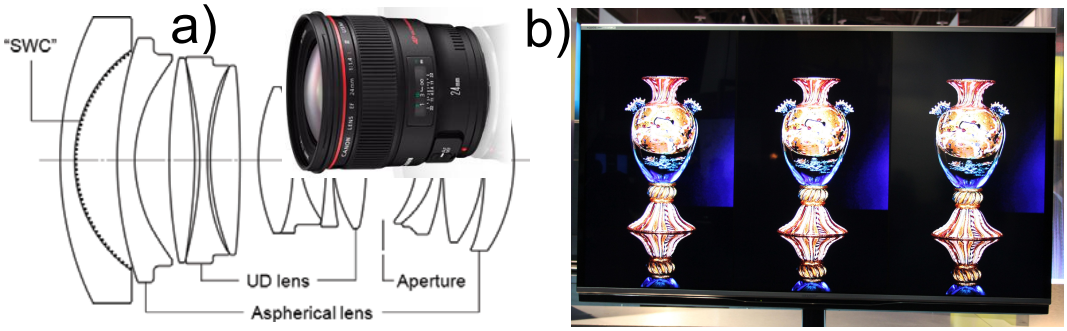

Figure 1.5: Products using moth-eye antireflective nanostructures. a) Diagram of the EF 24 mm f/1.4L II USM lens from Canon[14]. Moth-eye nanostructures are used on the inside of the first lens element. b) Prototype for display using moth-eye nanostructures to suppress reflections. Left side is a normal screen, right side is a matte screen, and the moth-eye screen is in the center. Images are from Brunner *et al.*[14], www.canon.dk, and www.clubic.com.

Displays that implement moth-eye technology have also appeared in recent years. A prototype from the Japanese company, Sharp is shown in Fig. 1.5 (b). In 2010 Sharp filed a patent on a moth-eye technology, which mentions the use of an anodized porous aluminia mould for fabrication of moth-eye structures[16].

1.1.2 Motivation

The properties discussed in the previous section could be very beneficial in many products, providing new functionalities, and new ways of decorating products. However, nanostructure fabrication is expensive, and industrial production is limited to a few industries, such as the microelectronic industry, and the DVD and Blu-ray industry. Both use highly specialised techniques that are not readily transferred to other products.

This thesis is motivated by the idea that nanostructured plastic parts can be produced by injection moulding, which is a high volume production method used for the production of almost all plastic parts today[17]. Injection moulding works by injecting a molten polymer under high pressure, into a cavity which forms the plastic part. The cavity can then be

opened, and the finished part removed. The idea is then to form nanostructures inside the injection moulding tool cavity, so the structures are transferred to the parts during moulding. In this way nanostructures can be fabricated inexpensively in large volumes[18;19].

This thesis is part of the project Nanoplast funded by the Danish National Advanced Technology Foundation[1]. The scope of the Nanoplast project is to combine the competences of Danish injection moulding companies, with the expertise in nano fabrication of DTU and NIL Technology. The vision of the project is *"to develop and implement a technology that enables the use of nanostructured surfaces on injection molded plastic components"*. A similar project, Plast4Future[2], includes also European partners such as Fiat and Maier, and the aim is towards the automotive industry. The scope of both projects is to add value to injection moulded parts by implementing some of the functionalities stated in the previous section.

The scope of this thesis is to provide proof of principle nanostructures, which can potentially be implemented in injection moulding tools, to add optical functionality to injection moulded parts.
The ultimate goal of the project is to eliminate the need for post-treatment of injection moulded parts, like pad printed decorations, and instead provide the decoration effects via nanostructures in the injection moulding tool, which are transferred to the plastic parts during moulding.
This would simplify the production, and make it easier to recycle the polymer, as there would be no paint added to the surface of the plastic parts. This paint would otherwise pollute the polymer material during recycling. Furthermore, if colour effects could be supplied by nanostructures, the need for many different colours of polymer, and paint could be omitted, which would simplify the supply chain. Colours would instead be controlled by the structuring of the moulds.

Apart from designing the structural functionalities of nanostructured surfaces, a large part of the Nanoplast project is devoted to enable nanostructuring of the mould used in the injection moulding industry. Here there are three main challenges. The surface roughness of the steel typically used for moulds is much larger than the size of the nanostructures. In order to structure the moulds, the surface roughness needs to be improved significantly, ideally to be similar to that of a Si wafer. The efforts here include polishing, plating, and coating of the steel surfaces, in order to planarize the rough surfaces.

Second, a nano imprint lithography (NIL) process for transferring the patterns from silicon masters and into the steel moulds has to be developed. The nanostructures are transferred from the Si master into a flexible mould of e.g. cyclic olefin copolymer (COC). The planarized steel mould is coated with a resist using spin- or spray coating, and the pattern is imprinted in the resist. The pattern is then transferred to the steel tool using a physical etching technique.

And third, the structures should be able to be transferred to free-form moulds, including double-curved surfaces. The coating of these surfaces is done by spray coating, and the pattern transferral is achieved by the flexible COC mould. The deformation in the patterns which will occur when the planar mould has to conform to the double curved surfaces, can

[1] www.nanoplast.dk
[2] www.plast4future.eu

potentially have a high impact on the functionality of the structures. For optically functional structures, even very small variations in e.g. the period of the structures can significantly change the effect. Efforts are here being taken in numerically modelling these deformations, with the goal of enabling an inverse mapping of the structure in the final mould, related to how the structures have to be designed on the planar Si master.

1.2 The state of the art

The following section will provide some insight in the state of the art of AR surfaces and nanostructured metal surfaces. For the antireflective surfaces, the focus will be on structures fabricated by scalable methods like black silicon (BSi), anodic porous alumina (APA), and laser interference, while distinguishing between period and random structures. Good reviews of the field of AR nanostructures can be found in Raut *et al.* [20] and Brunner *et al.* [14].

1.2.1 Random AR nanostructures

In 2008 Ting *et al.* reported antireflective structures in poly(methyl methacrylate) (PMMA), fabricated by hot embossing with a Ni-Co stamp [21]. The high aspect ratio structures were fabricated in Si using electron cyclon resonance etching (Fig. 1.6 (a)), and the Ni-Co shim was subsequently electroplated from the Si master. The structures were hot embossed into 2 mm thick PMMA substrates (Fig. 1.6 (b)). The measured reflectance was below 0.5% in the visible spectrum for structures with aspect ratio higher than 2.5. The average distance between the structures was approximately 150 nm. The antireflective effect is displayed in (Fig. 1.6 (c)).

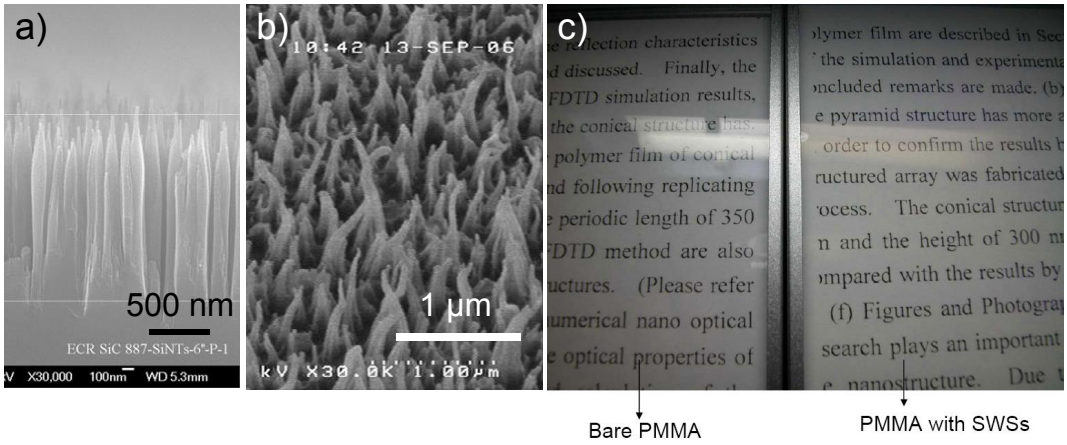

Figure 1.6: Antireflective structures from Ting *et al.* [21] a) SEM image of BSi master fabricated by electron cyclon resonance. b) SEM image of AR structures in PMMA. The structures were replicated from the BSi structures by electroplating a Ni-Co mould and hot embossing in a 2 mm thick PMMA substrate. c) Photo of specular reflection from a lamp in planar PMMA (left) and nanostructured PMMA (right).

In 2010 Hong *et al.* [22] reported the fabrication of antireflective nanostructures in COC by hot embossing from a BSi master. After hot embossing the master was dissolved, as it was not possible to release it from the imprinted COC. The transmittance of COC was increased from 90% to 95% by nanostructuring both sides of the COC film. The aspect ratio of the structures was up to 12, and the tip of the structures had a diameter of less than 20 nm (see

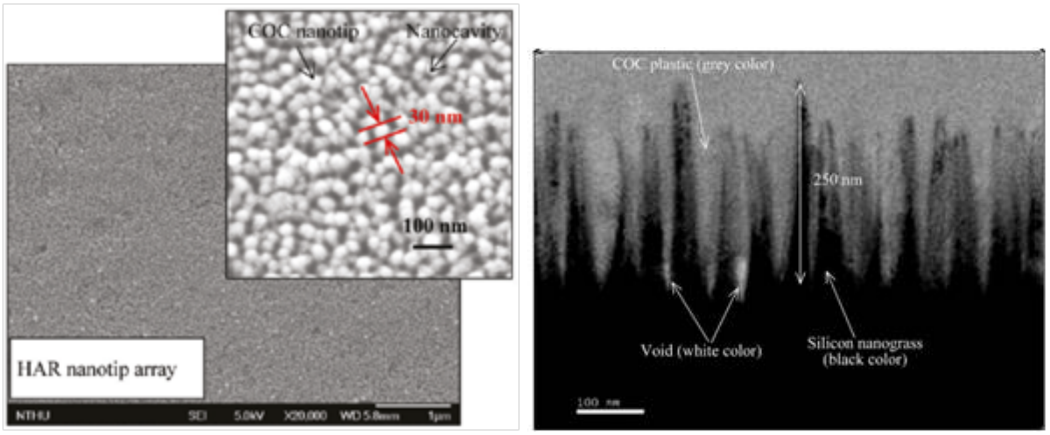

Figure 1.7: Left: Top view SEM image of the COC surface after hot embossing at 180 °C, using a BSi mould. Right: TEM image of the embossing process, showing both the Si master and COC prior to demoulding. Images are from Hong *et al.*[22].

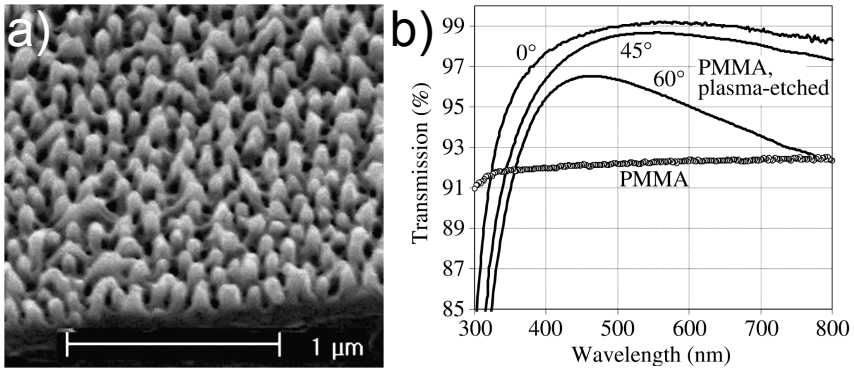

Figure 1.8: Antireflective nanostructures by plasma etching of PMMA. a) SEM image of nanostructured PMMA surface. b) Transmittance measurements of the nanostructured surface, showing increased transmittance for wavelengths above 325 nm. Figures are from Schulz *et al.*[24].

Fig. 1.7).

In 2011 Deniz *et al.*[23] reported antireflective properties of a thin hydrogen silsesquioxane (HSQ) film on a glass substrate. The HSQ film was imprinted with an APA master by embossing at room temperature, thermal curing of the HSQ and dissolving the APA master. The nanostructured thin film showed increased transmittance above wavelengths of 550 nm, compared to a glass substrate coated with a planar HSQ film. In this region, transmittance was increased from approximately 91% to 93%[23]. Ellipsometry measurements showed that the reflectance of the nanostructured HSQ film on glass was below 2% for incident angles up 65°. In comparison the reflectance of a HSQ film on glass was up to 3% at an incident angle of 15°. The results were compared to finite-difference time-domain simulations, and it was concluded that the optimal height of the tapered structures in a hexagonal array would be 175 nm (in an HSQ layer with total thickness of 275 nm on a glass substrate).

Schulz *et al.*[24] used an advanced plasma etching technique to form AR nanostructures directly in PMMA substrates (Fig. 1.8 (a)). The transmittance of the structured substrates was increased to up to 99% as shown in Fig. 1.8 (b).

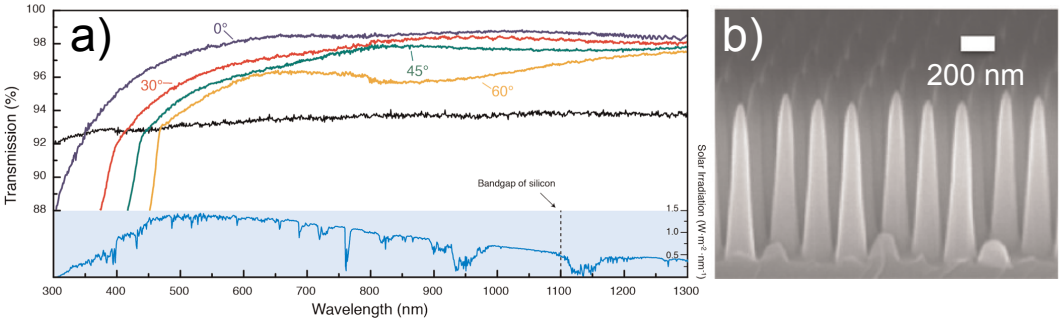

Figure 1.9: Results from Park *et al.* a) Transmittance spectra of fused silica wafer with nanostructures on both faces, for different incident angles. The solar irradiation spectrum is shown in the bottom. b) SEM image of the tapered nanostructures with 200 nm period.

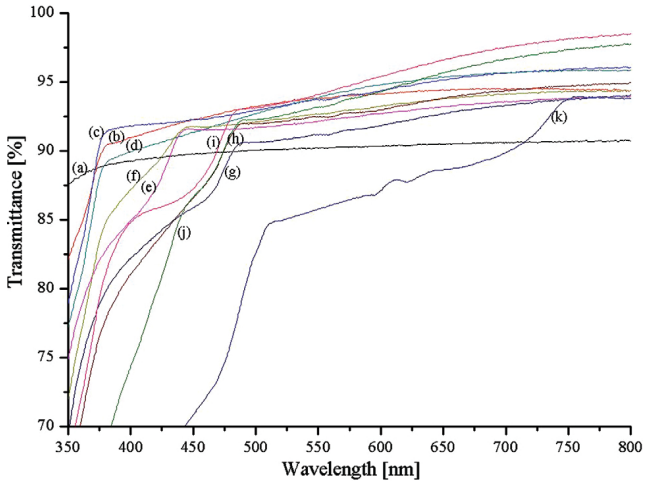

Figure 1.10: Transmittance measurements on periodic structures, from Jang *et al.*[26]). Cut-offs are seen where the transmittance drops, due to the onset of diffraction.

1.2.2 Periodic AR nanostructures

Park *et al.*[25] used interference lithography to form pillar arrays with 200 nm period and 1100 nm height, in fused silica wafers. Tapered cones were fabricated by forming posts of poly silicon on the fused silica surface. These posts were used as an etch mask in a Reactive Ion Etching (RIE) process, which slowly etched the poly silicon mask, resulting in tapered structures in the fused silica surface. Fig. 1.9 (a) shows transmittance spectra of the fused silica wafer with nanostructures on both faces. At normal incidence the transmittance was increased to around 98%, and dropped off as the incident angle was increased, to around 96% at 60°.

Jang *et al.* used laser interference lithography to fabricate nanostructured Si masters, which were used for hot embossing of polycarbonate. Transmittance was increased from 90% to 93.5% (single side)[26], as shown in Fig. 1.10. Drops in transmittance were seen when diffraction occurred for shorter wavelengths. A grating with 227 nm period had a cut-off at approximately 375 nm. A 300 nm period had a cut-off at approximately 475 nm.

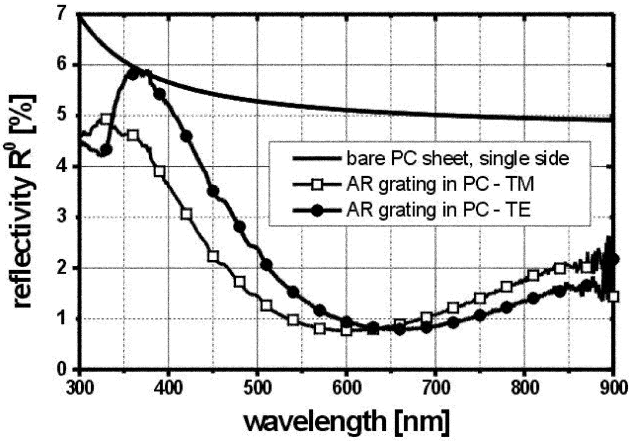

Figure 1.11: Reflectance of a binary AR grating structure in a polycarbonate sheet. Figure from David *et al.*[28]

1.2.3 Binary AR nanostructures

The binary AR structures have the virtue that they in theory can be designed to achieve 0% reflectance at a specific wavelength. This makes them particularly interesting for lasers. Kanamori *et al.* took advantage of this in a recent paper, where they fabricated binary AR nanostructures directly on the tips of fibers for optical communications wavelengths[27]. The structures were fabricated using electron beam lithography (EBL), and were pillars with a diameter of 560 nm, a period of 700 nm, and a height of 250 nm. They were designed for a wavelengths of 1550 nm, for which the optimum height is 320 nm. The reflectance of the structures was measured in the wavelength range 1460 nm to 1580 nm, and was reduced to 0.27%, from roughly 4%.

David *et al.* fabricated binary AR structures for visible wavelengths using 1D gratings[28]. The structures were fabricated in a quartz wafer using EBL, from which a Ni shim was electroplated. The structures were then hot embossed in 1 mm thick polycarbonate sheets. The reflectance of a single interface was lowered from around 5% to 1% at 600 nm. The reflectance increases significantly for smaller wavelengths, as shown Fig. 1.11.

1.2.4 AR thin film coatings

Traditionally reflections of light are suppressed by adding one or more layers of dielectric or metallic thin films on the substrate surface. A single layer can reduce the reflectance of a glass surface to a mean value of approximately 2.5% in the visible spectrum. Multilayer coatings, typically with 3-6 layers can reduce the reflectance to below 0.5% in the visible spectrum as seen in Fig. 1.12. Such coatings are rather expensive, are limited by a trade-off between reflectance and bandwidth, and are sensitive to the incident angle.

1.2.5 Scattering from defects and random structures

Lehr *et al.*[30] used rigorous coupled-wave analysis (RCWA) to predict the scattering due to imperfections in periodic cone-like antireflective structures. They varied the height of each protrusion as a Gaussian distribution, and calculated the total scattered light, due to the imperfections which introduce new periods in the lattice, which violate the zero'th order diffraction condition. In a similar way they varied the lateral positions of the individual

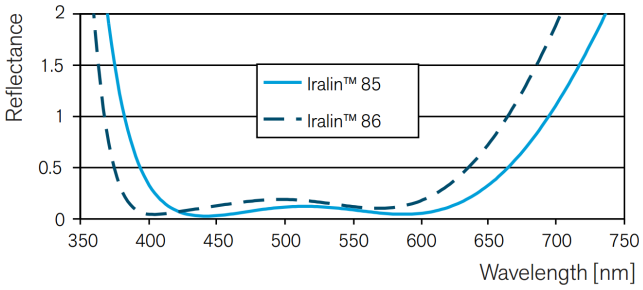

Figure 1.12: Reflectance of commercial multilayer antireflective coatings. The figure is from Optics Balzers[29].

cones. They compared their simulations to a fabricated periodic structure with a period of 80 nm. In this way they fitted the measured spectrum of the structures, to that of super-Gaussian profiles with a standard deviation of $\sigma = 15\%$ on both the heights and the lateral positions (the scattering term was calculated from a 1-dimensional profile, so the results are not quantitatively accurate). The fabricated structures were fabricated using block copolymer micelle lithography and RIE. The structures had a height of 235 nm and a period of 80 nm. Fig. 1.13 shows that the amount of scattered light increases with the variation in both the heights and the lateral position of the protrusions.

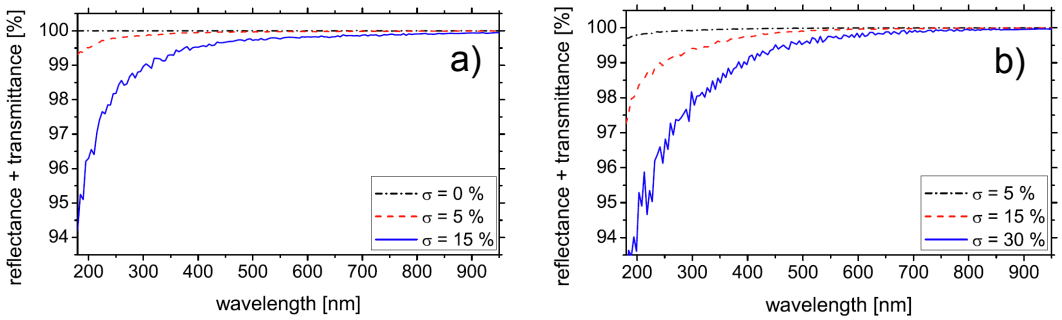

Figure 1.13: Calculated sum of specular reflected and transmitted light, when incident on a periodically structured surface with defects. a) The heights of the protrusions vary as a Gaussian distribution with standard deviation, σ. b) The lateral positions of the protrusions are varied. Figures from Lehr *et al.*[30].

1.2.6 Nanostructured metal surfaces

The optical properties of metals result in a very high reflectance in the visible spectrum. Recent studies have shown however, that this reflectance can be reduced by micro- and nanostructures. Such absorbing metals have been suggested for use in photovoltaics and thermo-photovoltaics, as well as for increasing the contrast of flat-panel displays.

Vorobyev *et al.* have studied blackening of various metals by femtosecond laser ablation[31]. They observed that dramatic changes of the optical properties of metals surfaces occurred after multiple exposures by a laser beam, as shown in Fig. 1.14 (a-c). Blackening of Al, Pt, and Si has been reported, and also colouring of Al surfaces, both diffractive, and angle-independent[32–35]. The ablation forms microstructures in the surface, while droplets of ablated material can redeposit on the surface as nanoparticles. Thus, various different structures are formed on the surface, both on the micro and nanoscale. Vorobyev *et al.* list four

possible mechanisms for the increased absorption[31]. An antireflective effect due to the gradient in the refractive index of the air-metal interface. Absorption due to surface plasmon resonances, broadened by the presence of multiple different nanoparticle sizes. Plasmonic absorption in choral- or fractal like nanostructures of different shapes and sizes. And finally they propose that absorption is increased due to multiple reflections and light trapping on the microstructures.

Other authors have also reported on similar findings for the blackening on Cu, using nano-, pico-, or femtosecond laser ablation[36;37], as shown in Fig 1.14 (d-e).

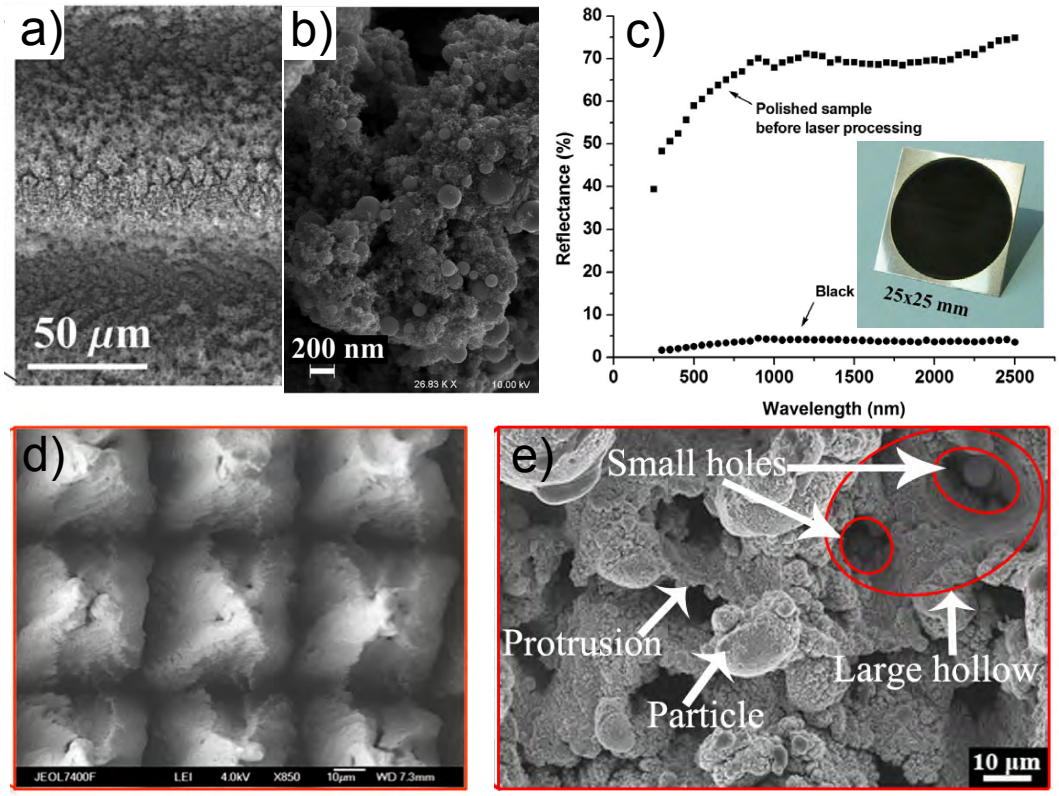

Figure 1.14: Laser ablated metal surfaces. The laser ablation induces a combination of micro and nanostructures in the metal surfaces, which increase the absorption of the metal. a-c) Nanostructured Pt surface with reflectance of around 5%, from Vorobyev *et al.*[33]. d) SEM image of structured Cu surface from Tang *et al.*[36] e) SEM image of structures in Cu by Fan *et al.*[37].

While the laser ablation techniques result in rather uncontrolled micro-and nanostructures, Søndergaard *et al.* have taken a different approach to achieve metal surfaces with low reflectance and high absorbance. In a paper from 2012 they achieve an average absorbance in the visible spectrum of 96%, in 900 nm thick gold films[38]. This was done by ion beam milling of 2D groove arrays with a period and height of 250 nm. The structured surface allows for excitation of surface plasmons that can propagate to the bottom of the grooves under adiabatic nanofocussing. The well defined geometry of the structures enables a detailed theoretical description of the underlying physics[39].

Finally, Jen *et al.* fabricated metal-dielectric-metal nano-pillars on a glass substrate with an

absorbance of 40-80% in the visible spectrum[40].

Absorbing metal films from multilayer interference

Cho *et al.* presented a method to produce a black surface based on absorption of a thin metal film[41]. It comprised a four layer stack of metal and dielectric thin films. With a Cr thickness of 16 nm they report a specular reflection of the film of 0.7% when averaged over the visible spectrum, from 380 - 780 nm. The method only worked with Cr and Mo, for which both n and k are between 2.8 and 4.5. These particular metals have a low reflectance, while maintaining an adequate absorptivity, as shown in Fig. 1.15.

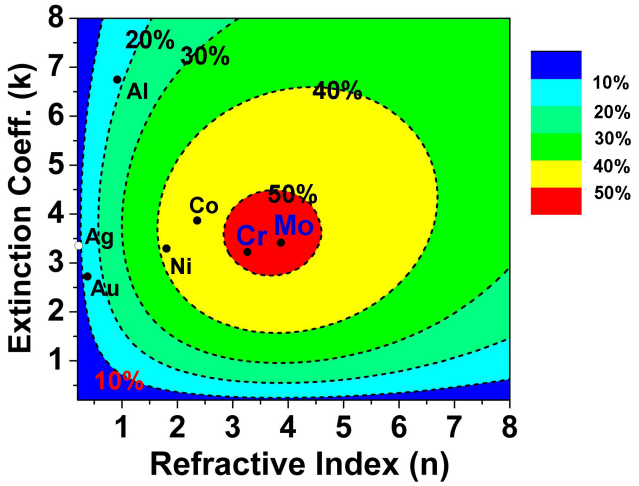

Figure 1.15: Absorbance of various 10-nm thick films calculated at 550 nm wavelength. Figure from Cho *et al.*[41].

Nanostructured heat insulating metal films

Metal films deposited on nanostructured surfaces have also been suggested for use as infrared filters with increased transmittance for visible wavelengths. Ting *et al.* fabricated antireflective nanostructures by interference lithography, and electroplated the structures to form a Ni shim. The Ni shim was used in a roll-to-roll process to replicate the structures to a UV curable resin on a polyethylene terephthalate foil[42]. Thin metal films were then deposited on the structured foil. Ting *et al.* showed that a 25 nm thick Au film deposited on the nanostructured foil had a transmittance of around 40% in the visible range, and 15% transmittance in the 750-1800 nm wavelength range[43;44]. Also nanostructured Ag films have been studied[45;46].

A similar study was presented by Choi *et al.*[47], who fabricated a hexagonal array of pillars with a pitch of 540 nm and a height of 260 nm, using UV nano imprint lithography (UV-NIL). They subsequently etched the structures using RIE, to form tapered cones. A 5 nm Ag film was deposited on the structures, and the optical properties were characterized. The authors concluded that the transmittance was increased, as the structures became more tapered.

1.3 Thesis outline

This thesis investigates the prospects of achieving optically functional nanostructures, which can potentially be mass produced using e.g. injection moulding or roll-to-roll processes. A key concept of the thesis has been to reduce the cost of the nanostructured masters, for which BSi has been used for fabricating nanostructures on larger areas.
The first part of the thesis gives a basic introduction to the optical properties of dielectrics and metals, and describes some of the methods used in the thesis. The results of this thesis are presented in two parts: the first part deals with dielectric materials, while the second part covers nanostructured metal surfaces.

Chapter 2 gives a short introduction to the theory of optical properties of dielectrics and metals.

Chapter 3 covers the experimental methods used in the thesis.

Chapter 4 presents the results of nanostructured dielectric surfaces, in the form of published papers, and an unpublished manuscript.

Chapter 5 discusses the experimental results on nanostructured thin metal films.

Chapter 6 is a patent application about nanostructured metal surfaces used for structural colouring.

Chapters 7 and 8 summarizes the conclusions of the thesis, and gives an outlook on future possibilities.

2

Theory of the optical properties of nanostructured surfaces

The following chapter will give a short introduction to the basic theoretical background for the thesis. The first part deals with reflectance from dielectric surfaces, and the theory of reflectance from stacks of thin films. The diffraction limit is introduced, followed by effective medium theory. With these concepts and mathematical tools, the basic theory of gradient and binary antireflective nanostructures are discussed. Finally, the interactions between light and metals are discussed.

2.1 Fresnel reflection

Light incident on an interface between two materials with different refractive indices, is subject to reflection, given by the Fresnel equation[48]

$$r_{\mathrm{TE}} = \frac{\cos\theta - \sqrt{n^2 - \sin^2\theta}}{\cos\theta + \sqrt{n^2 - \sin^2\theta}} \qquad r_{\mathrm{TM}} = \frac{-n^2\cos\theta + \sqrt{n^2 - \sin^2\theta}}{n^2\cos\theta + \sqrt{n^2 - \sin^2\theta}} \tag{2.1.1}$$

where r_{TE} and r_{TM} are the reflection coefficients of the transverse electric (TE) and transverse magnetic (TM) polarizations, which give the ratio of the reflected electrical field relative to the incident electrical field. θ is the incident angle with respect to the surface normal and $n = n_2/n_1$ is the ratio between the refractive index of the two media. The reflectance R is the ratio of the reflected power, P_r, relative to the incident power, P_i, and is given by

$$R = \frac{P_r}{P_i} = \left(\frac{E_r}{E_i}\right)^2 = r^2 \tag{2.1.2}$$

Figure 2.1 shows the reflectance of both polarizations for the interfaces between air ($n_1 = 1$) and a dielectric ($n_2 = 1.5$). The external reflectance refers to the air-dielectric interface, while the internal reflectance refers to the dielectric-air interface.
For normal incidence the Fresnel equation is independent of polarization, and yields equal results for internal and external reflection. The reflectance is then given by[49]

$$R = \left(\frac{n_1 - n_2}{n_1 + n_2}\right)^2 \tag{2.1.3}$$

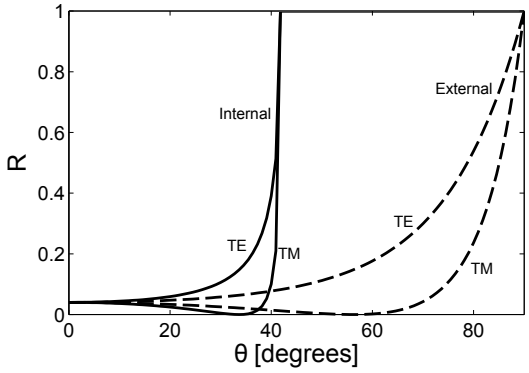

Figure 2.1: The reflectance R as function of angle of incidence θ, plotted for both internal and external reflection for both polarizations.

where n_1 and n_2 are the refractive indices of the first and second medium respectively. For light in air ($n_1 = 1$), incident on a polymer surface ($n_2 = 1.5$), the reflectance amounts to 4%.

2.2 Transfer matrix method

Later in this chapter we will model the antireflective properties of nanostructured dielectric materials, as well as thin metallic films. For such calculations, the transfer matrix method will become useful for modelling the optical properties of stratified media.

When modelling the effect of thin films on a substrate the reflection properties can be described by a transfer matrix which relates the electromagnetic fields on one side of the film (or films) to the electromagnetic fields on the other side.

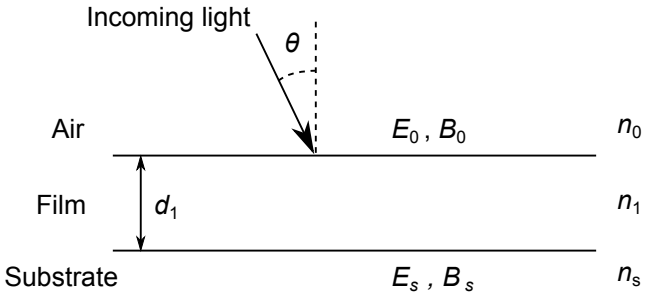

Figure 2.2: Sketch of a thin film on substrate. The magnitude of the electromagnetic fields on above the film (E_0, B_0) can be related to the magnitude of the electromagnetic fields below the film (E_s, B_s) by a transfer matrix.

In the following we write the refractive index as $\hat{n}$, in order to indicate that the equations are valid for real as well as complex refractive indices. Consider the example shown in figure 2.2 where a thin film of refractive index $\hat{n}_1$ is located on top of a substrate with refractive index $\hat{n}_s$ and with a material with refractive index $\hat{n}_0$ on top of the film. The film thickness is d_1 and the incident angle is θ. The magnitude of the electric and magnetic fields $\vec{\mathbf{E}}$ and $\vec{\mathbf{B}}$, just above the layer are denoted E_0 and B_0. Just below the film/substrate interface they are denoted E_s and B_s. The magnitude of the electromagnetic fields are now related by a transfer matrix $\mathbf{M}_1$ by the following relation[48]:

$$\begin{bmatrix} E_0 \\ B_0 \end{bmatrix} = \mathbf{M}_1 \begin{bmatrix} E_s \\ B_s \end{bmatrix} = \begin{bmatrix} m'_{11} & m'_{12} \\ m'_{21} & m'_{22} \end{bmatrix} \begin{bmatrix} E_s \\ B_s \end{bmatrix}. \tag{2.2.1}$$

If several films are placed adjacent to each other, the fields at the two boundaries of the stack can be related by a matrix which is the product of the matrix of each of the individual layers. This mathematical method thus accounts for the multitude of internal reflections and phase changes, occurring in a stack of thin films. As the method is valid for materials with real and complex refractive indices alike, it represents a powerful and simple tool for the theoretical properties of many of the optical systems discussed in this thesis.

The formulas can be derived by solving Maxwell's equations with appropriate boundary conditions. This has been covered in numerous good textbooks[48;49], and we will not go through the derivations here. Instead we focus on the implementation of these formulas. The characteristic matrix, $\mathbf{M}_j$ of a homogeneous thin film, surrounded by two homogeneous media is given by (for TE mode)[49]

$$\mathbf{M}_j = \begin{bmatrix} m'_{11} & m'_{12} \\ m'_{21} & m'_{22} \end{bmatrix} \tag{2.2.2}$$

where

$$m'_{11} = m'_{22} = \cos\hat{\beta}_j, \qquad m'_{12} = -\frac{i}{p_j}\sin\hat{\beta}_j, \qquad m'_{21} = -ip_j\sin\hat{\beta}_j \tag{2.2.3}$$

and

$$\hat{\beta}_j = \frac{2\pi}{\lambda_0}\hat{n}_j d_j \cos\hat{\theta}_j, \qquad p_j = \hat{n}_j \cos\hat{\theta}_j \tag{2.2.4}$$

where $\hat{n}_j$, d_j, and θ_j are the complex refractive index, the thickness, and the angle of propagation for the j'th layer. For a stack of N films, the total transfer matrix is calculated as

$$\mathbf{M} = \begin{bmatrix} m_{11} & m_{12} \\ m_{21} & m_{22} \end{bmatrix} = \prod_{j=1}^{N} \mathbf{M}_j \tag{2.2.5}$$

The reflection and transmission coefficients of the stack are then given by

$$r = \frac{(m_{11}+m_{12}p_s)p_0 - (m_{21}+m_{22}p_s)}{(m_{11}+m_{12}p_s)p_0 + (m_{21}+m_{22}p_s)}, \tag{2.2.6}$$

$$t = \frac{2p_0}{(m_{11}+m_{12}p_s)p_0 + (m_{21}+m_{22}p_s)} \tag{2.2.7}$$

where the subscript 0 refers to the first semi-infinite medium surrounding the stack, and the subscript s refers to the last. The reflectivity and transmissivity are

$$R = |r|^2 \tag{2.2.8}$$

$$T = \frac{p_s}{p_0}|t|^2 \tag{2.2.9}$$

where

$$p_0 = \hat{n}_0 \cos\hat{\theta}_0 \quad \text{and} \quad p_s = \hat{n}_s \cos\hat{\theta}_s \tag{2.2.10}$$

For TM mode the formulas are analogous, and differ only by the expressions for p_0, p_j, and p_s, which are then given by

$$p_{0,\mathrm{TM}} = \frac{1}{\hat{n}_0}\cos\hat{\theta}_0, \qquad p_{j,\mathrm{TM}} = \frac{1}{\hat{n}_j}\cos\hat{\theta}_j, \qquad p_{s,\mathrm{TM}} = \frac{1}{\hat{n}_s}\cos\hat{\theta}_s \tag{2.2.11}$$

The above set of equations can be used to describe stratified media with arbitrarily many layers. Furthermore, the equations are valid for both dielectric materials with real refractive indices, and for metals with complex refractive index, $\hat{n} = n + ik$. The transfer matrix method will be used throughout the thesis, for describing the optical properties of both gradient type and binary type AR nanostructures, as well as planar metal films.

2.3 Below the diffraction limit

Ultimately we would like to use the transfer matrix method to describe the optical properties of nanostructured dielectric materials. However, before we can do this we need a few more tools in order to relate the nanostructured surfaces to a system which can be described as a stratified medium, with layers of homogeneous refractive indices. First we discuss the diffraction limit for periodically structured surfaces, which can be used as a limit for when structures can be described using effective medium theory, which will be introduced in Sec. 2.4. In terms of optical properties, the diffraction limit is also important, since if the structures are in the diffraction regime, bright reflected or transmitted orders will be seen on the surface.

When light is incident on a periodically corrugated surface, the propagation of a diffraction order is determined by the grating equation[50]

$$n_m \sin\theta_m - n_0 \sin\theta_0 = \frac{m\lambda}{\Lambda} \tag{2.3.1}$$

where n_0 and n_m is the refractive index of the incident medium and the medium in which the diffracted order is travelling ($n_m = n_0$ for reflected light, or $n_m = n_s$ for transmitted light), m is the diffracted order, θ_0 and θ_m are the angle of incidence and the diffracted light of m'th order (measured from normal to the surface). The incident wavelength is denoted λ and Λ the period of the grating. From equation 2.3.1, it follows that only zero'th order diffraction allowed when Λ fulfils the condition

$$\Lambda < \frac{\lambda}{\max[n_s, n_0] + n_0 \sin\theta}, \tag{2.3.2}$$

The lower limit of λ for visible light is around 380 nm. At normal incidence, the condition for avoiding diffraction is then $\Lambda < 380$ nm for reflected light, and $\Lambda < 250$ nm for transmitted light in a medium with refractive index $n_s = 1.5$. If we consider all incident angles ($\theta = 90°$), then the constraint is $\Lambda < 150$ nm, for transmission through a medium with refractive index $n_s = 1.5$. Note that for reflectance at normal incidence, the condition is simply $\Lambda < \lambda$, which has give rise to the term sub-wavelength structures.

2.4 Effective medium theory

The macroscopic properties of a heterogeneous material can in some cases be described by a single effective parameter. This is referred to as effective medium theory[1] (EMT). A prerequisite for using EMT for structured surfaces is that the structures are in the effective medium regime, i.e. small enough to be below the diffraction limit described by Eq. 2.3.2.

In optics, two models are often used to describe the effective relative permittivity: the Bruggeman model, and the Maxwell Garnett model[2]. The Bruggeman and Maxwell Garnett effective medium expressions are in explicit form[51]:

$$\varepsilon_{\text{eff}}^{\text{BR}} = \frac{1}{4}\left\{\varepsilon_1(2-3f_2)+\varepsilon_2(3f_2-1)+\sqrt{[\varepsilon_1(2-3f_2)+\varepsilon_2(3f_2-1)]^2+8\varepsilon_1\varepsilon_2}\right\} \quad (2.4.1)$$

and

$$\varepsilon_{\text{eff}}^{\text{MG}} = \varepsilon_1\frac{\varepsilon_2(1+2f_2)-\varepsilon_1(2f_2-2)}{\varepsilon_1(2+f_2)+\varepsilon 2(1-f_2)} \quad (2.4.2)$$

where ε_1 and ε_2 are the relative permittivities of the first and second material respectively, and f_2 is the volume fraction of the second material[3]. Throughout this thesis we will assume that the materials are non-magnetic so that the magnetic permeability, $\mu = 1$. Then $n^2 = \varepsilon$, where n is the refractive index, and ε is the relative permittivity[4].

While the Maxwell Garnett model is derived by assuming a small volume fraction, the Bruggeman equation makes no such assumption. It is often discussed which model is best for a given material, especially when describing metals. Here we will limit ourselves to use EMT for purely dielectric materials. In this case the two models behave very similar, as shown in Fig. 2.3, where the effective refractive index is plotted as a function of volume fraction of a polymer ($n_2 = 1.5$) in air ($n_1 = 1$). Also shown, is a simple average of the refractive indices, $n_{\text{Linear}} = f_1 n_1 + (1-f_1)n_2$, which is seen to be a good approximation in the case of dielectric materials, and relatively low refractive indices. The maximum difference between the Maxwell Garnett and the linear model, is around 0.02 refractive index units, at around $f = 0.5$.

[1] also known as mean field approximation or homogenization.

[2] The model was derived by James Clerk Maxwell Garnett (1880-1958) in 1905 - not to be confused with the James Clerk Maxwell (1831-1879) who earlier postulated a set of equations describing electromagnetic fields.

[3] The stated expression are the explicit forms of the two equations. Strictly, the equations should be given in their explicit forms, from which the correct branch of solutions should be selected. This problem is discussed by Roussel *et al.*[52] and Bosch *et al.*[53].

[4] Historically the relative permittivity has been referred to as the *dielectric constant*. This term however, has been deprecated by the IEEE standards association[54].

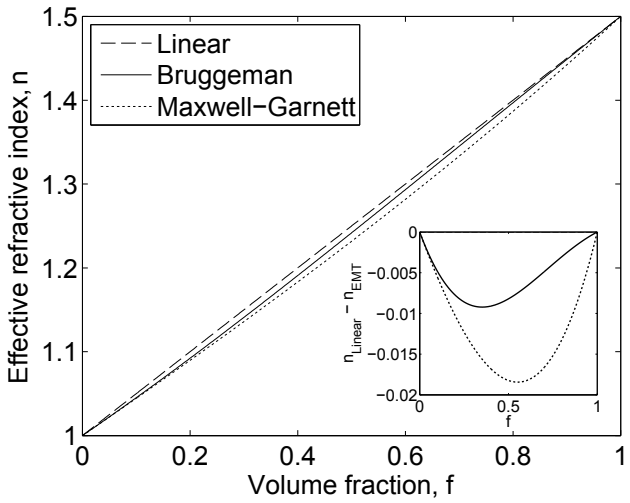

Figure 2.3: Comparison of effective medium theories for dielectrics. The effective refractive index of a heterogeneous medium of a dielectric ($n_2 = 1.5$) and air ($n_1 = 1$), is plotted as a function of the volume fraction of polymer, f, for different models.

The effective medium theory, when combined with the transfer matrix method, is a very potent tool for calculating the properties of antireflective nanostructures, as we shall see in the following sections.

2.5 Gradient AR nanostructures

In Sec. 2.1 we saw that light incident on an interface between two media with different refractive indices, is subject to Fresnel reflection. We will now discuss the principles of using tapered nanostructures to suppress such reflections.

The physical explanation of the moth-eye structures is that they can be described by EMT, so that the tapered nanostructures provide a gradual change in the effective refractive index over the interface, as opposed to a sudden change, like on a planar surface. The gradual change "removes" the interface at which the light would be reflected, and allows a larger part of the light to be transmitted over the interface. An important aspect of the theory is that the structures are sufficiently small, so that the structures do not scatter or diffract the incoming light, but only zero'th order propagation is allowed. In this regime the incoming light cannot resolve the individual structures, but only "feels" the gradual change in the effective refractive index.
As discussed in Sec. 2.4, this description assumes that the structures are in the effective medium regime, i.e. the structures fulfil Eq. 2.3.2, for periodic structures. Later in this thesis also random structures will be described using EMT (Paper IV, Sec. 4.5). For random structures there is no well defined period. But as will be discussed in Paper II (Sec. 4.3), scattering from the structures will be negligible if the characteristic length scale of the nanostructures is small enough. For such structures, EMT can be applied as well.

2.5.1 Modelling of the gradient AR effect

In a more rigorous manner, a model for the antireflective effect of gradient structures can be set up. The idea of the model is outlined in Fig. 2.4. The nanostructured region can

be divided into N layers. Each of the layers will have a different volume fraction, which translates into different effective refractive indices, by using EMT.

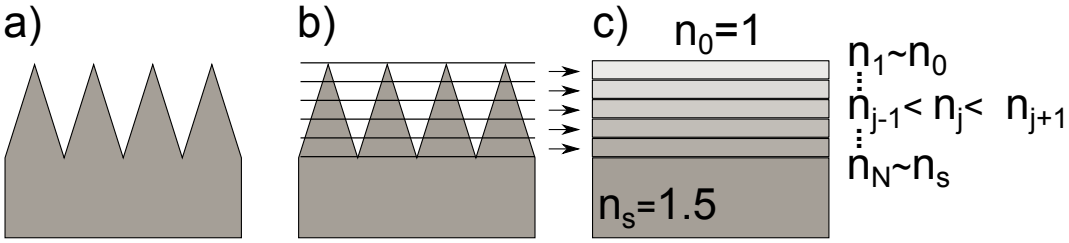

Figure 2.4: Principle of gradient AR nanostructures. a) The surface is structured by sub-wavelength structures. b) The structured region is divided into layers. c) Each of the layers will have a different volume fraction, which translates into different effective refractive indices, by using EMT.

The surface can now be described by $N+1$ interfaces, each with a very small change in refractive index. Recalling the Fresnel equation, the reflectance at each interface will be very small, due to the small change in refractive index. Due to the non-linearity of the Fresnel equation, the overall reflectance of the surface will be lower than that of a planar surface, even though the total change in refractive index is maintained.

The total reflectance of the stack can now be calculated using the transfer matrix method. Due to the scaling invariance of Maxwell's equations, it is instructive to show the reflectance as a function of the normalized height, d/λ, where d is the height of the structures. Figure 2.5 shows the calculated reflectance for an AR structure with a linear refractive index gradient, for different values of N. The refractive index of the substrate material is $n_s = 1.5$. It is seen that the calculation has converged for $N = 100$, and that a good antireflective effect is obtained for $d/\lambda > 0.4$, as also shown by Clapham *et al.* [3]. This means that the height of the nanostructures is a critical factor for gradient type AR structures.

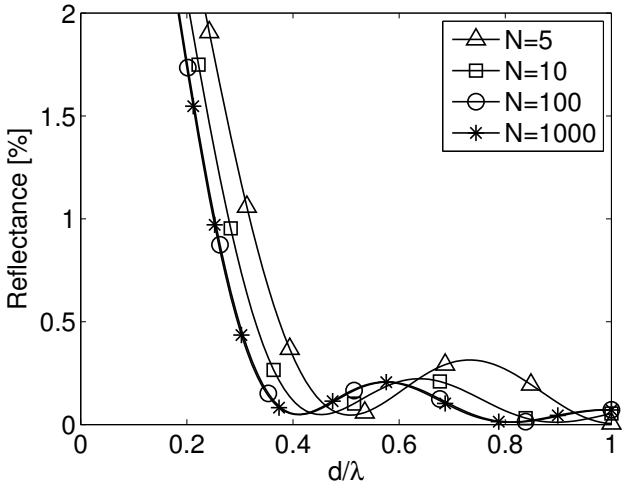

Figure 2.5: Reflectance of gradient AR nanostructures as function of the normalized height, d/λ, for different number of layers, N. It is seen that the calculation has converged for $N = 100$. A good antireflective effect is obtained for $d/\lambda > 0.4$. The calculation is for a linear gradient in the refractive index, and a substrate with $n_s = 1.5$.

Figure 2.6 shows the angle-resolved reflectance of surfaces with gradient AR structures.

The wavelength is 500 nm, and the reflectance is plotted for structures with heights 200 nm and 1000 nm. It is seen that by increasing the height, the range of incident angles for which the structures are effective, increases.

By increasing the height of the gradient AR nanostructures, the spectral region in which the structures are effective (the bandwidth) is increased, and the structures become effective for larger incident angles. However, since the period of the structures should be in the range 150-250 nm, the aspect ratios of such highly effective structures become very large. This makes them more challenging to fabricate using e.g. injection moulding. However, as shown in Fig. 2.5, structures with a height of just 200 nm still have a significant antireflective effect, and are effective for incident angles up to around 50°.

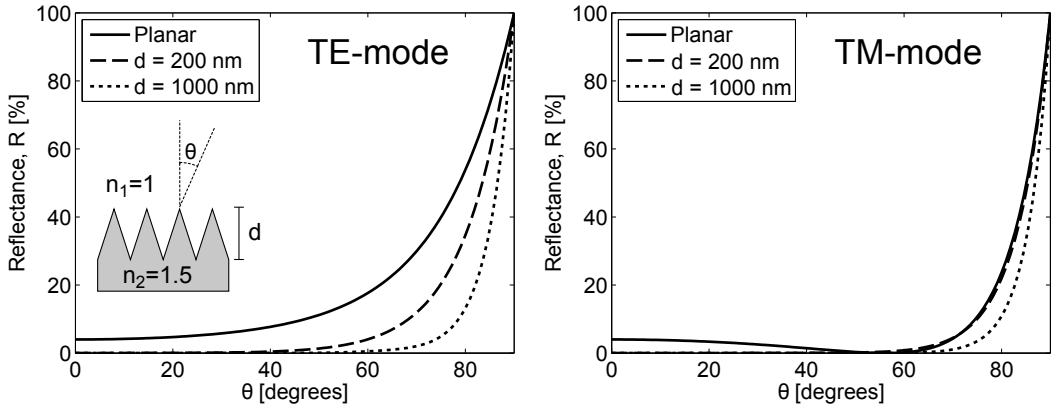

Figure 2.6: Reflectance of gradient AR structures with different heights. The graphs show the reflectance as function of the incident angle, θ. The reflectance was calculated for light with 500 nm wavelength, and a substrate refractive index of $n_s = 1.5$. The left graph is for TE polarization, the right shows TM polarization.

2.6 Binary AR nanostructures

A different type of AR structures rely on a single layer with a homogeneous refractive index, in contrast to the multiple layers of the gradient type structures. We will refer to the single layer structures as binary AR nanostructures. For this type of structures, there is no variation in volume fraction in the vertical direction. The structure can therefore be seen and modelled as a single thin film with a tunable refractive index, which is determined by the volume fraction of material in the layer.

When the period of the structures is below the diffraction limit, the only two design parameters are the height of the layer and the volume fraction of material in the layer. From the Fresnel equation it can be shown that minimum reflectance from a single layer is achieved when the refractive index of the layer is given by $n_1 = \sqrt{n_0 n_s}$, where n_0 and n_s are the refractive index of the incident and substrate media respectively. Furthermore, total destructive interference can occur if the phase difference between the two reflected waves is $\delta = \pi$. This is achieved for normal incidence when the thickness of the layer is given by[48]

$$d_1 = \frac{\lambda}{4n_1}. \tag{2.6.1}$$

where λ is the wavelength in vacuum. This means that the structure will work most efficiently at a single wavelength and that the efficiency will decrease when the wavelength changes.

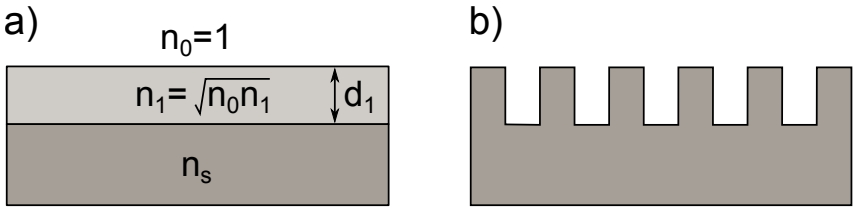

Figure 2.7: a) Sketch of the binary antireflection layer. b) The antireflection layer has the same refractive index as the substrate, but is nanostructured so as to lower the effective refractive index.

We now find the volume fraction of the substrate f, required for the effective refractive index of the intermediate layer to fulfil the expression $n_1 = \sqrt{n_0 n_s}$. In order to show the idea of the derivation, we use the approximate linear expression for the effective refractive medium as discussed in Sec. 2.4. The expression for the effective refractive index n_1 is then

$$n_1 = f n_s + (1-f) n_0 \Leftrightarrow \tag{2.6.2}$$

$$= n_0 + f(n_s - n_0) \tag{2.6.3}$$

The expression can be rewritten as

$$f = \frac{n_1 - n_0}{n_s - n_0} \qquad \Rightarrow \qquad f = \frac{\sqrt{n_0 n_s} - n_0}{n_s - n_0} \tag{2.6.4}$$

where in the last step, the condition $n_1 = \sqrt{n_0 n_s}$ was applied. For $n_0 = 1$ and $n_s = 1.5$ we get $f = 0.45$. Using the Maxwell Garnett model gives an optimal volume fraction of $f = 0.49$.

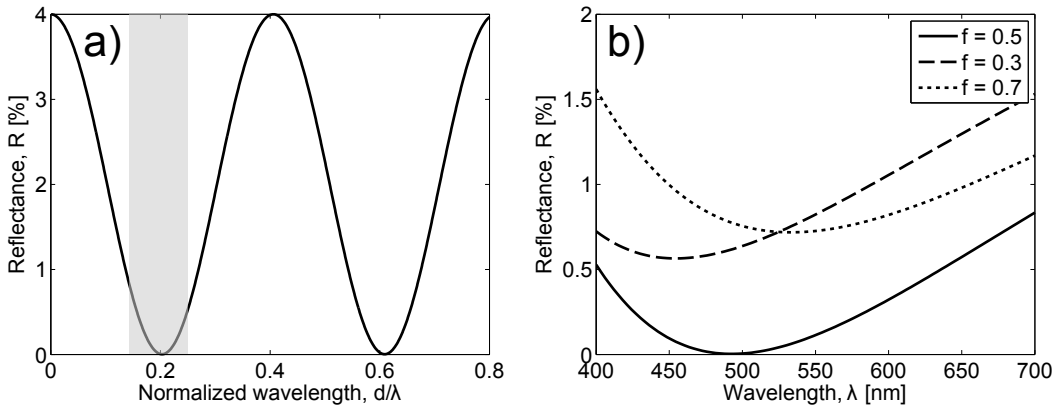

Figure 2.8: Reflectance of binary AR structures. a) Reflectance as function of normalized wavelength d/λ for a structure with volume fraction $f = 0.5$ and $n_s = 1.5$. The grey area marks the visible spectrum of 400-700 nm wavelength, for a structure with a height of $d = 100$ nm. The bandwidth is smaller compared to a gradient structure, since the binary structure is based on interference. b) Structures with $d = 100$ nm, and different volume fractions.

Figure 2.8 (a) shows the reflectance of a binary AR structure with a volume fraction of $f = 0.5$ and refractive index $n_s = 1.5$. The reflectance is plotted as a function of the normalized wavelength d/λ. The grey area marks the visible spectrum of 400-700 nm wavelength, for a structure with a height of $d = 100$ nm. The bandwidth is smaller compared to a gradient structure, since the binary structure is based on interference, and the reflectance is periodic in d/λ. Fig. 2.8 (b) shows the reflectance as function of λ, for a structure with height $d = 100$ nm and $n_s = 1.5$, for different volume fractions. The height fulfils the quarter wave condition, Eq. 2.6.1, for light with a wavelength around 500 nm, which is seen as a minimum in the graph for $f = 0.5$. Changing the height d will displace the optimum wavelength, according to Eq. 2.6.1. Figure 2.8 (b) shows that despite the narrow bandwidth of the binary structure, the reflectance is below 1% throughout the visible spectrum for a structure with volume fraction $f = 0.5$. Small changes in the volume fraction does not change the reflectance significantly, And even at volume fractions of 0.3 and 0.7 the reflectance is still below 1.5% in the visible spectrum.

The angular dependence of the binary AR structures was calculated for structures with a height of $d = 100$ nm, a volume fraction of $f = 0.5$, and a substrate refractive index of $n_s = 1.5$, as shown in Fig. 2.9. The structures are effective up to an angle of around 50°, which is similar to a gradient structure with a height of 200 nm. However, the binary AR structures cannot be further optimized to be effective for larger incident angles.

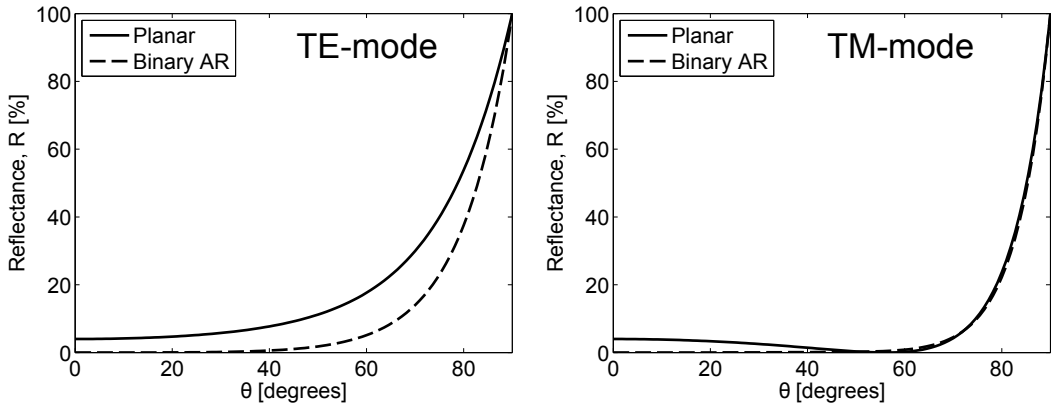

Figure 2.9: Reflectance of a binary AR structure as function of the incident angle, θ. The height of the structures is $d = 100$ nm, the volume fraction $f = 0.5$, and the refractive index of the substrate is $n_s = 1.5$. The left graph is for TE polarization, the right shows TM polarization.

2.6.1 RCWA calculations of 1D and 2D binary AR structures

The previous section showed that 100 nm tall nanostructures with a volume fraction of around 0.5 give rise to an antireflective effect. What EMT fails to predict however, is the difference between 1D (gratings) and 2D (e.g. pillars or holes) structures. In the following we use RCWA, to calculate the properties of 1D and 2D binary AR structures.

The reflectance of a grating, an array of holes, and an array of pillars was calculated using RCWA. The reflectance was calculated for normal incidence, for both TE and TM polarization. All the structures had a height of 100 nm, and had a refractive index of $n = 1.53$ (emulates Topas 8007[55], a COC polymer which is often used for injection moulding and

hot embossing[56;57]). For these calculations a volume fraction of $f = 0.45$ was used.

We used the commercially available code GDCalc[58], which is an engine for Matlab[59], and investigated structures with a period of 150 nm, which is below the diffraction limit as discussed in Sec. 2.3. In this case only a small number of Fourier coefficients, N_F are needed for the solutions to converge, as only the zero'th order is propagating. By increasing N_F in the calculations, it was seen that the simulation was convergent, and that the relative error on the result for $N_F = 5$ was less than 0.1% compared to the result for $N_F = 15$. In the following, $N_F = 10$ was used, since the computational time and memory usage was insignificant.

Figure 2.10 shows the calculated reflectance of the three types of structures. For the 1D grating, the reflectance is polarization dependent, and the reflectance does not behave as predicted by EMT. The two 2D structures in Fig. 2.10 (b) and (c) show the same results as was obtained above, using EMT. This result supports the validity of the use of EMT for binary AR structures, as long as the structures are 2-dimensional. The results further show that the best performance is obtained by using 2D binary AR structures. The 1D grating does however still show good AR performance, and is in practice easier to fabricate than 2D structures.

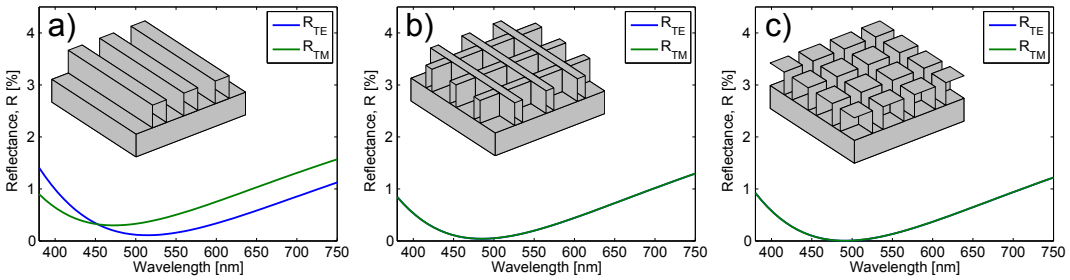

Figure 2.10: RCWA calculations. a) Reflectance for normal incidence on a 1D grating with 150 nm period and a volume fraction of $f = 0.45$, for TE and TM polarization. The reflectance is polarization dependent, and the reflectance does not behave as predicted by EMT. b-c) Reflectance for normal incidence for a 2D array of holes (b) and protrusions (c). The period is 150 nm and the volume fraction is $f = 0.45$.

2.6.2 Super-Gaussian AR structures

The previous sections discussed the functionality of perfect binary AR structures, which can be described as a single layer with a single effective refractive index. In practice however, it is challenging to fabricate perfectly shaped structures at this length scale, and especially if the structures are to be injection moulded, some rounding of the structures must be expected. This rounding could e.g. be described as a super-Gaussian shape. A 2D super-Gaussian distribution can be written as

$$G(x,y) = \frac{1}{\sqrt{2\pi\sigma}} \exp\left(\frac{-\sqrt{x^2+y^2}^{\Omega}}{2\sigma^{\Omega}}\right) \tag{2.6.5}$$

where (x,y) are the lateral coordinates and Ω is the order of the distribution (for $\Omega = 2$, the distribution is a standard Gaussian). σ is related to the full width at half maximum (FWHM) of the distribution by

$$\text{FWHM} = [2\ln(2)]^{\frac{1}{\Omega}}\,\sigma \tag{2.6.6}$$

For this investigation it is preferable to keep the height d of the structures fixed, which is ensured by replacing the normalization factor in Eq. 2.6.5 by d, so that the distribution is written

$$G(x,y) = d\exp\left(\frac{-\sqrt{x^2+y^2}^{\Omega}}{2\sigma^{\Omega}}\right). \tag{2.6.7}$$

Figure 2.11 (a) shows four super-Gaussian shapes with heights of 100 nm, and their theoretical reflectance. The structure with $\Omega = 50$ closely resembles a perfect cylinder shaped binary AR structure. Decreasing the value of Ω leads to a rounding of the structures, and the minimum reflectance shifts towards lower wavelengths, as the structures start to resemble gradient type structures. We recall that for a linear volume fraction gradient (which is the case for paraboloid structures), the minimum reflectance occurs at $\lambda = d/0.4$, which corresponds to $\lambda = 250$ nm for $d = 100$ nm.

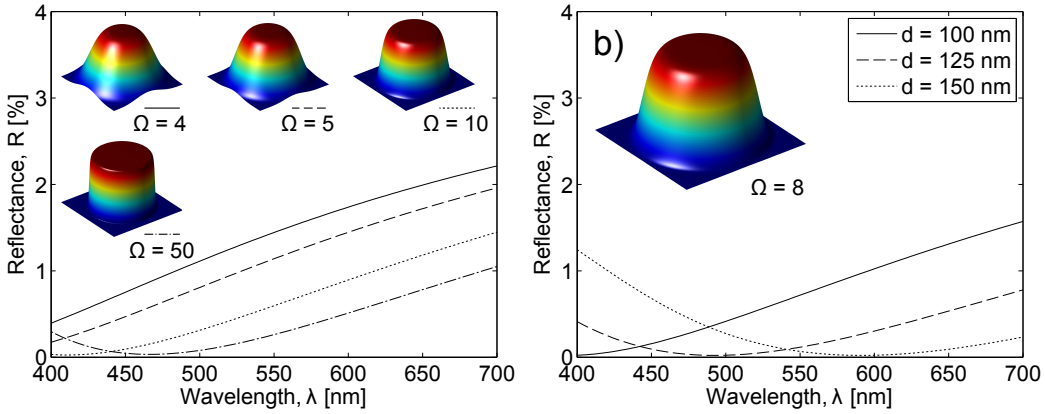

Figure 2.11: Calculated reflectance of super-Gaussian profiles. (a) Reflectance for profiles of different order, Ω. (b) Reflectance for structures of different heights, with $\Omega = 8$.

The shift in optimal wavelength can be compensated for, by increasing the height of the structures. As shown in Fig. 2.11 (b), structures with $\Omega = 8$, and a height of 125 nm will have a reflectance below 1% in the visible spectrum. This result suggests that the effect of imperfect replication of binary AR nanostructures can be compensated for in the design, by adjusting the height of the structures.

2.7 Optical properties of metals

In the final part of this theory chapter, we leave the dielectric materials for a while, in order to introduce some basic optical properties of metals. This section forms the basis for the discussion of nanostructured metal films in Chap. 5. The theory presented here draws inspiration from Maier[60], who offers a comprehensive introduction to the field of plasmonics, and from Born and Wolf[49] who discuss the basic optical properties of planar thin metal films.

The optical properties of a metal can to a large extent be analysed by describing the metal as a sea or plasma of electrons, existing in a matrix of positively charged ion cores. The electrons in the conduction band are free to move around in the matrix, which means that they can readily interact with external electric fields. An electric field will impose a force on the electrons which will displace the electron plasma with respect to the ion cores, which gives rise to a polarization in the metal.

If the electric field is oscillating, as is the case with electromagnetic waves, the polarization will oscillate as a reaction to the imposed field. This description leads to an expression for the relative permittivity ε, which describes the relation between the dielectric displacement field $\vec{\mathbf{D}}$ to the electric field $\vec{\mathbf{E}}$, which is given by one of the constitutive relations of Maxwell's equations, $\vec{\mathbf{D}} = \varepsilon_0 \varepsilon \vec{\mathbf{E}}$, where ε_0 is the vacuum permittivity. The result is called the Drude model and describes the complex relative permittivity as[60]

$$\varepsilon(\omega) = 1 - \frac{\omega_p^2}{\omega^2 + i\gamma\omega} \tag{2.7.1}$$

where ω is the angular frequency of the driving field and γ is the collision frequency for the electrons. $\omega_p^2 = \frac{ne^2}{\varepsilon_0 m_e}$ is the plasma frequency, where n is the number density of electrons, e the elementary charge, m_e is the effective optical mass of the electrons. The plasma frequency can be described as the natural frequency of the electron sea. Below this frequency, the electron sea exhibits metallic behaviour, as the electric field can cause electrons to oscillate. These oscillations are then damped, mainly due to collisions with phonons, causing a strong attenuation of the electric field. Above the plasma frequency the metal becomes transparent to electromagnetic waves. For most metals this occurs well into the UV frequency range.

The relative permittivity is related to the complex refractive index by $\hat{n}^2 = \varepsilon$, where $\varepsilon = \varepsilon_1 + i\varepsilon_2$ and $\hat{n} = n + ik$. This gives the following relations between the real and complex parts of the two values:

$$\varepsilon_1 = n^2 - k^2 \tag{2.7.2}$$
$$\varepsilon_2 = 2nk \tag{2.7.3}$$
$$n^2 = \frac{\varepsilon_1}{2} + \frac{1}{2}\sqrt{\varepsilon_1^2 + \varepsilon_2^2} \tag{2.7.4}$$
$$k = \frac{\varepsilon_2}{2n}. \tag{2.7.5}$$

Furthermore, k is related to the absorption coefficient α of Beer's law, by $\alpha = 2k\omega/c$. Beer's law describes the decay of a beam propagating through a medium via $I(x) = I_0 e^{-\alpha x}$. These considerations show that ε_2 is related to absorption in the media, while both ε_1 and ε_2 are related to the real refractive index, n, which describes the phase velocity of light in the medium.
For some noble metals interband transitions can occur in the visible regime. While the Drude model describes only transitions within the conduction band, interband transitions are excitations to e.g. the d-band orbital of noble metals. These transitions give an increase in ε_2, and thus in absorption.

2.7.1 Reflectance of thin metal films

The transfer matrix method discussed in Sec. 2.2 is also valid for metals, with complex refractive index $\hat{n} = n + ik$[49]. The reflectance of light incident on a conducting surface is likewise described by Fresnel's equation (here for normal incidence)

$$R = \left| \frac{\hat{n}_2 - n_1}{\hat{n}_2 + n_1} \right|^2 = \frac{(n_2 - n_1)^2 + {k_2}^2}{(n_2 + n_1)^2 + {k_2}^2} \tag{2.7.6}$$

From Eq. 2.7.6 it is seen that if $k \gg n_1, n_2$, then $R \approx 1$ This is the reason why metals typically have very high reflectance, as k is in the range 1 to 7 for most metals[49].

Using the transfer matrix method, we can calculate the theoretical reflectance, transmittance and absorbance of a thin aluminium film, for different thicknesses. The refractive index of Al was taken from Rakić[61]. The results are shown in Fig. 2.12, and compared to the measurements of Hass *et al.*[62], and our own measurements on thin Al films on planar Ormocomp substrates. Note that for thin films the reflectance measured by Hass *et al.* is slightly lower than the theoretical reflectance. This is because the refractive index used for the theoretical calculation is that of bulk aluminium. For a thin Al film, the refractive index is dependent on the thickness of the film, as discussed by Hass *et al.*[62].

Our measurements show an even lower reflectance of the thin Al films, which is likely due to imperfections in the deposited film. Imperfections can arise when e.g. the deposition speed is slow enough to allow the metal to rearrange and cluster, or form crystals on the surface during deposition, while increased deposition rates increase the quality of the deposited films[62]. The deposition rate of Hass *et al.* was 300 Å/s, while we used a deposition rate of 15 Å/s (which was the maximum allowed deposition rate of the deposition system). The theoretical values and the values of Hass *et al.* are for a thin metal film surrounded by air on both sides. Our measurements are with a dielectric material on the back side. The variation due to this is insignificant though, even for a thickness of 10 nm.

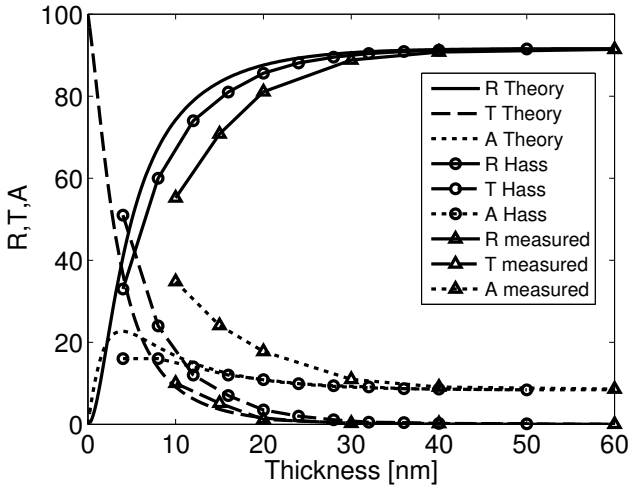

Figure 2.12: Reflectance, transmittance and absorbance for a thin planar Al film, as function of the metal thickness. The graph shows the theoretical results, compared to the findings of Hass *et al.*[62], and measurements of thin Al films on Ormocomp.

2.7.2 Surface plasmon polaritons

The electromagnetic field of light can interact closely with oscillations in the electron plasma of the metal. This leads to physical phenomena which are described by the theory of plasmonics. In general there exist three types of plasmonic excitations. Volume plasmons are quanta of oscillations in the electron sea. As discussed above these can occur above the plasma frequency, where damping is negligible. The other two types are surface plasmon polaritons (SPP), which are confined to interfaces between dielectric and conducting media, and localized surface plasmons that occur in conducting nanoparticles. An in-depth description of these phenomena is beyond the scope of this thesis, however a brief discussion of some properties of surface plasmon polaritons is given below, as these will be discussed later, in chap. 5.

SPPs are excitations that propagate along the interface of a dielectric and a conductor and occur due to coupling between an electromagnetic field, and oscillations in the conductor's electron plasma. SPPs can be described by setting up Maxwell's equations for an interface between a dielectric and a conductor and applying the appropriate boundary conditions. From this it can be shown that propagating modes exist at the interface, with the dispersion relation for the wave vector of the SPP, β,[60]

$$\beta = k_0 \sqrt{\frac{\varepsilon_1 \varepsilon_2}{\varepsilon_1 + \varepsilon_2}} \tag{2.7.7}$$

where ε_1 and ε_2 are the dielectric permeabilities of the conductor, and the dielectric respectively, and k_0 is the momentum of the photon in free space.

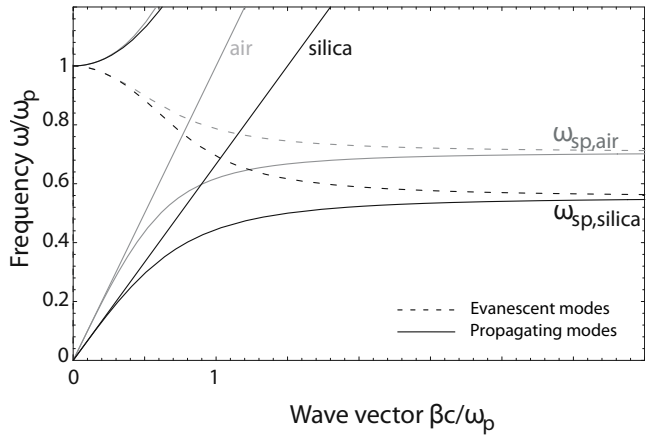

Figure 2.13: Dispersion relation of SPPs propagating along the surface of a Drude metal and air (grey curves) or silica (black curves). Figure is from Maier[60]. The legend was added by the author.

The dispersion relation of SPPs on an interface between a Drude metal, and air or silica, is shown in Fig. 2.13 (Figure from Maier[60]). The dispersion relation for light in air and silica is shown as well. The dashed lines correspond to the evanescent modes, for which light is absorbed in the metal. Above the plasma frequency, light can propagate into the metal. Fig. 2.13 shows that there is no overlap between the propagating modes in the dielectric, and the SPP mode, since the wave vector β of the SPP mode is larger than the free-space mode, for all frequencies. This means that light incident on a metal surface cannot directly excite SPP modes.

However, there are several schemes to overcome the lack of momentum, in order to allow coupling to SPPs. A periodic grating in the surface can provide the extra momentum required for the incoming light to couple to SPPs. The in-plane momentum of the incoming photons is $k_x = k\sin\theta$, where k is the total momentum of the photon, and θ is the angle with respect to normal incidence. For a 1D grating of shallow grooves with period a, wave-vector matching occurs when[60]

$$\beta = k\sin\theta \pm vg \tag{2.7.8}$$

where $g = \frac{2\pi}{a}$ and $v = (1,2,3,...)$. Scattering on a randomly structured surface, or from local scatterers can in a similar manner facilitate coupling to SPP modes. The coupling also works the other way around, so that surface structures can allow SPP modes to couple to free space light, thereby increasing losses in the SPP modes through radiation.

In instruments such as aperture mode near-field scattering optical microscope (NSOM), SPPs are excited by near field excitation. Here, a probe with an aperture $a \ll \lambda$ is placed in close contact to the metal surface. The small aperture diffracts the emitted light and ensures that the emitted light will have wave vector components k that match the wave vector β of the SPP mode[60]. In this way near field excitation can be used as a point source for SPPs, and in a similar manner, the probe can be used to collect light from SPPs as well.

Other coupling methods include prism coupling and fiber coupling. Both methods are used to excite SPPs on a metal-air interface, by coupling to the evanescent field of light in e.g. a glass. The higher refractive index of the glass provides the extra momentum required, as can be seen from Fig. 2.13.

3
Methods

The following chapter offers an introduction to some of the experimental methods used throughout the thesis. The BSi method, which is used extensively throughout the thesis to fabricate nanostructures over large areas, is introduced. We discuss a method to characterize the random BSi structures from SEM images, and describe how BSi masters are used to fabricate Ormocomp replica, in a UV-NIL process. The Ormocomp replicas allows us to characterize the optical properties of the nanostructures in a dielectric material. A fast EBL method is discussed, which will later be used for fabricating binary AR structures (Sec. 4.6). Finally, the methods for measuring reflectance and transmittance of fabricated dielectric, and metallic samples are described.

3.1 Black silicon

The BSi RIE process has been used extensively throughout this thesis, to fabricate nanostructured Si masters. The method relies on a critically tuned RIE process, which forms randomly positioned structures in Si, due to a self-masking process. Despite the random nature of the process, the fabricated structures can be controlled to some degree, in terms of e.g. structure height, spacing, and aspect ratio. The method can also been used in order to tune anisotropic RIE processes to give vertical side walls[63]: when BSi is formed, the Si wafers becomes black due to the AR effect of the structures and the absorbance of Si (hence the name). BSi has also been studied extensively for use in solar cells[64;65].

Since nanostructures can be formed over a full 4-inch wafer in less than 15 minutes, the approximate price for structuring the Si master is around € 0.5/cm^2. The fast EBL method which will be discussed in Sec. 3.5 is roughly 10^3 times more expensive than that, and with standard EBL the price is larger by a factor of around 10^4. Furthermore, the BSi process results in tapered nanostructures which are easy to replicate and demould, in UV-NIL, hot embossing, or injection moulding. The drawback of the process is of course the lack of control of the structures: it is not possible to fabricate perfectly periodic structures using the BSi process, and it is difficult to control structural parameters individually.

3.1.1 Reactive ion etching with SF_6 and O_2

The random BSi structures can be fabricated on large areas using a maskless RIE process. RIE is a combination of chemical and physical etching, where a plasma is used to supply ions that can be accelerated towards the substrate surface, causing physical etching (sputter-

ing). Furthermore the ions that are used are chemically reactive towards the substrate. This gives a synergetic environment, as the sputtering causes high mobility of the reactive species and the reactants. In turn, the etch is not entirely physical, so the chemical selectivity of the etch can be tuned. Furthermore, a very anisotropic etch can be obtained, as passivating layers can remain on the side walls, but are being sputtered away on the surfaces normal to the sputtering direction.

BSi etches can be performed in many different ways. The simplest one uses just SF_6 and O_2 gases[64;65]. SF_6 supplies the fluorine atoms that can react with Si to make a volatile SiF_4 gas. The oxygen can react with fluorine and Si to make a passivating layer of $Si_xF_yO_z$. The etching process relies on the initial surface roughness of the wafer. This roughness can be due to the roughness of the native oxide of the Si wafer, or it can be induced initially in the etching, due to the etch not being perfectly homogeneous. Any protrusion that would exist or be formed on the surface will be slightly more protected by the passivating layer, than the planar regions of the surface (See Fig. 3.1). As the etching continues, any roughness will be enhanced and eventually form cone- or needle like structures.

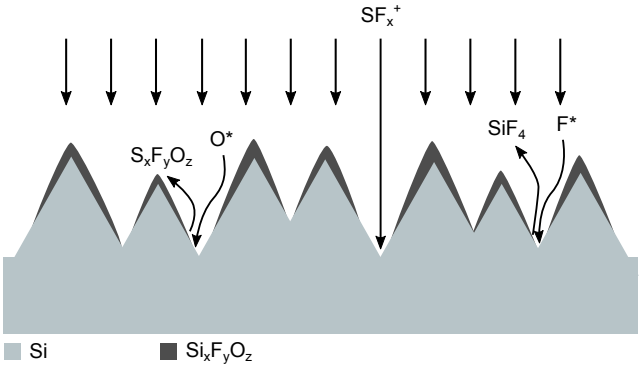

Figure 3.1: Formation of BSi in a maskless RIE process, using SF_6 and O_2. Fluorine radicals etch the Si while oxygen can react with fluorine and Si to make a passivating layer. The passivation on the inclined walls on small protrusions is more resistant to the ion bombardment, so the protrusions will remain protected from the etch. The protrusions will therefore increase in height as the surrounding Si is etched away, eventually leading to cone or needle like structures. The illustration is modified from Schnell *et al.*[64].

3.2 Fourier SEM method

The random nature of the BSi process, makes it difficult to exactly characterize the geometry of the structures. In this thesis we used a Fourier transform of top view SEM images of the surfaces, to determine a characteristic length scale for the different structures. A similar method was used by Schroeder *et al.* and Yoshida *et al.* [66;67].

Top view SEM images were recorded using a fast scan rate, to minimize the effect of drift on the measurement. The noise in the image does not influence the result, as it has a much higher frequency than the structures. Images with a width of 10 µm were used for the analysis. The discrete 2D Fourier transform F has the form

$$F(k,l) = \sum_{n=0}^{N-1} \sum_{m=0}^{M-1} g(m,n) e^{-i2\pi\left(\frac{mk}{M}+\frac{nl}{N}\right)} \tag{3.2.1}$$

where g is the intensity image with $N \times M$ pixels, generated by the SEM. The power spectral density (PSD) is calculated as

$$PSD = |F(k,l)|^2 \tag{3.2.2}$$

The PSD was calculated using a Matlab[59] script. Figure 3.2 (a) shows the PSD of a typical BSi surface. The rotational symmetry shows that the surface is isotropic. The Fourier transformed image was then averaged by azimuthal integration over θ, as shown in Fig. 3.2 (a). The integrated PSD is shown in Fig. 3.2 (b) and shows that the surface is not completely stochastic, as there is a peak in the spectrum, which witnesses of a characteristic length scale of the structures. This lenght scale is calculated by fitting two lines on each side of the peak, as shown in 3.2 (b). The grey areas indicate the range of these fits. These ranges were manually set, for each surface. The characteristic frequency of the image is then calculated as the intersection between the two lines. The confidence interval on the intersection is calculated from the confidence interval of the two fitted lines, using propagation of errors[68]. In this example, the characteristic length scale was 185 ± 25 nm, where the confidence interval corresponds to a single standard deviation.

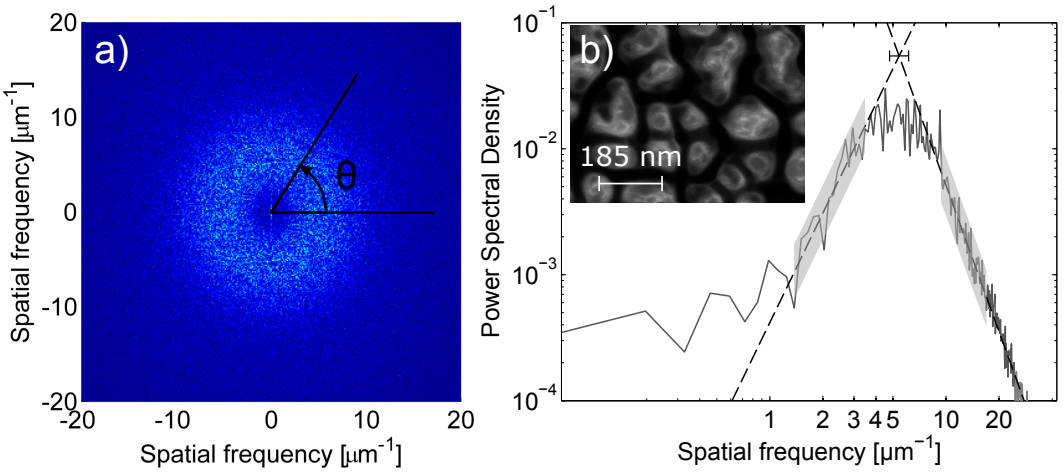

Figure 3.2: Power spectral density from SEM images. a) The 2D Fourier spectrum of an SEM image of a typical BSi surface b) The power spectral density after azimuthal averaging of the 2D Fourier spectrum. The shaded areas show the range of the two line fits. The characteristic wavelength is given as the intersection between the two lines. The confidence interval of the calculated frequency is shown. Here the characteristic length scale is 185 ± 25 nm, which is shown in the insert.

It should be noted that SEM does not generate a topographic image of the surface. However, due to the tapered nature of these structures, the intensity map from SEM roughly corresponds to the topography of the surface. This is due to the edge blooming effect of SEM, causing a large signal to be recorded from the apex of the structures. For other structures such as binary gratings, the edges of the structures would show a large signal in the SEM image, which could result in a misleading result from this technique. The robustness of this method was checked on BSi structures, by varying e.g. the image contrast settings, and acceleration voltage. No significant change on the calculated characteristic length scale was observed, when changing the image contrast, or when varying the acceleration voltage from 0.5 keV to 20 keV.

3.3 Ormocomp

In order to assess the optical properties of the nanostructures fabricated on Si masters, the structures were replicated into the UV-curable resin, Ormocomp. The fabrication method for this process is discussed in Sec. 3.4, but first the basic properties of the material will be discussed.

Ormocomp belongs to a class of organic-inorganic hybrid polymer materials, called Ormocers (ORganically MOdified CERamics), which are produced by Microresist Technology GmbH[69]. These materials consist of an organic and inorganic network, making it a hybrid between a glass (or ceramic), and a polymer.

Ormocomp is fabricated using the sol-gel method, where monomers are linked together by Si-O-Si bonds, by a series of hydrolysis and condensation steps, forming oligomers with sizes of 2-5 nm. The precursor for Ormocomp is a monomer without a systematical name[70]. A colloidal gel is formed, and at this stage photo-initiators that can link the organic parts of the gel, are added. The product is sold at this stage, as a viscous resin, without solvents. The photo-initiators can be inhibited by reacting with oxygen from the surrounding atmosphere. This can form an inhibition layer, a few nanometres thick for Ormocomp. The inhibition layer can be several micron for other Ormocers, such as Ormocore[71]. One of the advantages of Ormocers is that it contains no solvents, so that the shrinkage during curing is very low (5-7%)[72]. There are different types of Ormocers, each developed for specific purposes. Ormocomp was developed for optical elements such as gratings, micro lenses and prisms.

The optical properties of a fabricated planar Ormocomp film was measured using ellipsometry (M-2000V, J.A. Woollam). The measured refractive index is shown in Fig. 3.3, along with the theoretical reflectance, calculated using the Fresnel equation, Eq. 2.1.3.

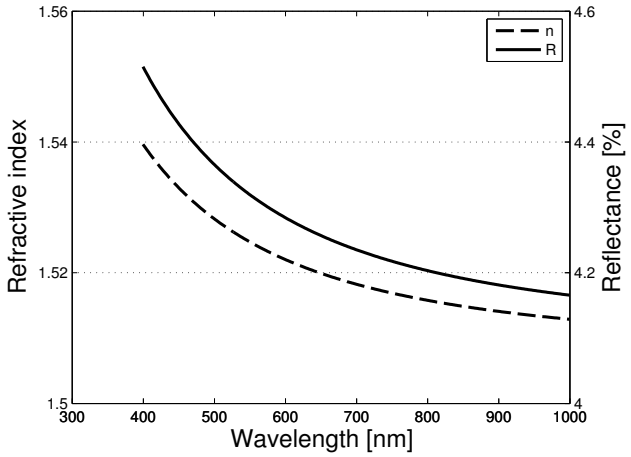

Figure 3.3: Refractive index of Ormocomp, and theoretical reflectance, calculated using Fresnel's equation 2.1.3. The refractive index was measured using ellipsometry.

3.4 Ormocomp fabrication process

Ormocomp was used to fabricate replicas of the nanostructured Si masters, in order to assess the optical functionality of the fabricated nanostructures in a dielectric material.

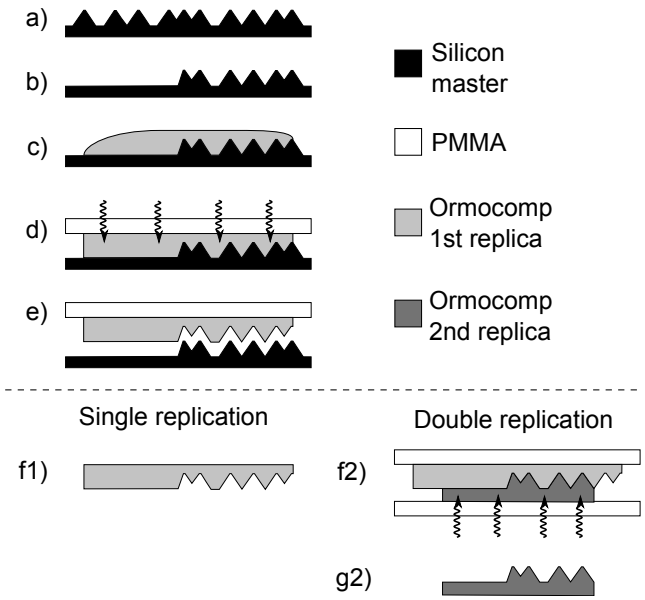

Figure 3.4: Ormocomp fabrication process. a) Nanostructured Si master (structures denoted polarity A). b) BSi masters could be patterned by photolithography and isotropic RIE, or by powder blasting. c) After FDTS coating of Si master, Ormocomp was applied and a PMMA substrate was used to planarize the Ormocomp. d) Ormocomp was cured by exposure to UV light, through the PMMA substrate. e) The flexibility of the PMMA substrate allowed the replica to be demoulded easily. f1) A single replication process resulted in polarity B Ormocomp replica. f2) In a double replication process, the first replica was coated with FDTS and used as master for a second replication, resulting in polarity A structures.

The fabrication process is outlined in Fig. 3.4. The Si masters were fabricated using the BSi method, of by EBL (3.4 (a)). BSi masters could be patterned by UV lithography and an isotropic RIE process, removing the BSi nanostructures in the unmasked areas (3.4 (b)). Alternatively the BSi masters were patterned by a powder blasting process: here the BSi structures were masked with a blue film, which was then patterned using a CO_2 laser. The wafers were then powder blasted, using the patterned blue film as a mask. The masters were then cleaned and coated with perfluorodecyltrichlorosilane (FDTS) using molecular vapour deposition (MVD 100 Molecular Vapor Deposition System, Applied Microstructures Inc.). Ormocomp was applied using a pipette and a PMMA substrate was placed on top, in order to level the surface (3.4 (c)). The Ormocomp was then cured by exposure to UV light through the PMMA substrate (3.4 (d)), using a UV flood exposure source (1000 W Hg(Xe) Oriel Flood Exposure Source, unit 92540). The PMMA substrates were Plexiglas XT 20070 which has a limited but sufficient transmittance in the 260-320 nm wavelength range. After UV exposure, the flexibility of the Ormocomp and PMMA allowed for a gradual release of the Ormocomp film from the BSi master, while the Ormocomp remained attached to the PMMA (3.4 (e)).
At this point, the Ormocomp sample could be released from the PMMA substrate, and heated to 110° for 3 minutes, in order to activate any remaining photo-initiators. This is referred to as a single replication process, and results in structures with opposite polarity the Si masters (3.4 (f1)). The polarities of the Si master and the replicas are referred to as

polarity X and polarity Y respectively.
Alternatively a double replication process was employed, in order to obtain polarity A replicas, as depicted in Fig. 3.4 (f2). Here, the first replica was coated with FDTS, and used as master for a second replica, following the steps of (b-e). The result was a polarity A Ormocomp replica (g2). Both single and double replication resulted in Ormocomp samples with a thickness of roughly 200-300 μm, which could be easily handled.

3.5 Electron beam lithography

This thesis deals with fabrication of nanostructures on large areas, so it is relevant to discuss the limitations of EBL, which is considered as a prototyping tool as it is typically a very slow (and expensive) technique. In this section we cover some simplified calculations for the writing time, when exposing nanostructures using an electron beam writing system. Furthermore a method for significantly increasing the writing speed, at the cost of resolution, is discussed. This fast EBL method will later be used for fabricating binary AR nanostructures (see Sec. 4.6).

In a simplified description the total e-beam writing time is composed of three parts: exposure time, beam time, and stage time. Exposure time is the time required to expose the resist. The beam time is used when moving the beam from one element to the next. The stage time is for moving the stage to a new writing field[73]. The exposure time is given as[74]:

$$T_{\text{exposure}} = \frac{DA}{I} \tag{3.5.1}$$

where D is the required exposure dose, I is the beam current and A is the total area to expose. The e-beam writer is blanking the beam between each exposure, with a dwell time, t_{dwell}, of

$$t_{\text{dwell}} = \frac{D\Delta x^2}{I} \tag{3.5.2}$$

where Δx is the shot pitch. The minimum dwell time is $t_{\text{dwell}} = 100$ ns, which is due to the maximum frequency of the beam blanker which is 100 MHz for the JEOL JBX-9500FS EBL system which was used in this thesis. This means that the beam blanker frequency in practice sets the upper limit of the current, to avoid over exposure.

The beam time is the time it takes for the sub-deflector to move the beam from one element to the next, as sketched in Fig. 3.5 (not between each exposure within the same element). For the JEOL JBX-9300FS EBL system which has been described by Takemura *et al.*, the beam time was $\tau_{\text{beam}} = 5$ μs[73] (this has not been confirmed for the JBX-9500FS system, but here we will assume it is the same). Thus, as a rule of thumb, the beam time becomes significant when the number of elements exceeds 10^6. This is in general not a problem when exposing lines, but for large 2D arrays of nanostructures, the number of elements can easily exceed 10^6. For a 2D array of structures, the total beam time T_{beam} can be estimated as

$$T_{\text{beam}} = \frac{A}{\Lambda^2}\tau_{\text{beam}} \tag{3.5.3}$$

where Λ is the period of the 2D array of nanostructures.

The total writing time can now be estimated from the exposure and beam time (disregarding stage time, and other factors which further increase the writing time), as $T_{\text{Total}} = T_{\text{exposure}} + T_{\text{beam}}$. For a shot step of $\Delta x = 4$ nm, $D = 200$ μC cm^{-2}, $I = 3$ nA, shot area A=0.5 cm^2, beam settling time $\tau = 5$ μs, structure period $\Lambda = 150$ nm, the exposure time is approximately 9 hours, and the beam time is 6 hours. So the total writing time for a 1 cm^2 of sub-wavelength nanostructures with a volume fraction of $f = 0.5$, is around 15 hours.

3.5.1 Fast EBL

A fast EBL technique was discussed in a paper by Gadegaard *et al.* in 2003[19], and in a recent paper by Højlund-Nielsen *et al.*[75]. The method is to define each structure with a single exposure from the electron beam, as outlined in Fig. 3.5. The method aims to eliminate the beam time, while increasing the current - both work to decrease writing time significantly. The current can be increased, as a relatively large area is exposed at each shot. The maximum possible current increases in accordance with Eq. 3.5.1 and the dwell time is no longer an issue due to the large Δx. The current can be significantly increased and the beam time is practically zero. Using the fast writing method, the theoretical exposure time can be calculated from Eq. 3.5.1. For a 1 cm^2 square array of dots with period $\Lambda = 150$ nm and 100 nm diameter, the writing time is approximately 1 hour, assuming a current of 30 nA, and a required dose of 200μC cm^{-2}.

The fast EBL method can thus decrease the processing time by a factor of around 15, compared to a standard EBL process. The method is interesting for applications such as binary AR nanostructures, which depend on only the volume fraction, and not the exact shape of each of the nanostructures. Binary AR structures fabricated with fast EBL will be discussed in Sec. 4.6.

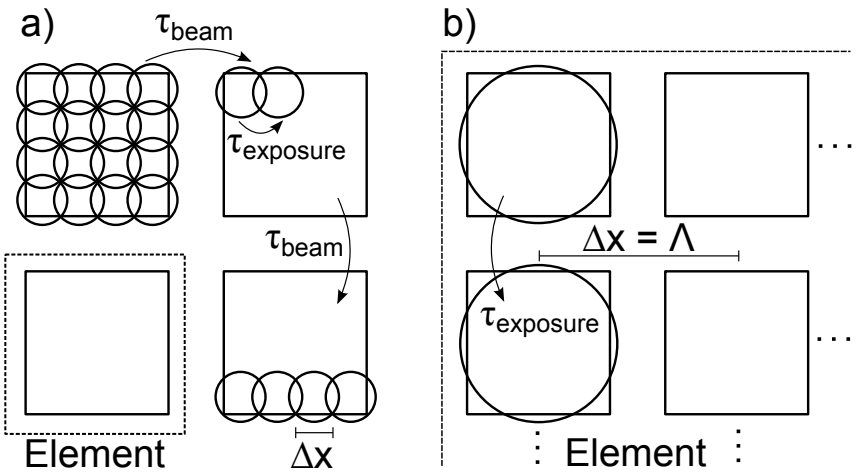

Figure 3.5: Concept of standard and fast electron beam lithography. a) Standard writing method. Each element is exposed by multiple shots, ensuring high resolution, but low speed. b) Fast writing method where each element is exposed in a single shot. The control of the exposed features is reduced, but writing speed can be significantly increased.

3.6 Optical measurements

3.6.1 Transmittance measurements

A setup for measuring broad band transmittance was designed and built. A sketch of the setup is shown in Fig. 3.6. Samples were illuminated with a white light source from a xenon lamp (HPX-2000, Ocean Optics[76]). The light was collected from the light source in a multi mode optical fiber, and emitted through a collimator. The light was transmitted through the sample, collected by a second collimator and detected with a spectrometer (Jaz, Ocean optics). Both collimators were placed in kinematic mounts allowing precise alignment of the beam, and samples were aligned perpendicular to the beam, using a goniometer. The collimator for the incident light beam was chosen with a relatively long focal length (10.9 mm) to ensure a well collimated beam, at the expense of a slightly larger spot size. Typically the reference measurement was a free space measurement.

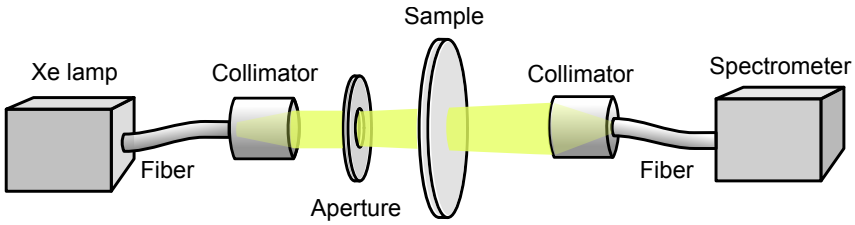

Figure 3.6: Sketch of the direct transmission measurement setup. Both collimators were placed in kinematic mounts allowing precise alignment of the beam, and samples were aligned perpendicular to the beam, using a goniometer.

3.6.2 Integrating sphere

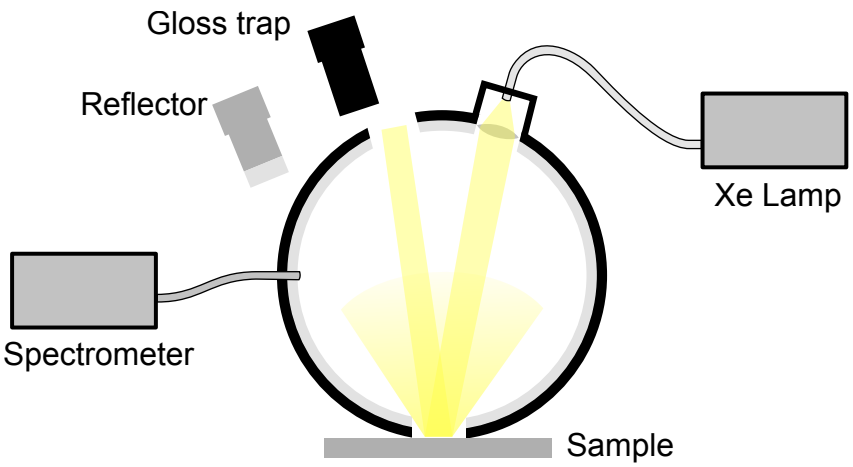

Figure 3.7: Sketch of the integrating sphere. The sample is illuminated at 8° incidence, by collimated white light. The light is reflected multiple times from the walls of the sphere, before it is collected and analyzed with a spectrometer. Specular and diffuse reflectance can be distinguished by using a gloss trap to absorb the specular reflected light.

Reflectance measurements were performed with an integrating sphere (ISP-50-8-R-GT, Ocean optics[76]). The integrating sphere setup is sketched in Fig. 3.7. The light was incident at an angle of 8° from normal incidence. After being reflected from the sample, the light was scattered isotropically from the walls of the sphere, and the light was collected at

an exit port, placed at 90° from normal to the sample surface. A gloss trap could be used to absorb the specular reflected light, allowing to distinguish between the specular and diffuse reflectance of a sample.
The integrating sphere measurements require a reference measurement, in order to measure absolute reflectance. Here we used a borosilicate float glass wafer, or a 100 nm thick Al film on borosilicate float glass, which was deposited using e-beam vapour deposition (Alcatel SCM 600).

4

Papers

This chapter presents the main results on nanostructured dielectric materials. The results are presented in the form of papers which have been published as part of this Ph.D. thesis (except for paper V which is an unpublished manuscript). The chapter begins with a short introduction and summary of each of the papers, in order to give an overview of the main results. The papers then follow in their full lengths, concluded by a discussion of the results. The layout of the papers, and certain figures have been reformatted to conform to the format of the thesis, but have not otherwise been altered from the published papers, save for occasional typos.

4.1 Extended abstracts

The main scope of this thesis is to show prototypes of nanostructured surfaces with optical functionality, which can be fabricated using high volume production methods like injection moulding. Antireflective nanostructures have been studied in particular. Furthermore, the work has been focused on fabrication methods which are relatively inexpensive, and capable of fabricating nanostructures on large areas. The main method of fabrication has been with the use of BSi, as described in Sec. 3.1. The structures for BSi masters were transferred to Ormocomp, as described in Sec. 3.4, or from PDMS stamps (this method will be introduced in paper I). Binary AR structures fabricated using fast EBL is discussed in paper V which is an unpublished draft for a manuscript.

Paper I discusses the optical properties of micron sized BSi Ormocomp structures, showing the scattering properties of such structures[77].

Paper II is likewise about BSi structures in Ormocomp, but here with the focus of minimizing the scattering, and showing that BSi structures can be used to fabricate AR structures[78].

Paper III gives a general introduction to the optical properties of polymers, and the fundamental limitations that injection moulding and hot embossing imposes on the nanostructures. In particular, the feasibility of achieving angle-independent colour functionality by injection moulded nanostructures in polymers is discussed[79].

Paper IV discusses injection moulding of the antireflective structures discussed in paper II. Here, a Ni shim was electroplated from a BSi master which was optimized according to the results of paper II, and used as a mould for injection moulding[80].

Paper V is an unpublished draft of a manuscript which discusses the fabrication of antireflective binary AR structures using fast EBL.

4.1.1 Summary of paper I

The paper discusses the scattering properties of BSi structures with lateral sizes around 1 µm. Polydimethylsiloxane (PDMS) replica were made from BSi masters, and used as a stamp for imprinting the structures in Ormocomp. It was found that different types of structures would selectively scatter light with wavelengths in a certain range. Structures that scattered the blue light more than the red, thus functioned as a red filter for the directly transmitted, non-scattered light. Other structures resulted in green or blue filters. The scattering properties were calculated from AFM data using scalar diffraction theory, and the results showed good agreement with the optical measurements. The results show that not all types of BSi structures are viable for being used as AR structures, as the dielectric substrates become translucent due to scattering, if the structures are too large.

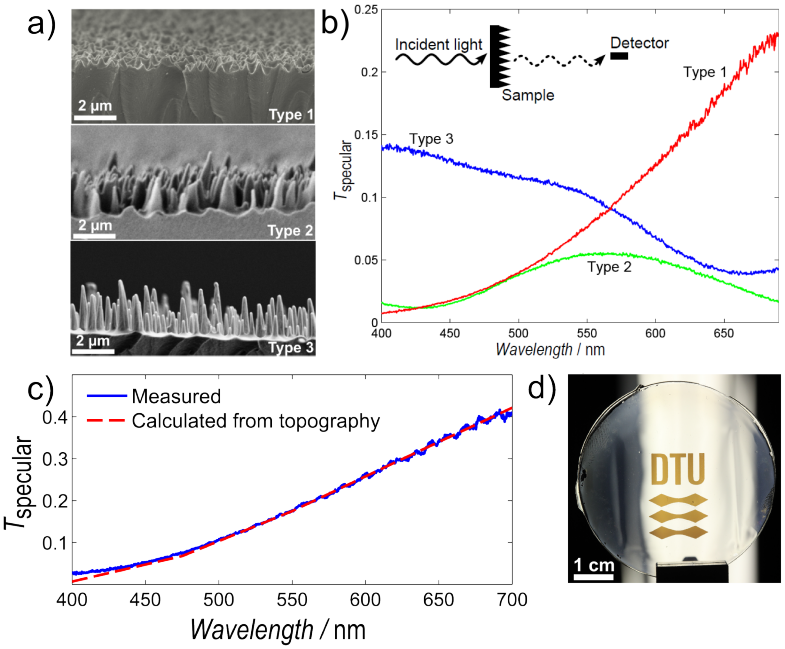

Figure 4.1: Summary of paper I. a) SEM images of BSi nanostructures in Ormocomp. b) Specular transmittance measurements of the three samples. c) Specular transmittance of type 1 sample, compared to theoretical transmittance, calculated from AFM data using scalar diffraction theory. d) Photograph of type 1 structures (DTU logo), when illuminated from the backside by a white light source.

Figure 4.1 summarizes the main results of the paper. The black silicon structures were replicated in Ormocomp, by casting a PDMS stamp from the BSi master. The PDMS stamp was used as a stamp in a UV-NIL process, to transfer the structures to an Ormocomp film on a glass substrate. SEM images of the structured Ormocomp samples are shown in Fig. 4.1 (a), and Fig. 4.1 (b) shows the specular transmittance of the three different samples. The spectra shows that the different BSi structures result in blue, red and green transmitted light. Fig. 4.1 (c) shows the specular transmittance of a type 1 sample, compared to the theoretical transmittance calculated from AFM data of the surface topography, using scalar diffraction

theory. This result underlines that the structures are not in the effective medium regime. Angle resolved measurements showed that the different colours were due to selective scattering on the surface. The red transmitted light for example, occurs because the transmitted blue light is scattered away from the specular direction. A photograph of the effect is shown in Fig. 4.1 (d). The structures area of type 1, and the reddish colour of the transmitted light is evident.

4.1.2 Summary of paper II

From the previous paper it is evident that not all BSi structures are viable for use as AR structures, due to scattering of light. Often the term sub-wavelength is used about BSi structures, although the term originates from periodic structures, as discussed in Sec. 2.3. While there is a clear condition for zero'th order diffraction from periodic structures, the situation is different for randomly structured surfaces.

In the second paper we find a characteristic length scale in the random BSi structures, using Fourier transformation of SEM images. This characteristic length scale can be compared to the period of periodic structures. We proceed to find an empirical relation between this characteristic length scale, and at which wavelength scattering becomes significant. Again, this relation can be compared to the zero'th order diffraction condition (Eq. 2.3.2) for periodic structures.

Figure 4.2 summarizes the main results of paper II. The different types of BSi structures are shown in Fig. 4.2 (a). Ormocomp replicas of these masters were fabricated using a double UV-NIL process, as described in Sec. 3.4. The transmittance of the Ormocomp samples is shown in Fig. 4.2 (b), along with the transmittance of a planar Ormocomp sample. For longer wavelengths, the transmittance of the structured samples is larger than for the planar, which is evidence of the antireflective effect of the structures. However, for smaller wavelengths the transmittance of the structured surfaces drops, due to scattering. The critical wavelength at which the transmittance crosses that of the planar, is compared to the characteristic length scale of the nanostructures, as shown in the insert in Fig. 4.2 (b). The type A structures where used to fabricate an Ormocomp sample with nanostructures on both faces, as shown in Fig. 4.2 (c). The left side of the sample is planar, showing the difference in reflectance properties of the planar and nanostructured surfaces. An SEM image of the border between the planar and nanostructured side is shown below (for the Si master).

Further discussions

The empirical relation we find in the paper is plotted in Fig. 4.3 (dashed line and square markers). The method used in the paper was also applied to the results of Schulz *et al.* [24]. The characteristic length scale of the structures was measured from the SEM image shown in Fig. 1.8 (a). The critical wavelength λ_c was taken as the intersection between the graph for reflectance of a planar and a structured sample at 0° incidence (Fig. 1.8 (b)). This data point was plotted along with the results of paper II, in Fig. 4.3, showing that the result of Schulz *et al.* follows the relation found in paper II.

Fig. 4.3 also shows the condition for zero'th order diffraction, Eq. 2.3.2, at normal incidence and a refractive index of $n = 1.6$, which is the refractive index of polycarbonate for

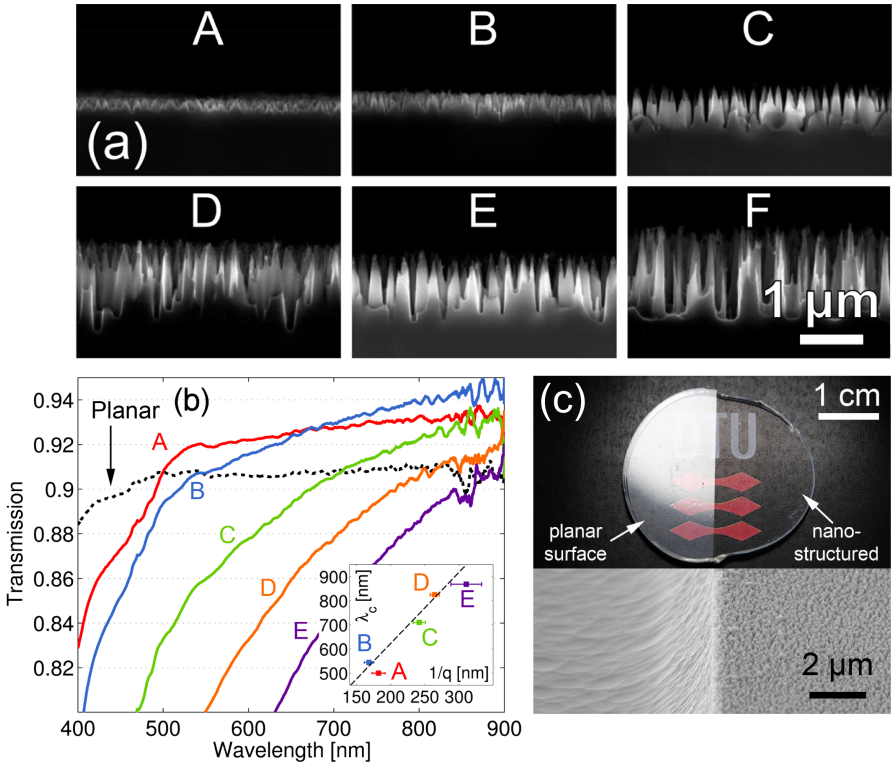

Figure 4.2: Summary of paper II. a) SEM images of BSi masters. b) Specular transmittance spectra of the Ormocomp replica. The drop in transmittance is due to scattering. c) Photograph of an Ormocomp sample with type A nanostructures on both faces (right side), compared to planar faces (left side). An SEM image of the border between the planar and nanostructured region is shown below (for the Si master).

wavelengths of around 500 nm[81]. The graph is compared to the results of Jang *et al.*, discussed in Sec. 1.2.2. The cut-off wavelengths were extracted from the results in Fig. 1.10, and plotted in Fig. 4.3. As seen, the experimental data is in good agreement with the theory.

The relation between the characteristic length scale of the random nanostructures and the onset of scattering, can be used as a design parameter for achieving non-scattering random AR nanostructures. Comparing the relation to the diffraction limit, further reveals that the required length scale of random AR structures is significantly smaller than for periodic structures. This ultimately means that the use of random AR structures require a better resolution of the fabrication process, than periodic structures.

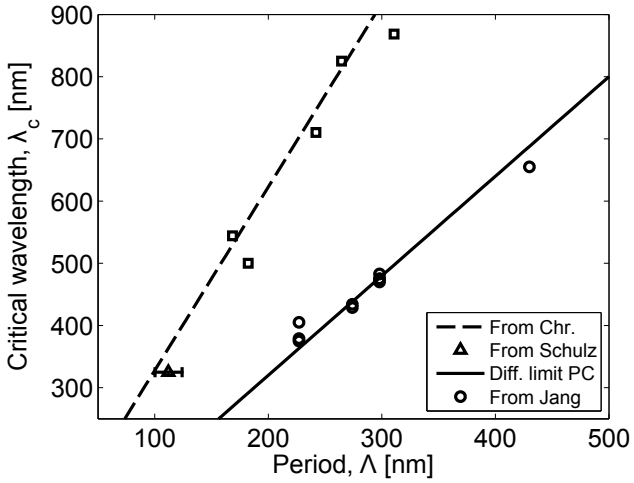

Figure 4.3: Critical wavelength of random structures and the diffraction limit of periodic structures. The dashed line is the empirical relation found in paper II. The triangular marker represent the results from Schulz *et al.* (see Sec. 1.2.1). The circles represent the measured onset of diffraction from periodic structures, from Jang *et al.*[26]. The solid line is the diffraction limit as given in Eq. 2.3.2, for a refractive index of $n = 1.6$ (an approximate value for polycarbonate[81]), at normal incidence.

4.1.3 Summary of paper III

The proceedings paper discusses the possibilities and limits for injection moulding or imprinting optically functional nanostructures in polymers. Some fundamental properties about the reflectance of light from polymer surfaces are discussed, followed by a discussion of different methods for achieving AR and colour functionality using surface structures.

One of the limitations for colour effects, is the low refractive index of polymers which is typically in the range $n = 1.5$ to 1.6. As shown in Fig. 4.4 (a), this limits the reflectance from a polymer surface to 4-5% for normal incidence, and around 15% when integrating the reflectance for all incident angles.
Colours with some degree of angle independence can be achieved by sub-wavelength nanostructures. Such structures form a layer with an effective refractive index, given by the volume fraction (in paper III referred to as filling factor) of the surface structures (as discussed in Sec. 2.6). Figure 4.4 (b) shows a colour-map which was calculated from RCWA simulations of 350 nm tall structures in a square array, with different volume fractions and periods. Different colours can be achieved by varying the volume fraction of the structures. However, in practice, the colour effect will be very limited due to the low reflectance from polymer surfaces.

The paper offers some ideas to overcome this problem. One is to utilize diffraction gratings, which reflect light into specific diffraction orders, according to the period of the surface structures. This gives a strong optical effect, because the 4% reflected light is concentrated in a few diffraction orders. The drawback is of course that the colour effects are highly dependent on the viewing angle, and lighting conditions. In order to make a pseudo angle-independent effect, the diffraction gratings were therefore ordered in small pixels, each with different grating period and orientation. Photographs of such arrays are shown in Fig 4.4 (c), for pixel sizes ranging from 800 µm to 50 µm. The samples were fabricated by hot embossing in PMMA, from a Si master. Figure 4.4 (d) shows an AFM image of an intersection between four different pixels. The pixels ensure that diffracted light is seen at all viewing angles. These structures were used for tests and pilot productions in the Nanoplast project, and have been injection moulded on both planar and double-curved surfaces. Figure 4.5 shows an injection moulded sample, which utilizes this design.

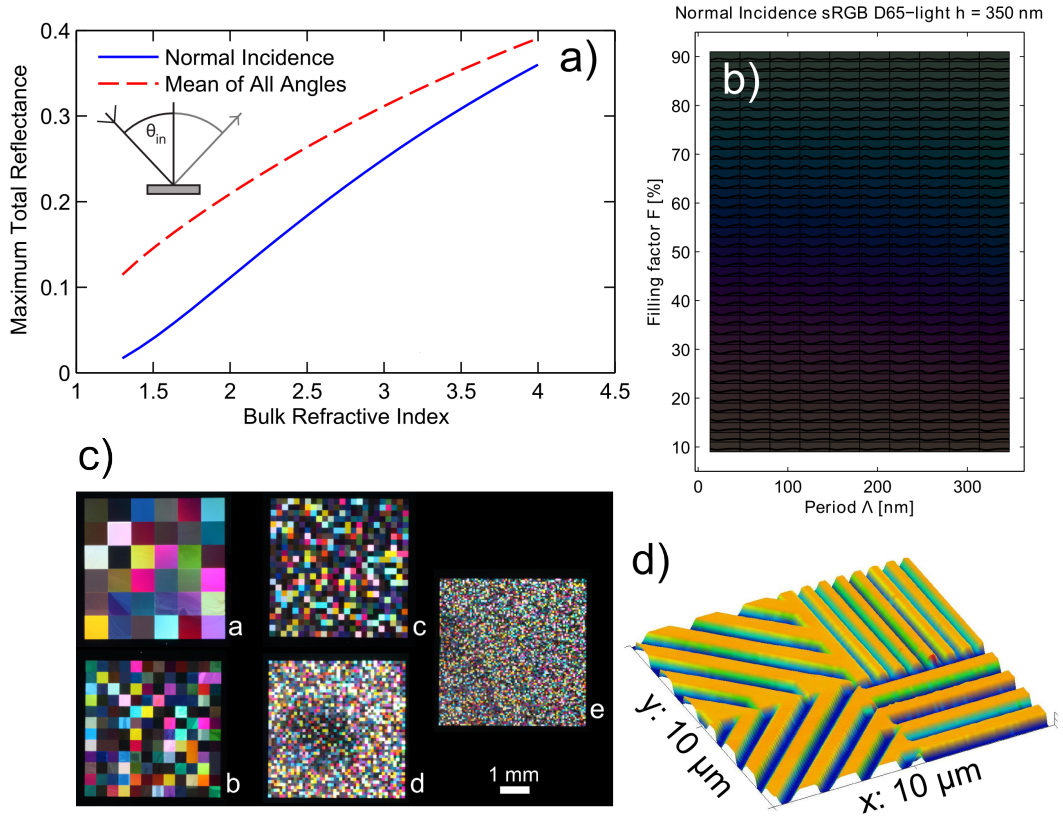

Figure 4.4: Summary of paper III. a) Calculated reflectance at normal incidence, and integrated over all angles, as function of refractive index. The reflectance of polymers with refractive index $n = 1.5$, is around 4% which limits the potential for achieving colour effects from surface nanostructures. b) Colour-map based on RCWA simulations of sub-wavelength nanostructures. Colour functionality can be achieved, but the visual effect is limited due to the low reflectance of polymers. c) Photographs of diffraction grating pixel arrays in PMMA. d) AFM image of the Si master, showing four different gratings.

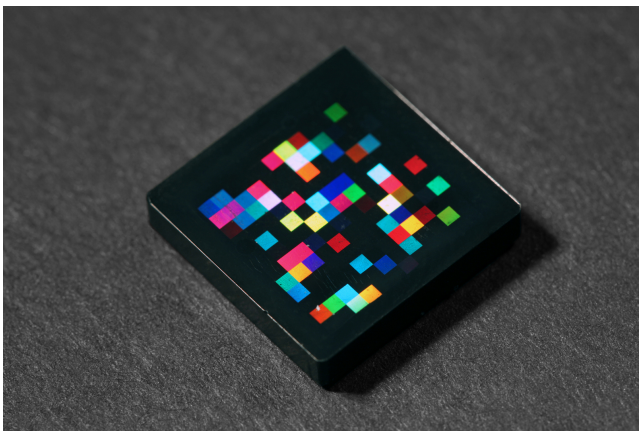

Figure 4.5: Injection moulded part with diffraction grating pixels. From pilot production in the Nanoplast project. The part is 1.6×1.6 mm^2. Photo by Jesper Scheel, DTU Nanotech.

4.1.4 Summary of paper IV

The paper describes how the antireflective BSi nanostructures discussed in paper II can be fabricated using injection moulding. A Ni shim was electroplated from a BSi master with the type A structures described in paper II. The Ni shim was FDTS coated, and inserted in an injection moulding tool. Polypropylene (PP) parts were injection moulded with cycle times of 35 seconds. The project was done in collaboration with Toolpartners[82] and LEGO Systems A/S[83] - partners in the Nanoplast project.

Figure 4.6 (a) shows SEM images of the original BSi master, and of the injection moulded PP part. The nanostructures were transferred to the injection moulded parts, although AFM images showed that complete filling was not achieved (Fig. 4.6 (b)). AFM images were also used to find the volume fraction gradient facilitated by the surface structures. As discussed in Sec. 2.5, this gradient gives rise to the AR effect. Since the structures did not show significant scattering in the visible spectrum, EMT could be used to extract the refractive index profile of the nanostructured surfaces, from AFM images. The injection moulded PP parts were compared to an Ormocomp replica of the Ni shim. Fig. 4.6 (c) shows measured reflectance spectra (measured with an integrating sphere as described in Sec. 3.6.2), compared to theoretical predictions based on EMT and AFM data. The measured and theoretical results show good agreement, and the reflectance of the PP parts was reduced from $4.5 \pm 0.5\%$ to $2.5 \pm 0.5\%$. This reduction was enough to give a significant optical effect, as seen in Fig. 4.6 (d), which shows a black injection moulded PP part in specular lighting conditions. The darker nanostructured areas are indicated by arrows.

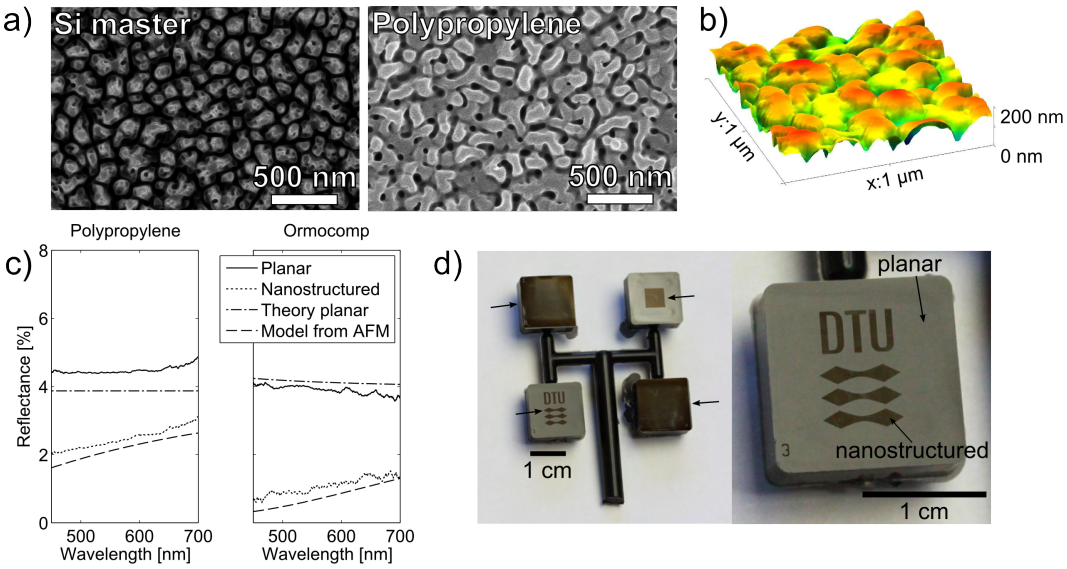

Figure 4.6: Summary of paper IV. a) SEM images of BSi master, and injection moulded polypropylene part. b) AFM image of injection moulded PP. c) Total integrated reflectance of injection moulded part, and Ormocomp replica of Ni shim. The measured spectra are compared to the theoretical reflectance calculated from AFM data using EMT. d) Photographs of injection moulded sample in black polypropylene. Nanostructured areas are darker than the planar surfaces.

Further discussions

A second test was later conducted at LEGO, after installation of a modified injection moulding tool, which allowed to go to a higher holding pressure during the process. It would have been instructive to use a transparent material in order to compare the optical properties to the results discussed in paper II. However, tests were still limited to opaque PP, as the tool was not able to go to the increased temperatures needed for injection moulding e.g. polycarbonate. A series of tests were made, using varying holding pressure from 300 bar to 2000 bar. The samples were characterized as the samples in the paper. The results are shown in Fig. 4.7 (a). It is seen that the reflectance is lowered, as the injection pressure is increased, as would be expected. However, at 1300-1800 bar, it seems to stabilize, and the antireflective effect is not improved further.

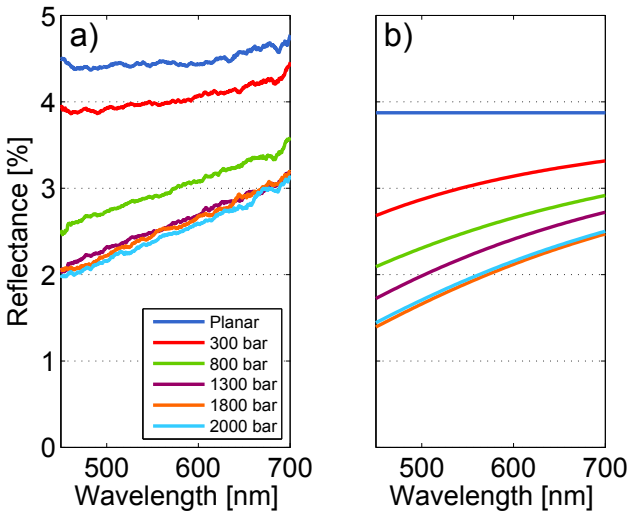

Figure 4.7: a) Measured total integrated reflectance spectra of injection moulded AR structured surfaces. b) Theoretical reflectance of injection moulded surfaces, calculated using effective medium theory and AFM data.

The injection moulded samples were likewise characterized with AFM, and the theoretical reflectance was calculated from the volume fraction profile. The results are shown in Fig. 4.7(b), and shows the same trend as the optical measurements, although the overall reflectance is slightly lower.

4.1.5 Summary of paper V

Paper V is a draft for a manuscript, which discusses the fabrication of binary AR nanostructures in Ormocomp, by casting from a Si master. The Si master was fabricated using the fast EBL method discussed in Sec. 3.5, where each structure is defined by a single exposure to the electron beam. The method reduces the resolution but significantly decrease the fabrication time, and thereby the cost.

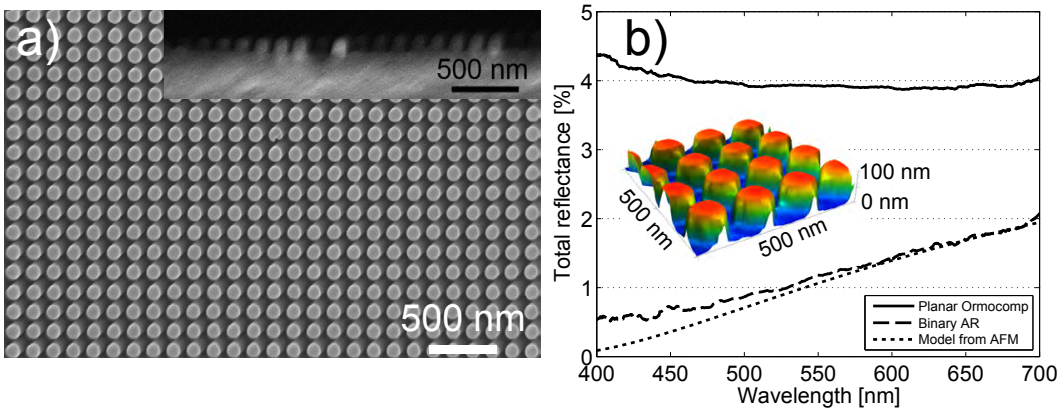

Figure 4.8: Summary of paper V. a) SEM image of AR nanostructures in Ormocomp. The insert shows a profile of the structures. b) Measured reflectance of planar and nanostructured Ormocomp. The reflectance is compared to the theoretical reflectance, calculated from an AFM image of the surface, using EMT.

Figure 4.8 summarizes the results of the manuscript. A Si master for binary AR structures was successfully fabricated using the fast EBL method, over a 0.25 cm^2 area. The master was used to replicate the structures to Ormocomp, using the single replication process described in Sec. 3.4. The fabricated Ormocomp structures are shown in Fig. 4.8 (a). The reflectance of the nanostructured sample was measured using an integrating sphere, as described in Sec. 3.6.2. The measured reflectance of a planar and nanostructured sample is shown in Fig. 4.8 (b). The reflectance was compared to the theoretical reflectance, calculated from an AFM image of the surface, using EMT. The structures had been designed to have a mumming reflectance for wavelengths of 500 nm. The measured reflectance show that the minimum had been shifted towards lower wavelengths. This was due to the structures being slightly lower than expected (93 nm instead of 100 nm). Furthermore, the replication process does not result in perfectly binary structures, but can be described by the 8th order super-Gaussian structures discussed in Sec. 2.6.2. The binary AR structures showed a decrease in reflectance from roughly 4% for a planar sample, to 0.5% at 400 nm wavelength, and 2% at 700 nm wavelength.

4.2 Paper I - Color effects from scattering on random surface structures in dielectrics

Authors

Jeppe S. Clausen[a], Alexander B. Christiansen[b], Jørgen Garnæs[c] ,N. Asger Mortensen[a], and Anders Kristensen[b].
[a]Department of Photonics Engineering, Technical University of Denmark, Oersteds Plads, Building 343, DK-2800 Kgs. Lyngby, Denmark.
[b]Department of Micro and Nanotechnology, Technical University of Denmark, Oersteds Plads, Building 345B, DK-2800 Kgs. Lyngby, Denmark.
[c]Danish Fundamental Metrology, Matematiktorvet, Building 307, DK-2800 Kgs. Lyngby, Denmark.

Abstract

We show that cheap large area color filters, based on surface scattering, can be fabricated in dielectric materials by replication of random structures in silicon. The specular transmittance of three different types of structures, corresponding to three different colors, have been characterized. The angle resolved scattering has been measured and compared to predictions based on the measured surface topography and by the use of non-paraxial scalar diffraction theory. From this it is shown that the color of the transmitted light can be predicted from the topography of the randomly textured surfaces.

Introduction

Nature has demonstrated optical effects such as antireflection and colors based on micro and nanostructures. Well known examples are anti reflective moth eye structures[2;3] and iridescent butterfly wings[6]. This has stimulated biomimetic research on obtaining such functionality by micro and nanofabrication methods. Optical effects that rely solely on surface topography has the potential for cost-efficient manufacturing in cheap polymers by embossing/imprinting or injection molding and can provide an alternative for chemical additives or multilayer deposition requiring vacuum methods.
This paper addresses structural color filters. Such devices have been proposed that are based on either sub-wavelength one dimensional gratings[84–87] or nano-holes in metal surfaces that rely on plasmon enhanced propagation[88;89]. These filters are all multi-material devices, and require several process steps to fabricate.
The results in this paper show that structural color filters can be produced in a single material, without use of pigments, dyes or multi-material sub wavelength structures. We demonstrate the application of strong scattering on random surface structures with dimensions close to the wavelength of the light. The structures show color effects in the direct transmission of white light, when fabricated in an otherwise fully transparent and colorless material and the textured surfaces thereby work as structural color filters fabricated in a single material. The optical performance of the demonstrated color filters rely on mechanisms different from those of periodic color filters[84–89], which in general have higher efficiencies and smaller spectral widths. On the other hand, the type of filter proposed here will benefit from a much lower fabrication cost.
The fabricated surfaces are characterized optically in transmission measurements and angle resolved scattering measurements. The measured results are compared to results calculated using diffraction theory and topographical information achieved by atomic force mi-

croscopy (AFM) and it is shown that for the investigated surface the specular transmittance can be predicted from an AFM-scan.
In recent years several methods for fabricating optically functional structures in polymeric materials have been investigated. For antireflective structures and structural color filters in polymers, the applications typically require large areas, making electron beam lithography inconvenient. Instead, methods like mask less plasma etching have been investigated which can fabricate randomly ordered nanostructures on large areas. The structures can be defined directly in the polymer surfaces e.g. by direct etching with a low pressure plasma[90] or by the use of an initial layer as random masking in a plasma etch[91].
Another approach is to fabricate the structures in a master and subsequently replicate them to the polymer. The replication process can be done by the use of an electroplated mold followed by hot embossing[21] or by casting a soft elastomeric mold from the master and subsequently use it for hot embossing or UV-nano imprint lithography (UV-NIL)[92;93].

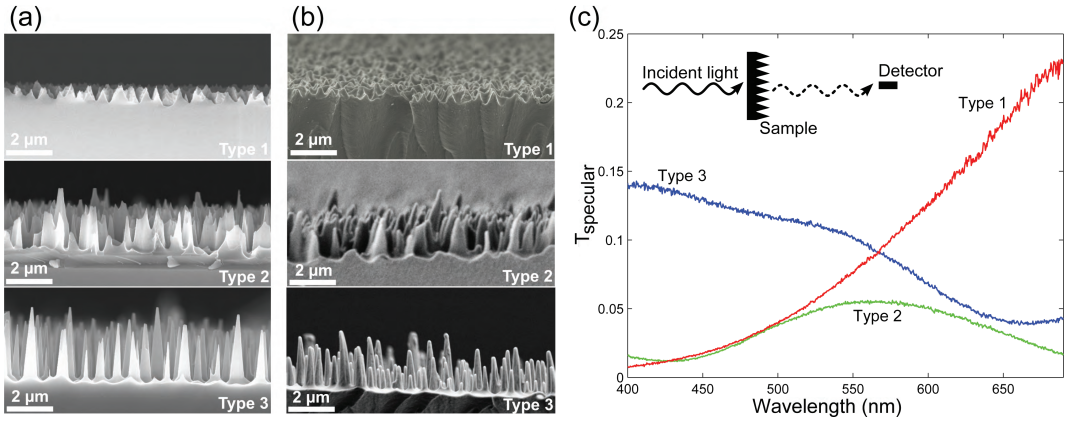

Figure 4.9: (a) Three different types of random surface structures fabricated in silicon by reactive ion etching. (b) The corresponding replica in Ormocomp fabricated in an UV-NIL process using a PDMS stamp casted from the silicon surface. The sharp corners of the silicon structures are rounded in the replication process. (c) Transmittance spectra of the three types of Ormocomp surface structures. The spectra are measured normal to the surface for normal incident light. The three types of surfaces appear orange, green, and blue respectively, when seen against a white light source.

Experimental section

The random structures were fabricated in silicon using reactive ion etching (RIE-STS Cluster System C004) with a gas mixture of SF_6 (15 sccm) and O_2 (22.5 sccm). The pressure was 300 mTorr, the platen power was 200 W, and the etching time was 10 minutes. The structures appear due to micro masking and the formation of a SiO_xF_y layer, which passivates the silicon surface. The resulting type of structure is determined by the rate of which the passivation is formed and subsequently removed by flourine radicals[63]. Three different types of structures were seen on one wafer. The variations are due to non-uniformities of the etch in the radial direction of the wafer. The three different types of structures are seen in Fig. 4.9(a). In the center of the wafer the structures are of type 1, at a distance of 10 mm from the edge the structures are of type 2, and 4 mm from the edge the structures are of type 3. All structures have lateral sizes similar to the wavelength of visible light and are therefore not characterized as sub-wavelength structures. As shall be demonstrated this results in scattering of incoming light, and the variations in height, shape, and pitch of the different types of structures lead to different scattering characteristics when replicated in

transparent materials.

The structures are replicated in the organic-inorganic hybrid polymer Ormocomp (Micro resist technology Gmbh, Berlin) based on the method described by Sainiemi *et al.* [93], where an elastomeric stamp is casted from the silicon and used in UV-NIL. The PDMS (Sylgard 184, Dow Corning) was mixed as recommended by the manufacturer and poured onto the master and left for degassing in a desiccator for 30 minutes prior to curing (65 degrees Celsius for 3 hours). The silicon master was coated with FDTS for anti adhesion.

Ormocomp was spin coated on a glass substrate to a thickness of approximately 50 μm. The imprints were performed in an Obducat NIL Imprinter 2.5 at room temperature with a hydrostatic pressure on the backside of the PDMS stamp (10 bar) for 10 minutes. The Ormocomp was cured with a UV-light source (1000 W for 10 minutes) through the glass substrate and the stamp was subsequently removed. The resulting replica of the silicon master are seen in Fig. 4.9(b). As expected from earlier reports the replicated structures are rounded [93;94], but the main characteristics of the various structures are maintained in the replica.

By using UV lithography the structures can be fabricated in specific patterned areas to make color filters of any macroscopic design. An example is seen in Fig. 4.10(a), where the pattern is seen as a black logo in the center of the silicon master. The structures in the logo are of type 1 and the corresponding replication is seen in Fig. 4.10(b). Here, the macroscopic logo is comprising wavelength scale structures not visible to the naked eye, yet causing the logo to appear orange when seen against the white light illumination.

All optical measurements were performed using a homebuild setup. The samples were illuminated at normal incidence with white light (Xenon lamp, HPX-2000). The light was collected in a fiber (500 μm in diameter) and analyzed in a spectrometer (Jaz, Ocean Optics). The setup made it possible to move the detecting fiber to any desired angle with respect to the sample.

AFM-images were scans of 20×20 μm^2 with a resolution of 512×512 pixels. The size of the scanned area influences the resolution of the scattering angle in the calculations [95] and is chosen such that good angular resolution is achieved while maintaining a sufficient spatial resolution in the AFM scan. The tip used was a high aspect ratio tip (Improved Super Cone type 125C40-R). Specifications according to the manufacturer: Tip height $>$ 7 μm, radius $<$ 10 nm, and full cone angle $<$ 10 degrees. The AFM used was a Metrology AFM based on a Dimension 3100 from Digital Instruments, Veeco Metrology Group (now Bruker) and a metrology head based on piezoelectric flexures equipped with capacitive distance sensors. All measurements were carried out in dynamic resonant mode.

Results and discussion

The structures have been characterized in the visible range from 400-700 nm. The specular transmission of light of the three types of structures is shown in Fig. 4.9(c). The quite different geometry of the three types also results in very different transmission spectra. The transmission spectrum of structures of type 1 shows much higher specular transmission for long wavelengths than for short wavelengths. The reason for this is wavelength dependent scattering which occurs at the structured surface, where light with short wavelength is scattered more than light with long wavelength. The opposite is the case for the transmission

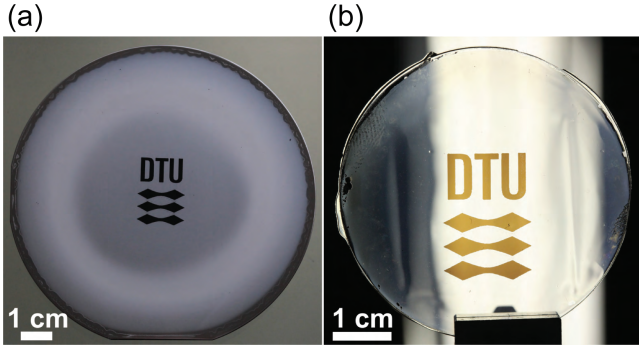

Figure 4.10: (a) Silicon master with a black DTU-logo fabricated by selective removal of the surface structures around the logo using photolithography and isotropic silicon etching. The structures in the logo are of type 1 (Fig. 4.9(a)). (b) Replication in an Ormocomp film on a glass substrate fabricated by UV-NIL with a PDMS stamp casted from the master. When seen against a white light source the logo appears orange.

spectrum of type 3, where red light is scattered more than blue light. For type 2 a peak in the transmission at 560 nm is observed. The three different transmission spectra illustrate the color appearance of the different areas of the imprint when seen against white light. Type 1 appears orange, type 2 appears green, and type 3 appears blue. In order to investigate the scattering behavior in more detail, measurements of the angle resolved scattering (ARS) were performed on another sample with similar scattering characteristics as type 1 in Fig. 4.9(c). Under normal incident light, the transmitted intensity was measured as a function of scattering angle θ as illustrated in Fig. 4.11(a). The transmission haze $H_T = T_{\text{diff}}/T_{\text{total}}$ is the probability that an incoming photon is diffusely scattered[95]. The specular transmitted light T_{specular} and the transmission haze are related as $T_{\text{specular}} = 1 - H_T$. In Fig. 4.11(b), the intensity normalized to the intensity of the incoming light is plotted as function of wavelength and scattering angle. In order to convert the data to a probability distribution, they are multiplied by a factor of $\sin\theta$ and for each wavelength the data are normalized such that 2π times the integral over θ equals the transmission haze[95]. The light is most probable to be diffracted to an angle around 30 degrees and the shorter wavelengths are most likely to be scattered. This explains the orange color of the specular transmitted light.

ARS must be intimately connected to the surface topography. The measured ARS has been compared to predictions based on measurement of the surface topography and diffraction theory. The surface topography was measured by AFM and a typical profile from an AFM scan is seen in Fig. 4.11(c). The model is based on non-paraxial scalar diffraction theory[96;97] and the used method is described in detail by Domine *et al.*[95].

While the overall qualitative agreement is seen by comparison of Fig. 4.11(b) and 4.11(d), the quantitative agreement can be evaluated in more detail in Fig. 4.11(e), where experimentally measured results and the results achieved from topographical information are compared directly for three different wavelengths. It is seen that the model predicts the scattering behavior of the surface structures very well.

It is also possible to make predictions for the specular transmittance using the surface topography as the only input. In Fig. 4.11(f) the calculated and measured values of the specular transmittance are plotted as function of wavelength for the investigated surface. While a deviation is seen for wavelengths shorter than 500 nm, the model fits the measured data

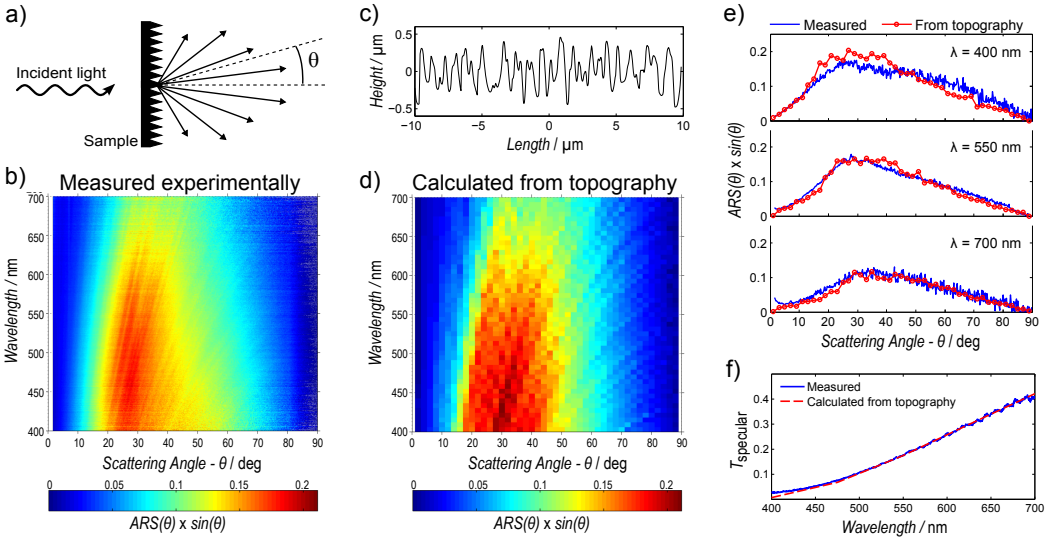

Figure 4.11: (a) Sketch of the measurement geometry for angle resolved measurements. The data are collected with normal incident light and the detector is moved to various angles measuring the intensity as function of θ. (b) Measured angular resolved scattering ARS(θ) for visible wavelengths. The data are multiplied by a factor of $\sin\theta$ to achieve a probability distribution. (c) Typical profile from two dimensional scan recorded by AFM used for the modeling. (d) ARS(θ) calculated from a 20×20 μm^2 scan of the surface topography. The data are normalized to all propagating modes and multiplied by $\sin\theta$. (e) Comparison of the experimentally measured data and the data calculated from the surface topography for three different wavelengths. (f) Comparison of the measured specular transmittance and the specular transmittance calculated from the measured surface topography.

very well in the rest of the considered interval and the color appearance can be predicted from the AFM image.

The quality of the measured AFM data has proven to be important for the achieved result. The tips used were specially designed for high aspect ratio surfaces in order to be able to resolve relevant features of the surface. The same analysis has been carried out using a standard AFM tip. The result of this analysis showed an increase in the specular transmittance over the entire wavelength interval of up to 0.1 compared to the measured data shown in Fig. 4.11(f).

Although the AFM measurements have proven adequate for the topographical characterization of the investigated surface, it would be less straight forward to characterize surfaces with structures of higher aspect ratio in detail. This is for example the case for the surfaces of type 2 and type 3 in Fig. 4.9(b) because the shape of the AFM tip would influence the observed topography more significantly. For prediction of the transmittance for surfaces with such high aspect ratios one may have to investigate other techniques or thoroughly approximate the tip shape and correct for the influence on the observed topography.

Conclusion

In conclusion, a route to the realization of cheap single material color filters has been demonstrated based on the concept of light scattering on surface structures. Three distinct colors have been observed for three different surfaces. The scattering characteristics could be reproduced from topographical data and the specular transmittance spectrum could be

predicted from a simple model which opens up new avenues for design of single-material plastic color filters.

Acknowledgements

The work was supported by the EC FP7 funded NaPANIL (Contract No. 214249) project and the NanoPlast project funded by the Danish National Advanced Technology Foundation (File No.: 007-2010-2). We thank professor Ole Sigmund for fruitful discussions, and acknowledge Emil Højlund-Nielsen and Thomas Buss for experimental assistance.

4.3 Paper II - Minimizing scattering from antireflective surfaces replicated from low-aspect-ratio black silicon

Authors

Alexander B. Christiansen[a], Jeppe S. Clausen[b], N. Asger Mortensen[b], and Anders Kristensen[a].
[a] Department of Micro and Nanotechnology, Technical University of Denmark, Oersteds Plads, Building 345B, DK-2800 Kgs. Lyngby, Denmark.
[b] Department of Photonics Engineering, Technical University of Denmark, Oersteds Plads, Building 343, DK-2800 Kgs. Lyngby, Denmark.

Abstract

The scattering properties of randomly structured antireflective black silicon polymer replica have been investigated. Using a two-step casting process, the structures can be replicated in Ormocomp on areas of up to 3 inches in diameter. Fourier analysis of scanning electron microscopy images of the structures shows that the scattering properties of the surfaces are related to the spatial periods of the nanostructures. Structures with a dominating spatial period of 160 nm, a height of 200 nm, and aspect ratio of 1.3, show insignificant scattering of light with wavelength above 500 nm and lower the reflectance by a factor of two.

Introduction

Antireflective nanostructures have the potential to provide an alternative to expensive coatings for optical components. High aspect ratio structures with periods around 200 nm have been shown to greatly reduce Fresnel reflections for a broad band of wavelengths.[20] Such periodic structures can be fabricated on large areas by laser interference lithography[25] or by anodized aluminium oxide.[23] An important feature of this kind of structure is that below a certain ratio between period and wavelength, only zeroth order diffraction will occur at the surface, and no light will be scattered.[26;98] Minimizing scattering is crucial when the antireflective element is to remain fully transparent and increase the direct transmission of light. Only recently have the scattering properties due to imperfections in periodic structures been studied.[30]

Another method for fabricating antireflective surfaces is by pattern transferral of the nanostructures in black silicon (BSi) surfaces. BSi structures are randomly positioned, cone-shaped formations, formed in silicon by a mask-less etching process.[65] However, due to the random nature of these structures, such surfaces will inherently scatter incoming light. Several studies have used this type of structures for antireflection[21;22;93] but the scattering properties of the surfaces have only recently been addressed.[77]

In this Letter we present a simple method for replicating BSi structures into Ormocomp, a transparent organic-inorganic hybrid polymer (Micro resist technology Gmbh, Berlin), on areas of up to 3 inches in diameter. The silicon masters were characterized by scanning electron microscopy (SEM) and dark field microscopy, and the Ormocomp replica were characterized by SEM and Fourier analysis, and light transmission measurements. The structures which showed increased transmission for light with a wavelength down to 500 nm were used to demonstrate the antireflective effect, which was significant even for structures with

aspect ratio as low as 1.3.

Fabrication

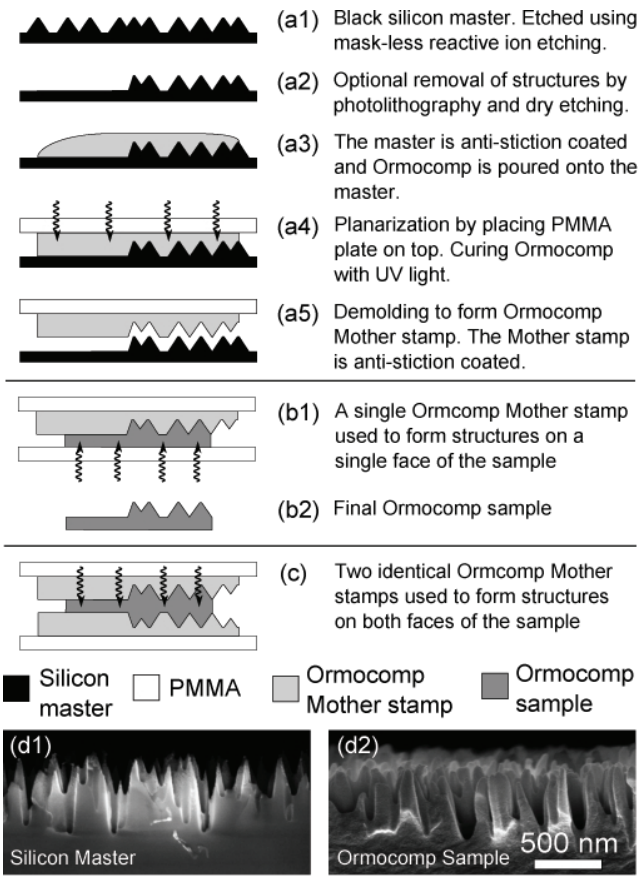

Figure 4.12: (a) Process for fabricating Ormocomp Mother stamps. A black silicon master is formed by mask-less reactive ion etching. Selected areas can be removed using conventional photolithography and dry etching. The master is anti-stiction coated and Ormocomp is poured onto the master. A PMMA plate is placed on top, planarizing the Ormocomp film. The Ormocomp is cured with UV light and the Mother stamp is released. (b) The final Ormocomp sample is formed from the Mother stamp similar to steps (a3-a4). (c) Using two identical Mother stamps, a sample can be formed with identical nanostructures on each face. (d1) Sideview SEM of a black silicon master. (d2) The final Ormocomp sample which was replicated from the Mother stamp.

The BSi substrates were structured by reactive ion etching (Pegasus DRIE, STS). The structures were formed in a single etching cycle with an O_2/SF_6-based etch.[65] By varying the gas-flows and platen power, different types of BSi surfaces were fabricated, denoted from hereon as types A-F.

After etching the BSi substrates [See Fig. 4.12(a1)], the surface can be patterned using conventional photolithography and dry etching to remove the nanostructures from the defined areas (a2). Using molecular vapor deposition, the BSi masters were coated with an anti-stiction layer. Ormocomp was poured on the master (a3) and a 1.5 mm thick and 4 inches wide polymethylmethacrylate (PMMA) substrate was placed on top. The thickness of the

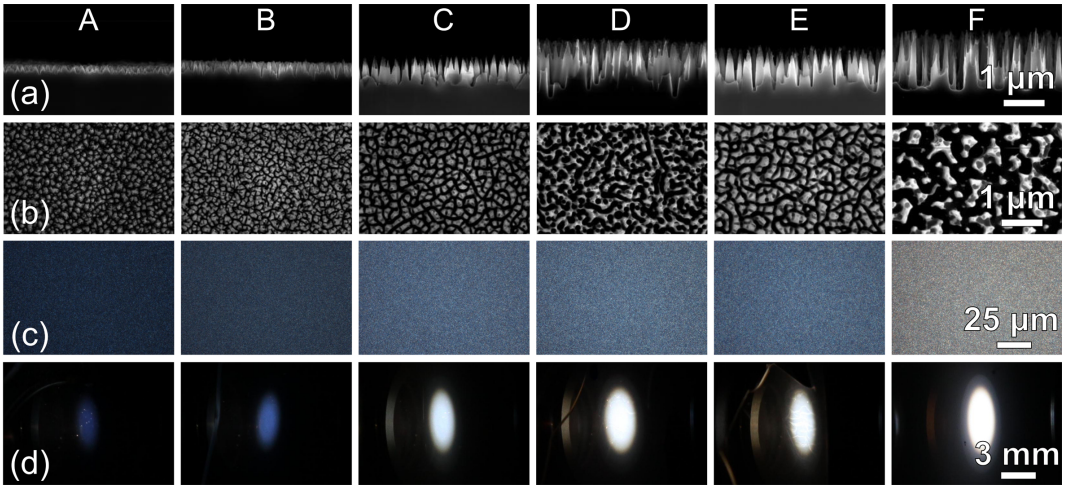

Figure 4.13: (a) Side view SEM of BSi. (b) Top view SEM image of BSi. (c) Dark field optical micrographs of BSi. (d) Photographs of fabricated Ormocomp samples. Samples were illuminated by a powerful white light source under normal incidence, and the scattered light was photographed at an oblique angle.

Ormocomp film was controlled by placing spacers at the periphery, between the master and PMMA back plate. The Ormocomp was cured with UV light in the wavelength range of 260-320 nm, through the PMMA (a4). The type of PMMA is Plexiglas XT 20070, which has a limited but sufficient transmittance in the 260-320 nm range. After UV exposure the flexibility of the Ormocomp and PMMA allowed for the gradual releasing of the Ormocomp film from the BSi master, while the Ormocomp remained attached to the PMMA (a5). Finally, the Ormocomp Mother stamp was coated with an anti-stiction layer.

Samples with structures on a single face were fabricated by pouring Ormocomp on the Mother stamp, and placing a PMMA backplate on top. The Ormocomp was again cured with UV light, through the PMMA, as shown in Fig. 4.12(b1) and (b2). Two identical Ormocomp Mother stamps were used to fabricate samples with identical antireflective structures on the front and back face, see Fig. 4.12(c). A comparison of the structures on a BSi master and the final Ormocomp sample is shown in Fig. 4.12(d1) and (d2).

Characterization and measurements

The silicon masters and the final Ormocomp samples were characterized by SEM top and side view micrographs. The relative scattering properties of the structures were characterized with a dark field optical microscope (Nikon Eclipse L200). The microscope was calibrated with a highly scattering sample (type F, see Fig. 4.13), and the exposure settings and white balance were fixed for all recorded images. Thus the relative scattering properties of the six types of surfaces can be characterized.

Power spectral densities of each Ormocomp sample were calculated from the top view SEM images by azimuthal averaging of the 2D Fourier spectrum of the surface.[66] This allows for identifying the dominating spatial frequency of the randomly ordered structures.

For the direct transmission measurements, the samples were illuminated at normal incidence with white light (Xenon lamp, HPX-2000, Ocean optics), through a fiber and a collimator.

The samples were aligned perpendicular to the incident light using a goniometer. The light was then collected in a fiber with a collimator, and analyzed in a spectrometer (Jaz, Ocean Optics). Thus only non-scattered, directly transmitted light was collected by the collimator.

Angle Resolved Scattering (ARS) measurements were performed using the same setup, by rotating the collecting fiber around the axis of the illuminated sample. The scattered transmitted light was collected at an angle (θ) from the normal, in the range 15° to 90°.

Figure 4.13(a) and 4.13(b) show SEM images of the BSi masters as viewed from the side and top, respectively. Fig. 4.13(c) shows dark field microscope images of the BSi masters. Fig. 4.13(d) shows photographs of the fabricated Ormocomp samples, when illuminated by an intense white light source (Xenon lamp). The samples were illuminated at normal incidence and photographed from an oblique angle. The results shown in Fig. 4.13(c) and (d) offer a simple comparison of the relative scattering properties of the different BSi masters and the final Ormocomp samples respectively.

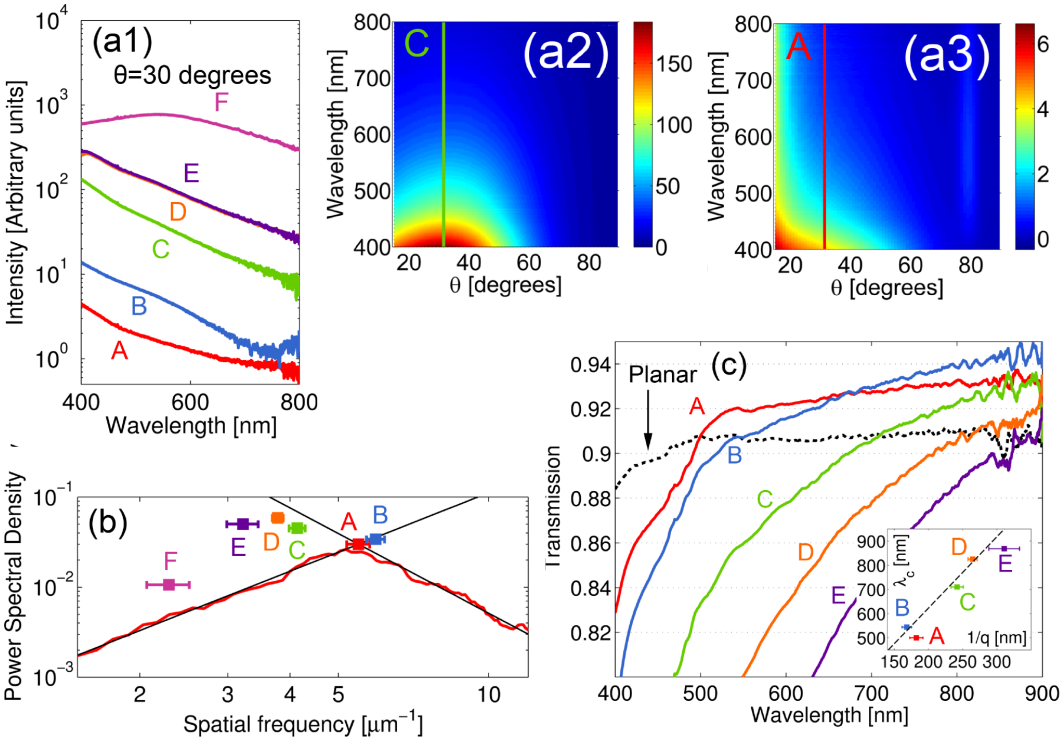

Figure 4.14: (a1) Intensity of transmitted, scattered light, measured at an angle of $\theta = 30°$, for the six different Ormocomp samples. (a2) and (a3) Surface plots of the full ARS measurements of samples C and A respectively. (b) Power spectral density of type A Ormocomp sample. The square marked A is the dominating spatial frequency, q, found by fitting, with a 95% confidence interval. Squares marked B-F indicate q for other types of surfaces. (c) Direct transmission measurements of Ormocomp samples with antireflective structures on one face. Insert: Wavelength at intersection between transmission spectra of planar and structured surfaces, λ_c, as a function of the dominating structural periods, q^{-1}.

Figure 4.14(a1) shows the intensity of transmitted, scattered light, measured at an angle of $\theta = 30°$, for the six different Ormocomp samples. The intensity of the scattered light varies within two orders of magnitude when comparing the different samples. The results

show that for all samples, the shorter wavelengths are scattered significantly stronger than the longer wavelengths. Fig. 4.14(a2) and (a3) show surface plots of the full ARS measurements of samples C and A respectively.

Results and discussion

Figure 4.14(b) shows the power spectral density of a top view SEM image of a type A Ormocomp sample. The black lines show a fit to a power function of the first and last parts of the data. The intersection of the two lines thus marks the dominating spatial frequency, q, of the surface structures, and the error bars represent a 95% confidence interval on q, based on the uncertainties of the parameters of the two fitted functions. Power spectra for the other Ormocomp samples were analyzed in a similar manner, and the intersections are denoted by squares.

Figure 4.14(c) shows direct transmission measurements of planar and structured Ormocomp samples. For clarity, sample F is not shown as the transmission is below 0.5 throughout the spectrum. Most samples show antireflective properties at a wavelength of 900 nm, while only sample A and B show increased transmission down to 500 nm and 550 nm, respectively. Samples C, D, and E show reduced transmission in the entire visible spectrum due to scattering. It is evident that the structures of type A, with aspect ratio of 1.3 and height of 200 nm, reduce the reflectance by a factor of 2, from 4% and down to 2% in the visible spectrum.

The insert in Fig. 4.14(c) shows the wavelength of the intersection of each transmission line with the planar line, denoted λ_c, as a function of the dominating structural periods, q^{-1}, found in Fig. 4.14(b). The plot thus correlates the spatial frequency of the surface structures to the scattering properties. This central result shows that larger values of q lower the cut-off wavelength, λ_c, at which scattering becomes significant. This shows that replica of BSi structures are viable for increasing transmission of light in the visible spectrum, despite the random nature on the structures. Furthermore, the scattering properties can be estimated simply from a top view SEM image.

Finally, the type A structures were used to fabricate a sample with nanostructures on both faces, see Fig. 4.12(c). The resulting sample is shown in Fig. 4.15(a), where the transparent Ormocomp disc is placed on a sheet of paper with a printed logo. On the left side, the light from a lamp is reflected specularly from the planar top and bottom surface of the sample. On the right side, nanostructures covering both the top and the bottom faces, suppress part of the Fresnel reflections, rendering the underlying surface visible. We note that the scattered blue light is too dim to see in daylight conditions.

Conclusion

In conclusion we have shown that the spatial frequencies of BSi structures are related to the scattering properties of the antireflective surfaces. Structures with a dominating spatial frequency of 160 nm, a height of 200 nm, and aspect ratio of 1.3, show insignificant scattering of light with wavelengths above 500 nm and reduce Fresnel reflections by up to a factor of 2. Using a simple two-step casting process, the structures can be fabricated in Ormocomp

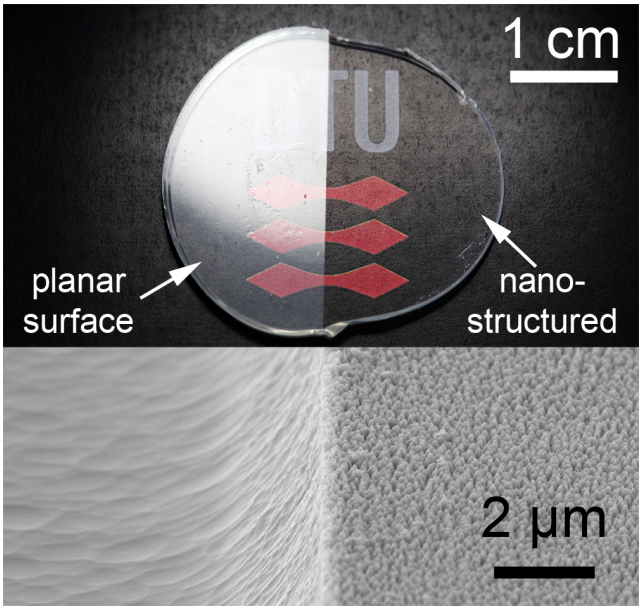

Figure 4.15: (a) Photograph of Ormocomp sample with antireflective nanostructures on top and bottom face, placed on a sheet of paper with a printed logo. Nanostructures are on the right side of the fully transparent sample. (b) SEM image of the sample, showing the difference between the planar (left) and the nanostructured surface (right).

on areas of up to 3 inches in diameter.

Acknowledgements

We thank Ole Sigmund, Johannes Weirich and Jakob Birkedal Wagner for fruitful discussions. The work was supported by the NanoPlast project funded by the Danish National Advanced Technology Foundation (File No.: 007-2010-2).

4.4 Paper III - Imprinted and injection-molded nano-structured optical surfaces

Authors

Alexander B. Christiansen[a], Emil Højlund-Nielsen[a], Jeppe Clausen[b], Gideon P. Caringal[a],N. Asger Mortensen[b], and Anders Kristensen[a].
[a]Department of Micro and Nanotechnology, Technical University of Denmark, Oersteds Plads, Building 345B, DK-2800 Kgs. Lyngby, Denmark.
[b]Department of Photonics Engineering, Technical University of Denmark, Oersteds Plads, Building 343, DK-2800 Kgs. Lyngby, Denmark.

Abstract

Inspired by nature, nano-textured surfaces have attracted much attention as a method to realize optical surface functionality. The moth-eye antireflective structure and the structural colors of Morpho butterflies are well-known examples used for inspiration for such biomimetic research. In this paper, nanostructured polymer surfaces suitable for up-scalable polymer replication methods, such as imprinting/embossing and injection-molding, are discussed. The limiting case of injection-moulding compatible designs is investigated. Anti-reflective polymer surfaces are realized by replication of Black Silicon (BSi) random nanostructure surfaces. The optical transmission at normal incidence is measured for wavelengths from 400 nm to 900 nm. For samples with optimized nanostructures, the reflectance is reduced by 50 % compared to samples with planar surfaces. The specular and diffusive reflection of light from polymer surfaces and their implication for creating structural colors is discussed. In the case of injection-moulding compatible designs, the maximum reflection of nano-scale textured surfaces cannot exceed the Fresnel reflection of a corresponding flat polymer surface, which is approx. 4 % for normal incidence. Diffraction gratings provide strong color reflection defined by the diffraction orders. However, the appearance varies strongly with viewing angles. Three different methods to address the strong angular-dependence of diffraction grating based structural color are discussed.

Introduction

Within the past decades, nano-textured surfaces have attracted much attention as a method to realize optical surface functionality. The moth-eye antireflective structure[2] and the structural colors of Morpho butterflies[99;100] are well-known examples. In this paper, nanostructured polymer surfaces suitable for up-scalable polymer replication methods, such as imprinting/embossing and injection-molding, are discussed. The limiting case of injection-moulding compatible designs is investigated.
This study is motivated by the need for efficient and large scale recycling, due to an increasing world population and declining natural resources. Much of the waste generated stems from plastic products. Here the base color is given by bulk properties based on pigmentation. Added surface decoration provides additional color effects, for example logos, text decoration or line art, thereby providing cost effective color effects. However, the addition of decoration also makes recycling difficult, because the powerful pigments used for the thin decoration layers tend to pollute the base color of the bulk material in the recycling state. Here we propose functional surfaces for structural colors and other optical effects to produce decoration art, thereby enabling a direct decomposition into raw materials of the consumed

product. The vision is multi-functional surfaces, where surface topography added to a material creates new functionalities, such as color, anti-reflective and self-cleaning properties for plastic parts.
The nano-texture anti-reflective surface of moth-eyes was first reported in 1967 by Bernhard[2], who observed the tapered nano-structure by scanning electron microscopy of slices of the moth-eye lens. The broadband anti-reflective functionality was confirmed by microwave experiments. In 1973, Clapham realized the first artificial anti-reflective moth-eye structure in the visible range by interference lithography in a thin photo resist film on a glass substrate, yielding 200 nm protuberances[3]. Already these first papers clarified the underlying physics; that the structures function as an effective gradient in refractive index of the material reducing reflections from the surface. Furthermore, it was shown by modelling that minimum reflectance can be achieved with $d/\lambda = 0.4$, where d is the height of the tapered protuberances and λ is the vacuum wavelength for glass materials. More general numerical modelling was reported by Stephens and Cody in 1977[101]. The advancement of nano-scale lithography has enabled further research; a few examples are electron beam lithography defined silicon nanocone arrays[102], silicon and polymer surfaces by plasma etching and replication[93] and anti-reflection anti-fogging silica surfaces[25].
Structural colors are optical phenomena, where the topography of a surface determines the reflected spectrum of light, although an unambiguous definition has not been settled yet[6]. In recent years, structural coloration has attracted considerable attention within the field of optics[7–10]. The mechanisms of structural colors are categorized into thin-film interference, multi-layer interference, diffraction grating optical effects, and photonic crystal effects.[6] In nature, structural colors are found among butterflies and beetles, such as the Morpho butterfly[5], reflecting omnidirectional blue light due to a multilayer topography.
The structures found in nature often consist of several layers. Here the focus is on one-layer structures that comply with injection-molding, the industry standard for high volume plastic production. This only allows for simple single-material surface textures, and may not, for example, comprise closed air-filled regions inside the material.
Anti-reflective polymer surfaces are realized by replication of Black Silicon (BSi) random nanostructure surfaces. The specular and diffusive reflection of light from polymer surfaces and their implication for creating structural colors is discussed. In the case of injection-moulding compatible designs, the maximum reflection of nano-scale textured surfaces is discussed. Diffraction gratings provide strong color reflection defined by the diffraction orders. However, the appearance varies strongly with viewing angles. Three different methods to address the strong angular-dependence of diffraction grating based structural color are discussed.

Reflection from a polymer surface

In this section, the specular and diffusive reflection of light from polymer surfaces and their implication for creating structural colors is discussed. The limitations imposed by the injection moulding production platform itself is considered. Injection-moulding requires that the parts are able to be separated from the molding tool without damage. Therefore, any topography must consist of one layer only of alteration without closed air-filled regions inside the material. Any structure may only consist of one layer of alteration on top of bulk. All individual structures or combinations may be periodic or semi-periodic. We will refer to these single-material structures of one layer, that have zero or positively sloped side walls, as injection-moulding compatible surface textures, because they in general allow for the separation in an injection-molding machine. Examples are given in Fig. 4.16.
The topography limitations described above generally indicate that the advanced multi-layer

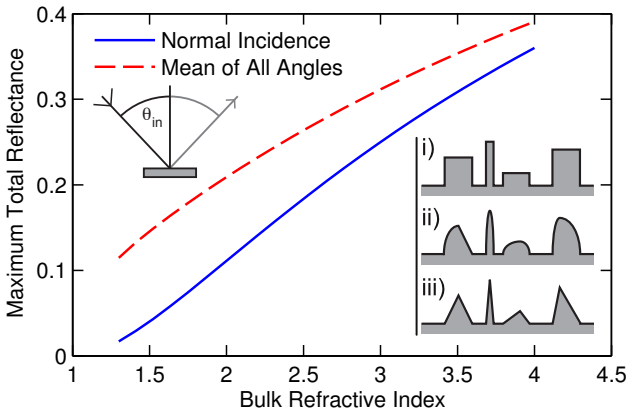

Figure 4.16: Maximum specular reflectance for Injection-molding compatible topographies for unpolarized light for normal incidence (blue curve) and averaged over all incoming angles assuming a uniform intensity distribution (red curve), where examples i, ii and iii are defined with respect to an initial flat micro-scale surface.

structures often found in nature, on butterfly scales and similar[103], cannot be fabricated using a one-step injection molding process. These limitations have consequences for the optical performance. It has been shown by Bao[104] that the upper limit of surface reflection for all injection-molding compatible periodic structures are given by the reflectance of a plane dielectric interface, where the largest difference in refractive index occurs and thus the largest reflection of energy. The reflection of a planar dielectric interface is also known as Fresnel or specular reflection, often arising from mirror like surfaces. This limitation applies for all values of the bulk refractive index, n_2, larger than that of the surrounding air medium, n_1. The simplest possible case of reflection and transmission is given by of a lossless dielectric interface between two regions, air and material. The reflection and transmission for normal incidence is independent on polarization and can be calculated using the Fresnel coefficients:

$$R_{\perp} = r^2 = \left(\frac{n_1 - n_2}{n_1 + n_2}\right)^2 = \left(\frac{1 - 1.5}{1 + 1.5}\right)^2 = 0.04,$$

indicating that plastic materials only reflect 4 % of the incoming normal light. The remaining 96 % is transmitted into bulk. It is seen that, as the numerical difference between the two refractive indices becomes smaller, the reflection is reduced. We define the hemispherical reflection W for un-polarized light averaged over all angles: $W(n_1,n_2) = \frac{1}{\pi}\int_{\theta_{in}=-\frac{\pi}{2}}^{\frac{\pi}{2}} R(n_1,n_2,\theta_{in})\,\mathrm{d}\theta_{in}$, describing the total normalized reflection of a dielectric surface equally illuminated at all angles. In Fig. 4.16, the total reflection is seen as function of refractive index for normal incidence and averaged over all incoming angles (hemispherical reflection). For an air-plastic interface, with $n_2 = 1.5$, we find an accumulated reflection of 8.92 % for p-polarization and 20.2 % for s-polarization. This means, that in normal daylight, meaning uni-directional unpolarized light, we may only alter 14.6 % of the incoming light at maximum. The remaining 85.4 % of the incoming light is transmitted into bulk, where it may be absorbed or scattered. As an rule of thumb, the hemispherical reflection for common plastic materials is around 15 %. These numbers describe the fundamental limit of performance in clear plastic for any structure or design respecting the injection-molding compatibility condition. In general, higher refractive index means higher reflection.

We now consider a periodic nano-texturing of the surface, characterized by a period Λ. If the period of the texture is longer than the wavelength of the incident light, we refer to this

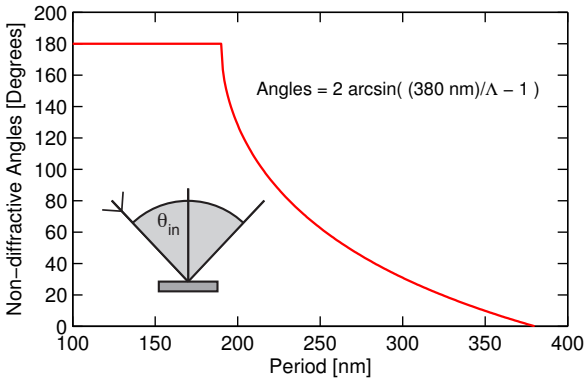

Figure 4.17: Incident angles causing no reflected diffraction in the visual spectrum as function of nanostructure period. Periods below 190 nm does not lead to diffraction at any angles in the visual spectrum.

periodic alteration as a diffraction grating. We find the grating equation[50] Eq. (1), here written in the most general case:

$$n_1 \sin\theta_m - n_1 \sin\theta_{\text{in}} = \frac{m\lambda}{\Lambda}, \ (\text{reflected orders}) \qquad (4.4.1)$$
$$n_2 \sin\theta_m - n_1 \sin\theta_{\text{in}} = \frac{m\lambda}{\Lambda}, \ (\text{transmitted orders})$$

where n_1 and n_2 is the refractive indices of the incident medium and the transmission medium respectively, and θ_{in} is the incident angle of the light with respect to the surface normal. This is a very general formula because Fourier series form the most fundamental solution to any linear differential equation that is subject to periodic boundary conditions. Therefore iridescence arising from diffraction gratings always takes the form of one or more ordered spectra although intensity may vary. Besides the slowly varying intensity of diffracted spectral orders described by the grating equation (4.4.1), rapid variations can also be found in certain narrow frequency bands. These abnormally high or low intensities in the diffracted light are referred to as Wood's anomalies[105]. Especially in the case of the first diffraction order appearing parallel to the surface at glancing angle, anomalies in the measured spectra can be found. According to Stewart and Gallaway[105], the corresponding "Rayleigh" wavelengths can be found in the zero–order specular radiation yielding:

$$\lambda_R(\theta_{\text{in}}) = \frac{\Lambda}{m_\pm}(\pm 1 - \sin\theta_{\text{in}}). \qquad (4.4.2)$$

At the Rayleigh wavelengths first order emerges at glancing angle and the redistribution of energy results in a anomaly in the specular reflection. Anomalies have been subject to an intense study. Hessel and Oliner[106] argue that two distinct types of anomalies may exist: A Rayleigh wavelength type due to the emergence of a new spectral order at grazing angle, and a resonance type which is related to the guided complex waves supportable by the grating.

To complete the picture of optical gratings, we also discuss, sub-wavelength, non-diffractive gratings using an argument given by Raguin and Morris[50]. For non-diffractive gratings the period should be small enough that all higher diffraction orders are evanescent. From the grating equation, this requirement sets an upper limit to the period-to-wavelength ratio specified by[50] Eq. (2); $\frac{\Lambda}{\lambda} < \frac{1}{\max(n_2,n_1)+n_1\sin\theta_{\max}}$, where $\theta_{\max}$ is the maximum angle of incidence.

Since the denominator of the right-hand side of the above inequality is always larger than unity because $n_1 \geq 1$ and $n_2 \geq 1$, it is seen that the surface must always have a surface period smaller than the dimensions of the incident wavelength, hence the term sub-wavelength. It should be noted that the above argument is normally only given in terms of the reflected orders, leading to an intermediate range of structures that are often anti-reflective, but still scatters light in the transmission. In the case of a period of 250 nm, the first order reflection appears at glazing angle (horizontal along the interface) at 31 degrees incidence, meaning that the perceived specular color is significantly changed for angles bigger than 31 degrees incidence. Therefore, the non-diffractive angle interval is 62 degrees, as seen in Fig. 4.17. For a period of 200 nm, first order reflection does not occur until 76 degrees. Periodic structures below 250 nm provides basis for angle-independent colors, although diffractions can be seen for angles approaching grazing angle. For structural color effects, the optimum is periods approximately 200 nm in order to avoid diffraction in the visual spectrum. Periods below 190 nm do not lead to diffraction at any angles in the visual spectrum, as seen in Fig. 4.17, however transmission diffraction effects may still affect the specular reflection.

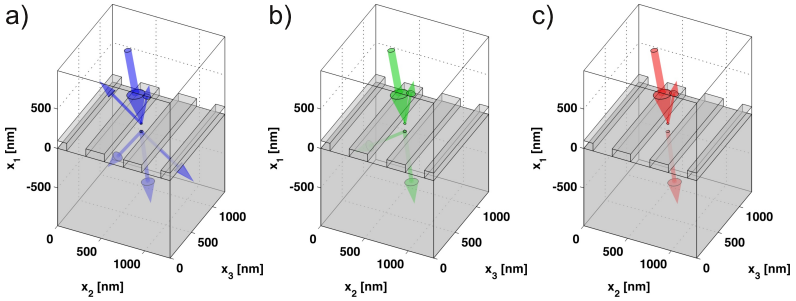

Figure 4.18: RCWA simulations illustrating the three fundamental grating regimes using 430 nm period, 100 nm height, 10° incident light and $n_2 = 1.4$. Arrows indicate magnitude on logarithmic scale. a) λ = 410 m (blue light). Several orders in both transmission and reflection. b) λ = 550 nm (green light). 0'th order in reflection, two orders in transmission. c) λ = 680 nm (red light). Only 0'th order in both reflection and transmission.

As illustrated in Fig. 4.18 three optical regimes can be distinguished: 1) For short wavelengths, several orders in both the transmission and reflection exist, 2) for wavelengths longer than the period, only the zero–order in reflection but still several orders in transmission exist, and finally, 3) for long wavelengths only zero–order in both reflection and transmission exist. These three optical regimes are fundamental to the reflection and transmission of optical gratings.

Antireflective structures

Anti-reflective coatings, as widely applied in many optical components, is conventionally realized by adding one or more layers of dielectric or metallic thin films on the surface. It is widely known that a single layer can reduce the reflectance of a glass surface to a mean value of approximately 2.5% in the visible spectrum. Multi-layer coatings, typically with 3-6 layers can reduce the reflectance to below 0.5% in the visible spectrum. At 45° incident angle the reflectance of such a coating is approximately 1%.
Antireflective properties can also be obtained by structuring the surface on the nanoscale. In the sub-wavelength regime, light cannot resolve the individual features of the surface. The structures function as a gradient in the effective refractive index of the material, reducing Fresnel reflections from the surface[2;3]. Antireflective structures can be realized in different ways. It can be random structures or periodic structures in one or more dimensions. For

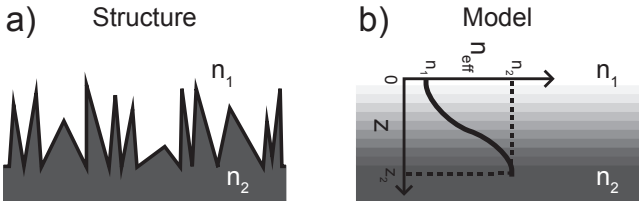

Figure 4.19: Illustration of sub-wavelength structures to reduce Fresnel reflection. a) Structure. b) Modeling by a gradient in the effective refractive index of the material.

fabrication of such such nano-texture by casting or molding, the master structures can be fabricated in a range of different ways. Random textures have been fabricated by anodized aluminium oxide[23] and by so-called black silicon[78;93], whereas periodic textures have been realized by interference lithography[3] and electron-beam lithography[102].
In 2008 Ting *et al.* reported antireflective structures in PMMA, fabricated by hot embossing with a Ni-Co stamp[21]. The high aspect ratio structures were fabricated in Si using electron cyclon resonance (ECR) etching, and the Ni-Co shim was subsequently electroplated from the Si master. They report reflectances below 0.5% in the visible spectrum for structures with aspect ratio higher than 2.6. In 2010 Hong *et al.* reported the fabrication of antireflective nanostructures in COC by hot embossing from a black silicon master. After hot embossing, the master was dissolved as it was not possible to release it from the imprinted COC. the transmittance of COC was increased from 90% to 95% by nanostructuring both sides of the COC film. The aspect ratio of the structures was up to 12, and the tip of the structures was below 20 nm. Jang *et al.* reported laser interference patterns in Si hot embossed in polycarbonate. Transmittance increased from 90% to 93.5% (single side)[26] and drops in transmittance are observed when diffraction occurs for small wavelengths. For example, a grating with a period of 227 nm has a cut-off wavelength around 375 nm, whereas a 300 nm period yields a cut-off wavelength of approximately 475 nm.

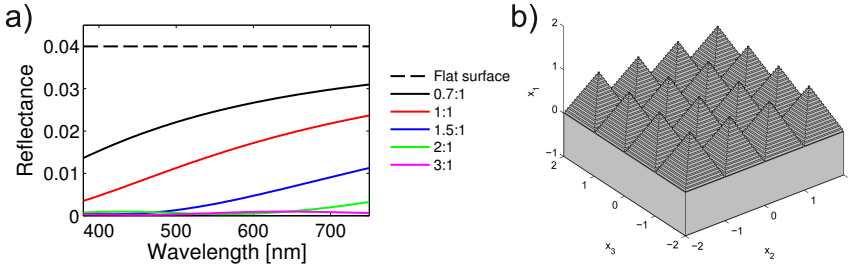

Figure 4.20: Reflectance of pyramid texture as function of wavelength for various aspect ratios. a) Calculation by 100 layers with transfer matrix approach and effective medium theory. b) Schematic of modelled structure.

The black silicon method[63] has been chosen for this study. This is a cheap and fast method to cover large areas with random conical-shape nanostructures. For comparison, the price-per-area for e-beam exposed masters can be four orders of magnitude higher. Black silicon etching is a mask less reactive ion etching (RIE) process, which can form large areas of random tapered nanostructures. Black silicon etches can be performed in many different ways. The simplest one uses just SF_6 and O_2[65]. SF_6 supplies the fluorine atoms that react with silicon to make a volatile SiF_4 gas. The oxygen reacts with fluorine and silicon to make a passivating layer of $Si_xF_yO_z$. Any protrusion that will exist or is formed on the surface will be slightly more protected by the passivation layer compared to the planar regions of the surface. As the etching continues, any roughness will be enhanced and eventually form

cone or needle-like structures. The surfaces formed by this method are statistical in nature due to the random formation process. Thus it is not a lithography method. However, by controlling the critical etching parameters[93] such as pressure, platen power, gas flows and temperature, the average lateral sizes and aspect ratios of the structures can be tuned. The black silicon can then be used as a master, for replication in polymer by hot embossing or by UV nano-imprint lithography (UV-NIL).
The antireflective effect can be described by dividing the structured region of the surface in thin layers of increasing refractive index. Instead of a single interface, the surface now consist of a multiple of interfaces, each with a small increment in the refractive index, see Fig. 4.19. Due to the non-linear dependence on the refractive index of the Fresnel coefficients, the total reflectance from such a system will be smaller than that of a single interface. From this model, the reflectance of a polymer surface can be calculated, using the transfer matrix method[48]. The refractive index of each of the layers can be described from the geometry of the structures, and an effective medium theory. The result of such a model is given in Fig. 4.20, for a surface with pyramid shaped structures. It is seen that by increasing the height of the structures, the reflectance can effectively be reduced to zero. However, large-aspect-ratio structures can be challenging to fabricate. Thus, significant anti-reflective effect is seen for structures with an aspect ratio of only 1.5:1.
The random nanostructures will inherently scatter light. This is a drawback for our applications. If the structures are too large, they will scatter light in the visible spectrum, rendering the surface of an otherwise clear polymer milky white. As shown by the authors[77], the scattering properties of black silicon can be tailored to function as color filters in directly transmitted light. Furthermore, the scattering from the randomly textured black silicon can be minimized, as reported by the authors[78]. By controlling the black silicon etching process, the characteristic lateral spatial frequency of the nanostructures can be maximized to minimize scattering. An example of such a surface is shown in Fig. 4.21. The sample is fabricated using black silicon as a master for a UV-NIL process, using the UV curable resin, Ormocomp (a transparent organic-inorganic hybrid polymer from Micro resist technology Gmbh, Berlin). The left side of the sample is a planar Ormocomp surface on both front and backside, whereas the right side is nanostructured on both front and back. The sample is placed on a paper with a DTU logo printed on a black background and illuminated by a white light source for specular reflection into the camera. It is clearly seen that the nanostructured surface suppress a large part of the specularly reflected light. The nanostructures reduce Fresnel reflection by 50%, even though they only have an aspect ratio of 1.3. The structures are 200 nm tall, and have a characteristic distance between each nanostructure of 160 nm corresponding to a lateral spatial frequency of 6 μm^{-1}.

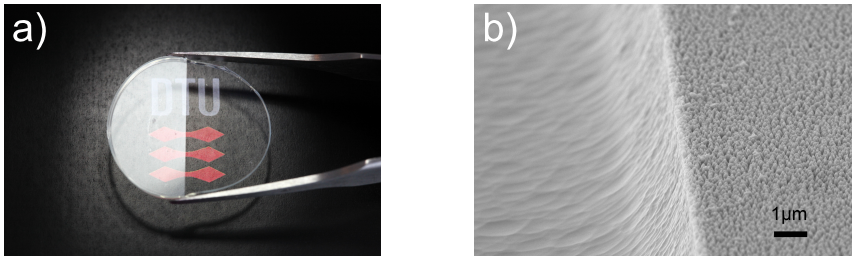

Figure 4.21: Comparison between functionality and nano-texture. a) Photograph of an Ormocomp sample with antireflective functionality of the nanostructures fabricated by UV-NIL, using black silicon as a master (right part of sample), compared to a non-textured surface (left part of sample). b) SEM image of the interface between the nano-textured and non-textured surface.

Angle-independent structural colors

Structural colors can originate from nano-textured surfaces. As a first approach to address the strong angular-dependence of diffraction grating based structural color, we discuss the possibilities of structural color in the case of polymer surfaces from sub-wavelength diffraction gratings. The grating scattering properties are studied by RCWA,[107] using a commercial solver (GD-Calc, KJ Innovation) for simulating the absolute values of reflection and transmission. Due to the dependence on the exact structural dimensions, each point in the $(\theta_{\text{in}}, \phi_{\text{in}}, \lambda)$ parameter space must be individually assessed for given structural dimensions.

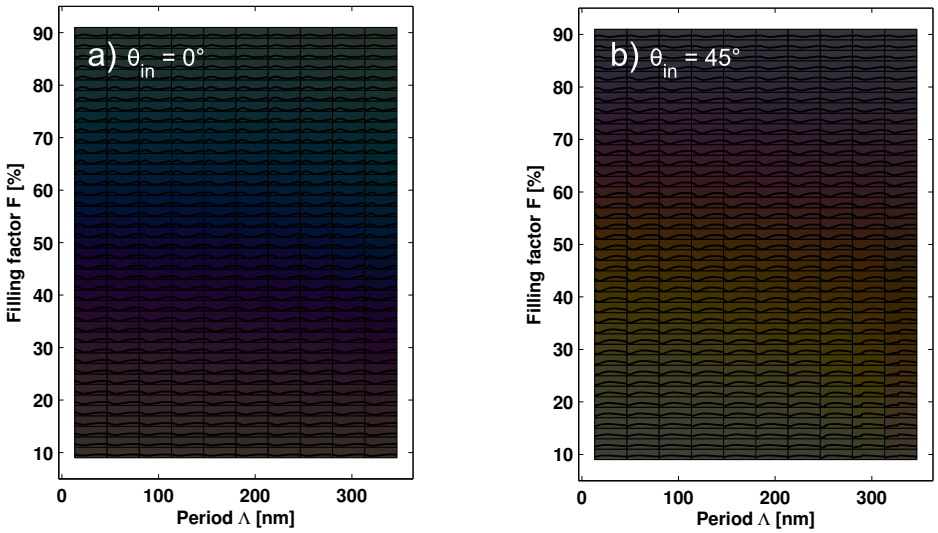

Figure 4.22: Example of plastic (n=1.5) surface daylight color effects based on a square lattice. a) Normal incidence. b) 45° incidence. Each square shows RCWA simulated specular colors for given parameters.

For background, the color of an object is the result of a complex interaction between the light source $S(\lambda)$ incident on the object, the reflection or transmission of the object $R(\lambda)$ or $T(\lambda)$, and the observer modeling the spectral sensitivity of human perception. In the CIE 1931 XYZ-model,[108] colors can be defined on integral form:

$$\begin{bmatrix} X \\ Y \\ Z \end{bmatrix} \equiv C^{-1} \int_0^{\infty} S(\lambda) R(\lambda) \begin{bmatrix} \bar{x}_{\text{obs}}(\lambda) \\ \bar{y}_{\text{obs}}(\lambda) \\ \bar{z}_{\text{obs}}(\lambda) \end{bmatrix} \mathrm{d}\lambda, \tag{4.4.3}$$

with normalization $C \equiv \int_0^{\infty} S(\lambda)\, \bar{y}_{\text{obs}}(\lambda)\, \mathrm{d}\lambda$. The parameters $(\bar{x}_{\text{obs}}, \bar{y}_{obs}, \bar{z}_{obs})$ describe the spectral sensitivity of the observer and roughly correspond to the sensitivity of the three cones (fovea centralis) of the human eye. Here, we use the 1978 Judd Vos correction[109] of the CIE 1931 2° observer[108] and the ISO/CIE standard illuminant D65.[110] In order to accurately present color values, a conversion between the device-independent CIE-XYZ model and device-dependent outputs on a display (voltages expressed in RGB) or paper (CMYK) is needed. Here we adopt the sRGB conversion for display.[111]
Given the fabrication platform developed, what possible colors may be produced? An answer to that question is given by the color map in Fig. 4.22 for normal incidence and 45° incidence. The map is constructed by simulating the reflection of squared two-dimensional silicon gratings converted into a color via Eq. (4.4.3). The colors may appear darker due to the overlaying reflection spectra data.

From the figures, it is seems that bright angle in-dependent color effects in polymer material by sub-wavelength diffraction gratings are challenging. The results confirm the basic observation that the total reflectance cannot exceed the Fresnel reflection of the corresponding planar surface.

Angle-dependent color effects by diffraction grating pixels

Even though the reflectance of polymers is low, diffraction gratings can provide bright reflected angular dependent color effects on a black polymer substrate by diffracting light into several beams traveling in different directions. Despite the angular-dependent nature of diffraction, it is possible to obtain what we will refer to as an pseudo-angular independent color effect. This can be achieved by combining multiple gratings of different types in a pixel-array. Each pixel, consisting of a single grating, will be highly angle-dependent, however the overall glitter effect of the entire array will appear homogeneous and independent of viewing angle as a second approach to address angle-dependence.

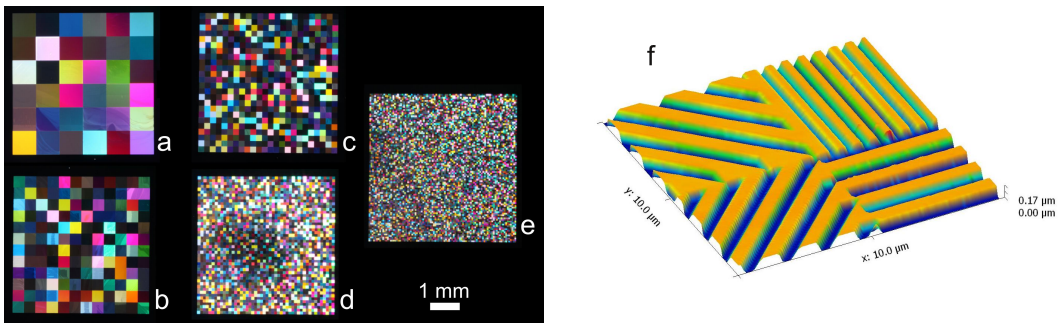

Figure 4.23: Photographs of the pixel grating structures on black PMMA. a) Shows the array with the biggest pixels, 800 micron. b) 400 micron. c) 200 micron. d) 100 micron. e) Down to 50 micron, barely resolvable with the human eye. f) AFM image of the Si master, showing an intersection between four different pixels. The different orientations and periods of the diffraction gratings give rise to the pseudo angle-independent color effect.

The individual gratings are chosen to be one-dimensional line gratings. A 2D-grating would provide more diffraction orders, thereby increasing the chance of an order being seen by the observer, but the individual orders would also be significantly weaker. By choosing 1D gratings there will be fewer orders, but the ones existing will be much stronger. The period of a grating determines the direction of the diffraction orders for light with a given incident angle. Here we use 8 different periods ranging from 700 nm to 1400 nm with 100 nm spacing in a uni-form distribution. This interval is chosen to provide orders for large intervals of solid angles, while still maintaining bright individual orders. To even out the azimuthal angle dependence, the gratings are oriented in four different directions. The height and filling factor are chosen to maximize the diffraction efficiency for a wide range of wavelengths and incident angles. Based on RCWA simulations, it is found that a height of 135 nm and a filling factor of 50 % leads to a optimum of diffraction efficiency, with respect to incident angle and wavelength.
The diffraction gratings were defined using electron beam lithography on a silicon wafer. The structures were transferred to a black PMMA substrate, using hot embossing. An AFM image of the fabricated master is shown in Fig. 4.23f, where four different pixels can be seen. The fabricated PMMA sample was photographed using a digital single-lens reflex camera with a Canon MP-E 65mm f/2.8 1-5x Macro lens, and a white light source. The photographs, seen in Fig. 4.23, were taken directly above the sample, with the light source

directed at the sample from the side. The lens can resolve features not visible to the human eye. The 50 micron pixels, for example, are easily seen in the photo with the help of the lens. Each array is 4.8×4.8 mm^2, (a) is the 800 micron pixels, (b) 400 micron; halved each time, down to (e) with 50 microns.

Diffraction gratings on thick transparent foils

Until this point the nano-textured polymer surface has been considered as an isolated system with the reflectance of the surface being the only contribution to the observed color. This is for example the case for a black pigmented polymer, where practically all light entering the polymer is absorbed. As a third approach to overcome angular dependence, we now discuss the inclusion of backside reflections.

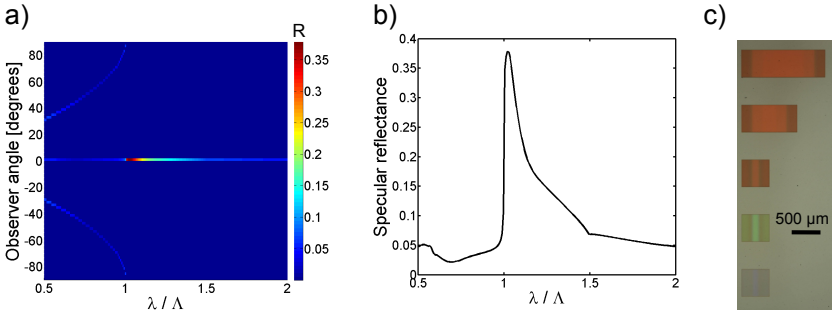

Figure 4.24: Calculated reflectance values for a thick foil with a grating on the front illuminated at normal incidence. a) Reflectance for a given wavelength and observer angle. For the given wavelength interval 0'th order as well as $\pm$ 1'st order are present b) The 0'th order reflectance showing a large peak just above $\lambda/\Lambda = 1$. c) Microscope image of gratings with three different periods leading to three different colors.

Angle-independent color effects can be achieved with a reflectance exceeding the corresponding planar Fresnel surface reflectance, for example in the case of a thick transparent foil. A thick foil can be defined as a slab of material with parallel front and back sides and with a thickness larger than the coherence length of the light under consideration. This implies no interference between reflections on the front and back. Therefore all surface effect calculations can be treated separately using RCWA and Fresnel coefficients for diffraction gratings and flat surfaces respectively.
The system under consideration is a transparent foil, of refractive index n_2, with a diffraction grating of period Λ on the top side. The foil is illuminated by white light at normal incidence. The back side is flat. With the given constraints, it is straight forward to set up a calculation of the efficiency of the reflected and transmitted orders of the full system using ray tracing. First, the incoming light interacts with the grating in the top surface producing both transmitted and reflected orders, of which the efficiencies may be calculated using RCWA. The transmitted orders propagate to the back side where they partly escape into the air and partly reflect back into the substrate. The reflected light from the back will again approach the front surface, now from the inside and it is again reflected and transmitted based to the grating geometry. By tracing all orders the total reflectance and transmittance can be found by summation of the escaped light.
Such a calculation has been made for a binary line grating of which both the protrusion height and width equals half the period. The reflectance as function of wavelength and observer angle is seen in Fig. 4.24a. The zero'th order reflection is located at 0 degrees, whereas the ± 1 orders are present for wavelengths smaller than the period at varying angles

according to the diffraction equation.
In Fig. 4.24b the 0 order reflectance is seen. Most noticeable is a large peak for wavelengths just higher than the period, reaching a level almost 10 times the Fresnel reflection of a flat surface. At the same time the peak is relatively sharp enabling bright colors to be produced. Three examples of such colors are seen in Fig. 4.24c, where a 0.1 mm thick Topas foil with imprinted gratings of periods 425 nm (blue), 505 nm (green), and 615 nm (red) is seen trough a bright field microscope. The gratings, which are here 350 nm deep, were originally fabricated in a silicon master using e-beam lithography and dry etching and then replicated in the foil using thermal imprint.
The strong peak in the zero'th order reflection is based on total internal reflection on the backside of the transmitted orders of the first interaction with the grating. For wavelengths satisfying $\Lambda < \lambda < n_2\Lambda$ the foil will support three orders (-1,0, and 1) while the air will only support one. This leads to total internal reflection of the ± 1 orders on the backside of the foil. For wavelength satisfying $\lambda < \Lambda$ there exists more orders in the air which the ± 1 can couple to, thereby lowering the Fresnel reflection on the backside. The process producing the strong peak is illustrated in Fig. 4.26, where the strengths of the first order fluxes are shown after the initial interaction with the grating (1a) and after reflection at the back side (1b). The Fresnel reflectance of the first orders on the back is also shown.

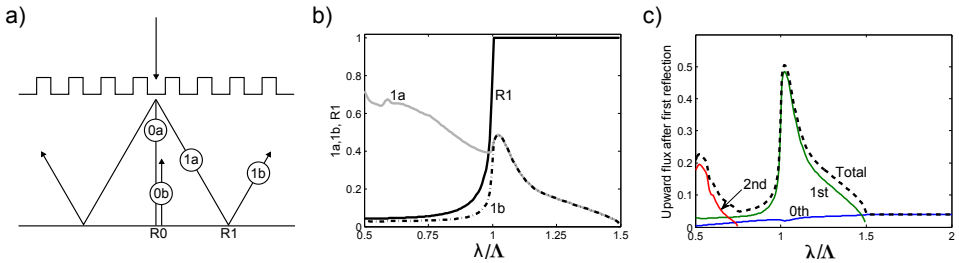

Figure 4.25: a) Illustration of different orders relevant for the creation of the sharp reflectance peak. b) The 1st order fluxes before (1a) and after (1b) reflection on the back side as well as back side reflectance, R1. c) Contributions to the upwards flux after one reflection on the back.

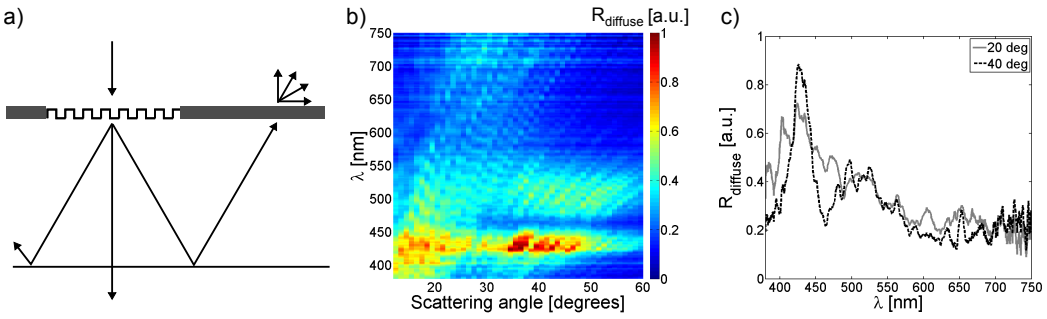

Figure 4.26: a) Conceptual sketch of alternating grating and diffuser sections. b) Angle resolved measurement of diffuse reflectance from gratings with period 405 nm for normal incident light is used c) Spectra at 20 and 40 degrees observer positions.

It is clear that two conditions must be fulfilled in order to get high strength of upwards going fluxes. The ± 1 order efficiency must be high and it should be totally reflected on the back. These conditions are only fulfilled for wavelengths just above the period leading to the significant peak. In Fig. 4.26c are the contributions to the total upwards flux after one reflection on the back shown. Here it is clear that the ± 1 orders are responsible for the

existence of the peak.
With the knowledge that the color information is lying in the total internally reflected first order fluxes (1b) it is possible to create a structure which facilitates a diffuse colored reflection upon normal incident light, rather than having the color information only in the specular direction. The principle is illustrated in Fig. 4.26a. The surface of the foil is covered by alternating sections of grating and diffuser elements. The diffuser elements, which enables the out coupling of the first order modes in various directions, could be fabricated in several ways. Refractive elements, such as micro lens arrays are effective diffusers[112], but the structure size of the lenses is not compatible with the design used her. Instead random binary diffusers[113] are used. In this ways the periodic gratings and diffusers may be fabricated in the same fabrication step. The widths of the sections are designed such that all total internal reflected first orders of the peak wavelength hits a diffuser.
Angle resolved measurement of the diffuse reflection for such a surface with a grating period of 405 nm is seen in Fig. 4.26b. A clear enhancement of the blue light in a wide angle interval is observed as also illustrated by the spectra at 20 and 40 degrees in Fig. 4.26c. The spectra somewhat noisy character of the spectra originates from the diffractive nature of the diffusers.

Acknowledgments

We acknowledge J. Scheel, DTU Nanotech, for photography. J. Weirch, Danish Fundamental Metrology, and J. Nørregaard, NIL Technology Aps, are acknowledged for fruitful discussions. This work was supported by the Danish National Advanced Technology Foundation (Contract No.: 007-2010-2) and by the European Commission via the FP7 MMP Integrated project PLAST4FUTURE (NMP2-SE-2012-314345).

4.5 Paper IV - Injection moulding antireflective nanostructures

Authors

Alexander B. Christiansen[a], Jeppe S. Clausen[b], N. Asger Mortensen[b], and Anders Kristensen[a].
[a] Department of Micro and Nanotechnology, Technical University of Denmark, Oersteds Plads, Building 345B, DK-2800 Kgs. Lyngby, Denmark.
[b] Department of Photonics Engineering, Technical University of Denmark, Oersteds Plads, Building 343, DK-2800 Kgs. Lyngby, Denmark.

Abstract

We present a method for injection moulding antireflective nanostructures on large areas, for high volume production. Nanostructured black silicon masters were fabricated by mask-less reactive ion etching, and electroplated with nickel. The nickel shim was antistiction coated and used in an injection moulding process, to fabricate the antireflective surfaces. The cycle-time was 35 seconds. The injection moulded structures had a height of 125 nm, and the visible spectrum reflectance of injection moulded black polypropylene surfaces was reduced from $4.5 \pm 0.5\%$ to $2.5 \pm 0.5\%$. The gradient of the refractive index of the nanostructured surfaces was estimated from atomic force micrographs and the theoretical reflectance was calculated using the transfer matrix method and effective medium theory. The measured reflectance shows good agreement with the theory of graded index antireflective nanostructures.

Introduction

The optical properties of injection moulded plastic products can be altered by nano-scale surface textures[79;114]. Antireflective (AR) structures which reduce reflectance by 2% can significantly improve the optical properties of a dielectric, in terms of reducing glare, with possible use for displays or polymer lenses[78]. AR structures in opaque materials have also been shown to enhance the colour appearance (chroma) of coloured plastics[115]. Other functionalities can be achieved using nanostructures, such as super hydrophobicity, and anti-fogging[25]. While these functionalities have been shown on lab-scale, there are still great challenges in developing industrial fabrication methods that can reduce the cost of such nanostructured materials.

Saarikoski *et al.* previously reported injection moulding of antireflective nanostructures in polycarbonate, from nanoporous anodized aluminium oxide, decreasing the reflectance from 5% to below 1% in the visible spectrum[114]. Black silicon[65] can likewise be used as a template for fabricating antireflective structures[93], despite the random nature of the structures. We have previously shown that black silicon can be optimized in order to minimize the scattering of light on the structured surface[78]. The antireflective properties of the nanostructures depend on the height of the structures, as well as the gradient profile of the refractive index, generated by the structures[20;116;117].

Although early works show that injection moulding of high aspect ratio nanostructures with low cycle times is possible[18], recent results still indicate that it is a challenging matter. Recent reports rely on dynamic heating and cooling[118–120], in order to obtain high aspect ratio structures.

Here we present a low cost method for fabricating antireflective polymer surfaces, based on mask-less reactive ion etched black silicon masters, and 35 second cycle-time conventional injection moulding from antistiction coated, electroplated nickel (Ni) shims. The

reflectance of the black, injection moulded polypropylene (PP) was measured using an integrating sphere, and was reduced from $4.5 \pm 0.5\%$ to $2.5 \pm 0.5\%$, in the visible spectrum. We compare the measured reflectance to the theoretical gradient index antireflectance, by estimating the gradient from atomic force micrographs of the nanostructured surfaces, and calculating the reflectance using the effective medium theory and the transfer matrix method. We thus show the direct relation between the incomplete filling of the nanostructures, and the impact it has on the desired optical property. This is useful for future optimization of the injection moulding process. Despite the shortcomings of the injection moulding process, we still obtain the desired optical effect of the nanostructures.

Theory

Light incident on an interface between two materials with different refractive indices, is subject to reflection, given by the Fresnel equation (at normal incidence)[49]

$$R = \left(\frac{n_1 - n_2}{n_1 + n_2} \right)^2 \tag{4.5.1}$$

where n_1 and n_2 are the refractive indices of the first and second medium respectively. For light in air ($n_1 = 1$), incident on a polymer surface ($n_2 = 1.5$), the reflectance amounts to 4%. Since the expression for R is quadratic in the difference between the value of the two refractive indices, the reflectance can be lowered by introducing one or more intermediate layers on the interface, with a refractive index, n, which obey $n_1 < n < n_2$. This can be realized by nanostructuring the surface using so-called moth-eye nanostructures[2]. Tapered moth-eye nanostructures provide a gradient in the effective refractive index over the interface which can be described as multiple thin layers, each with a gradually increasing refractive index. Due to the very small difference in refractive index, the reflectance at each interface becomes very small, and the total reflectance of the surface can in principle go to zero.

Clapham *et al.*[3] showed that very good antireflective properties can be obtained by gradient structures that obey the relation $d/\lambda > 0.4$, where d is the height of the nanostructures, and λ is the wavelength of the incident light. If we consider the visible spectrum of light, with wavelengths of 380-700 nm, the nanostructures should then have a height of around 280 nm or more. Structures with a smaller height will still be antireflective, but less effective.

The exact reflectance of a nanostructured surface can be calculated analytically, from the geometry of the nanostructures. If the volume fraction profile of the structures is known, this can be related to the effective refractive index profile, using effective medium theory. The effective refractive index n of two materials can be calculated using the Maxwell Garnett model[20;51]

$$\left[\frac{n^2 - n_1^2}{n^2 + 2n_1^2} \right]^2 = (1 - f_1) \left[\frac{n_2^2 - n_1^2}{n_2^2 + 2n_1^2} \right]^2, \tag{4.5.2}$$

where n_1 and n_2 are the refractive indices first and second medium, respectively, and f_1 is the volume fraction of the first medium.

In this paper, the volume fraction of the surface was measured with atomic force microscopy. The topographic data was divided in layers with a thickness of 1 nm. The effective refractive index of each of the layers was calculated using Eq. 4.5.2. The total reflectance of the resulting multilayer structure was calculated using the transfer matrix method[49]. In this way the theoretical reflectance was calculated, using actual topographical data.

Fabrication

The black silicon (BSi) substrates were structured by reactive ion etching (Pegasus DRIE, STS), see Fig. 4.27. The structures were formed in a single etching cycle with an O_2/SF_6-based etch[65]. The masters were patterned using conventional photolithography and isotropic dry etching to remove the nanostructures from the unmasked areas. A 90 nm seed layer of NiV was deposited on the Si masters using sputtering, and the masters were electroplated with Ni, to a thickness of 300 µm. The Si was subsequently dissolved in a 8.9 M KOH solution at 80°C. The etch time was approximately 9 hours. The nickel shims were coated with perfluorodecyltrichlorosilane (FDTS) using molecular vapor deposition. The Ni shims were inserted in the injection moulding tool, and the samples were fabricated using cycle times of up to 35 seconds.
An Ormocomp (a hybrid organic-/inorganic UV curable resin from Microresist Technologies GmbH) sample was casted from the Ni shim as well, using UV moulding (See Christiansen *et al.*[78] for details on the fabrication process). The Ormocomp replica has a very high resolution, and served as a reference for the characterization of the nanostructures and optical properties.

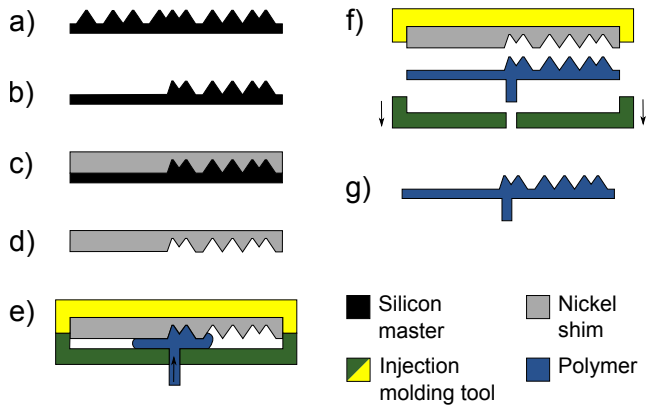

Figure 4.27: Fabrication process. a) Reactive ion etching of Si master. b) pattering using UV lithography. c-d) electroplating Ni shim. e-f) injection moulding. g) final part.

Results

SEM and AFM characterization

The Si master, Ni shim, injection moulded samples, and the Ormocomp replica were characterized using atomic force microscopy (AFM) and scanning electron microscopy (SEM). A PPP-NCH tip from Nanosensors (www.nanosensors.com) was used for the AFM characterization. Figure 4.28 shows scanning electron micrographs of the fabricated samples. The images show good resemblance between the nanostructures of the Ni shim, and those of the injection moulded samples. The characteristic distance between the nanostructures is around 210 nm (measured by Fourier analysis. See Christiansen *et al.*[78]). No significant changes to the Ni shim were observed after the injection moulding process.
The heights of the nanostructures were measured from atomic force microscopy micrographs, and are shown in Tab. 4.1. The standard deviation on the heights was estimated by measuring two to three AFM scans on different positions on each sample. The height of the structures on the Si wafer was additionally measured by breaking a similar master, and measuring the height from SEM profiles. The height was then measured to be 255±13 nm.

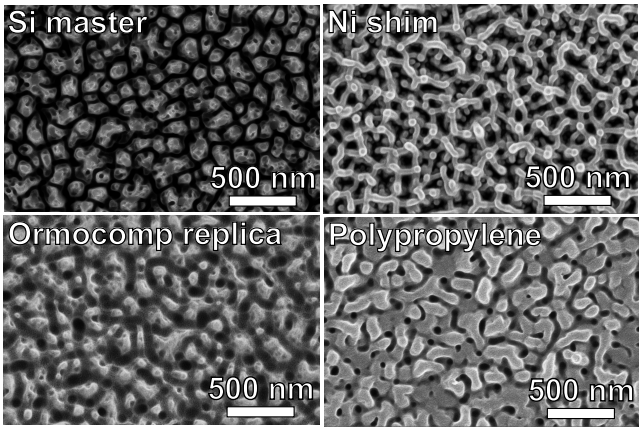

Figure 4.28: Scanning electron micrographs of nanostructured surfaces.

The AFM measurement thus underestimates the height by less than 5% for the tallest of the structures presented in this paper. Atomic force micrographs of the Si master, the Ormocomp replica, and the injection moulded polypropylene are shown in Fig. 4.29 (a)-(c). The AFM data were used to extract the volume fraction profiles of the structures, which are shown in Fig. 4.29 (d).

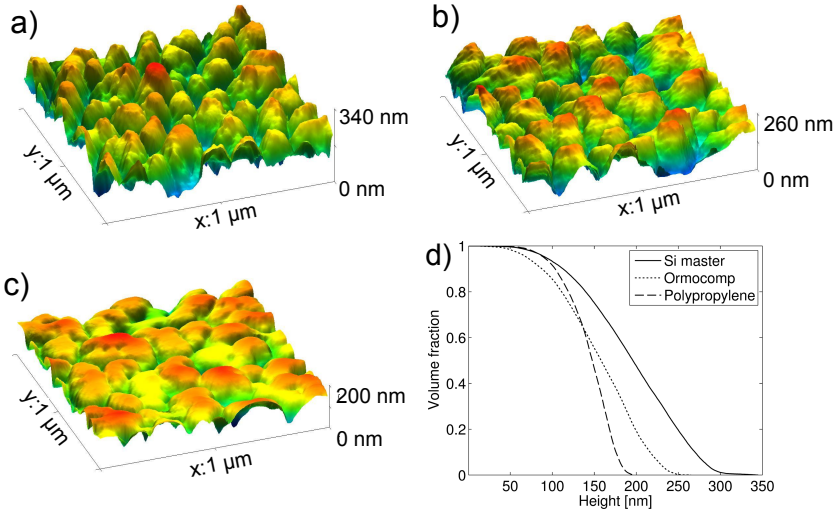

Figure 4.29: Atomic force micrographs of the nanostructured surfaces. a) The silicon master. b) Ormocomp replica of the Ni shim used for injection moulding. c) Injection moulded polypropylene. d) Volume fraction extracted from the data.

Reflectance measurements

The total reflectance of the samples was measured using an integrating sphere (ISP-50-8-R-GT, Ocean Optics) with collimated illumination at 8 degrees incidence. The light source was a xenon lamp, (HPX-2000, Ocean Optics) and for detection we used a spectrometer (Jaz, Ocean Optics). For the opaque PP samples, an aluminium mirror (100 nm Al deposited on a Borofloat wafer using electron beam evaporation) was used as reference sample. For the transparent Ormocomp samples, we used a Borofloat wafer as reference. The reflectance of the nanostructured side was calculated by subtracting the backside reflectance of a non-structured Ormocomp sample.

Sample	Polarity	Height [nm]
Si master	A	246 ± 25
Ni shim	B	230 ± 5
Ormocomp	A	214 ± 5
Polypropylene	A	125 ± 14

Table 4.1: Height of nanostructures, estimated from atomic force micrographs.

The reflectance of the planar and nanostructured polypropylene and Ormocomp is shown in Fig. 4.30. The planar samples are compared to the theoretical reflectance which can be calculated from the refractive index of the material. Here we have used $n = 1.49$ for PP, and $n = 1.52$ to $n = 1.54$ for Ormocomp. The theoretical reflectance of the nanostructured surfaces was calculated using the volume fraction from atomic force micrographs and the transfer matrix method, as described above.

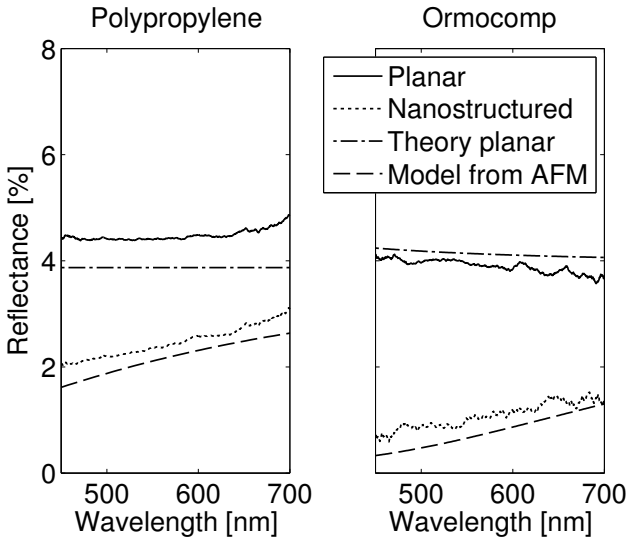

Figure 4.30: Reflectance of planar and structured polypropylene and Ormocomp. The reflectance is compared to the theoretical reflectance of the two planar materials, as well as the structured, by using the gradient model, and the volume fraction extracted from AFM data.

Discussion

The measured and calculated reflectance show good agreement for both the injection moulded PP, and the Ormocomp replica, thus validating the theoretical description of the effect of the nanostructures. The findings suggests that optimization of the injection moulding process could further decrease the reflectance of the surfaces, by increasing the height of the nanostructures.

The injection moulded parts are shown in Fig. 4.31. Each of the square parts are 1.6×1.6 mm^2. The nanostructured areas appear darker in diffuse, and in particular in specular lighting conditions. The nanostructured areas are indicated by arrows. Figure 4.31 (b) shows a close up of a part with a DTU logo, which is comprised of nanostructured areas surrounded by a planar area.

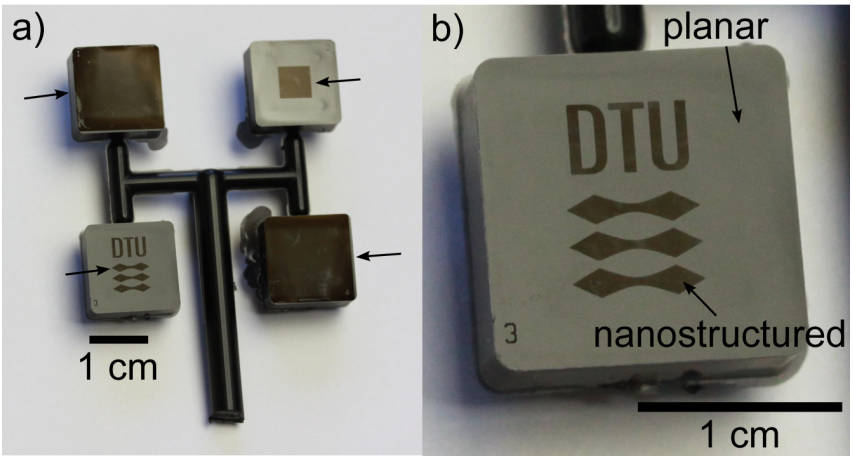

Figure 4.31: Injection moulded sample. The antireflective structures are seen as darker areas, and are indicated by arrows. The largest areas are 16×16 mm^2.

Conclusion

In conclusion, we injection moulded nanostructures with a characteristic inter-distance of 210 nm, with a height of up to 125 nm in polypropylene. The injection moulded structures show good antireflective functionality, as the reflectance of polypropylene is decreased from $4.5 \pm 0.5\%$ to $2.5 \pm 0.5\%$ in the entire visible range. The reduction is sufficient for providing a visible effect on the injection moulded parts, and could provide a antireflective effect for e.g. displays, if fabricated in a transparent material. However, further optimization of the process is needed in order to compete with high-quality optical coatings. The reflectance is compared to an Ormocomp replica of the Ni shim, which had a height of 215 nm and showed a decrease in reflectance from 4% to 1%. The gradient of the refractive index of the nanostructured surfaces was estimated from atomic force micrographs, and the theoretical reflectance was calculated using the transfer matrix method, and effective medium theory. The measured reflectance shows good agreement with the theory of graded index antireflective nanostructures.

Acknowledgments

We thank Claus Højgaard, DTU Danchip for electroplating of Ni shims and the Danish Technical Institute for FDTS coating of Ni shims. This work was supported by the NanoPlast project funded by the Danish National Advanced Technology Foundation (File No.: 007-2010-2) and by the European Commission via the FP7 MMP Integrated project PLAST4FUTURE (NMP2-SE-2012-314345).

4.6 Paper V - Binary antireflective nanostructures

Antireflective (AR) nanostructures have been shown to be a potential alternative to thin film coatings for optical components and devices. AR nanostructures can be classified as gradient and binary type. Gradient type consist of tapered nanostructures that facilitate a gradient in the effective refractive index over the surface, while the binary type structures form a single layer with an effective refractive index which can be tuned by the volume fraction of the nanostructures.

The binary AR structures have the virtue that they in theory can be designed to achieve 0% reflectance at a specific wavelength. This makes them particularly interesting for lasers. Kanamori *et al.* took advantage of this in a recent paper, where they fabricate binary AR nanostructures directly on the tips of fibers for optical communications wavelengths[27]. The structures were fabricated using e-beam lithography, and were pillars with a diameter of 560 nm, a period of 700 nm, and a height of 250 nm. They were designed for a wavelengths of 1550 nm, for which the optimum height is 320 nm. The reflectance of the structures was measured in the wavelength range 1460 nm to 1580 nm, and was reduced to 0.27%, from roughly 4%. David *et al.* fabricated binary AR structures for visible wavelengths using 1D gratings[28]. The structures were fabricated in a quartz wafer using e-beam lithography, from which a Ni shim was electroplated. The structures were then hot embossed in 1 mm thick polycarbonate sheets. the reflectance of a single interface was lowered from around 5% to 1% at 600 nm. However, the reflectance increased significantly for smaller wavelengths.

Here, 2D binary antireflective structures were fabricated by nanostructuring an Si master using fast e-beam writing, etching the master using RIE, and using the master to cast an Ormocomp replica. The reflectance of the Ormocomp sample was reduced to between 0.5% and 2% in the visible spectrum, compared to 4% of a planar sample.

Design

When the period of the structures is below the diffraction limit, the refractive index of the nanostructured layer can be described by effective medium theory. In this regime the only two design parameters are the height of the layer and the volume fraction of material in the layer. From the Fresnel equation it can be shown that minimum reflectance from a single layer is achieved when the refractive index of the layer is given by $n_{\text{eff}} = \sqrt{n_1 n_2}$, where n_1 and n_2 are the refractive index of the incident and substrate media respectively[48]. Furthermore, total destructive interference can occur if the phase difference between the two reflected waves is $\delta = \pi$. This is achieved for normal incidence when the thickness of the layer is given by[48]

$$d_1 = \frac{\lambda}{4n_{eff}}. \tag{4.6.1}$$

where λ is the wavelength in vacuum. This means that the structure will work most efficiently at a single wavelength and that the efficiency will decrease when the wavelength changes.

The effective refractive index of the nanostructured layer can be calculated by the Maxwell Garnett effective medium theory as[51]

Sample	Volume fraction, f_2	Diameter	Height
	%	nm	nm
Si master	44	112	94
Ormocomp replica	43	111	93

Table 4.2: Geometry of the fabricated master for binary AR structures, and the Ormocomp replica. The volume fraction and diameter (of holes in the master, and protrusions in the Ormocomp) was calculated from SEM images. The heights of the structures were measured from AFM data.

$$\varepsilon_{\text{eff}}^{\text{MG}} = \varepsilon_1 \frac{\varepsilon_2(1+2f_2)-\varepsilon_1(2f_2-2)}{\varepsilon_1(2+f_2)+\varepsilon 2(1-f_2)} \tag{4.6.2}$$

where ε_1 and ε_2 are the relative permeabilities of the incident and substrate media respectively, and are related to the refractive index by $n^2 = \varepsilon$. The parameter f_2 denotes the volume filing fraction of the substrate in the nanostructured layer. For a substrate material with refractive index $n_2 = 1.5$, and $n_1 = 1$ for air, the optimum effective refractive index $n_{\text{eff}} = \sqrt{n_1 n_2}$, is achieved at a volume fraction of around $f_2 = 0.5$.
Here we design the structures for a wavelength of 500 nm, and a refractive index of $n_2 = 1.5$. From Eq. 4.6.1, it follows that the height of the nanostructures should be 100 nm. As discussed above, the volume fraction of polymer in the nanostructured layer should be $f_2 = 0.5$. The period of the 2D array was chosen to be 150 nm, in order to avoid diffraction for all incident angles

Fabrication

A ZEP520A:Anisole (1:1) solution (ZEP520A from ZEON) was spincoated on a Si wafer, at 3000 RPM, and baked at 185 ° for 8 min. The resist thickness was 200 nm. The nanostructures were exposed with the fast electron beam writing method, described by Gadegaard *et al.*[19;75]. With this method, each structure is defined by a single exposure to the beam. The period of the structures is thus defined by the distance between each exposure point. The size of the structures is defined by the beam spot size, and the exposure dose. For a 2D square array with a period of 150 nm, the holes should have a diameter of around 100 nm, in order to obtain a volume fraction of $f = 0.5$. In order to achieve this, different exposure doses were used, ranging from 20 to 400 μC cm^{-2}. The structures were exposed using a writing field of 600×600 μm^2 to avoid defocussing at the field edges, as described by Gadegaard *et al.*[19]. The total writing time was 2.2 hours, corresponding to a writing time of roughly 2 hours/cm^2. After the exposure the wafer was developed in ZedN50 for 120 seconds, followed by immersion in isopropyl alcohol for 30 seconds.

The exposed and developed resist was characterized with SEM. The clearing dose was seen to be around 60 μC cm^{-2}, while the exposed holes started to merge at 200 μC cm^{-2}. At 300 μC cm^{-2} the structures were overexposed, and no structures were left. The best results were for 100 μC cm^{-2}. Here, well defined arrays of circular holes were seen in the resist. However, there was still some variation in the exposure, within each writing field of 600×600 μm^2, as the size of the exposed holes was varying from one corner of the writing field to another.

The wafer was etched using reactive ion etching (Pegasus DRIE, STS), using an anisotropic etch, with an etch time of 40 seconds. The resist was removed using an O_2/N_2 plasma, before the wafer was coated with perfluorodecyltrichlorosilane (FDTS) using molecular vapour deposition (MVD 100 Molecular Vapor Deposition System, Applied Microstructures Inc.).
Ormocomp replica were cast from the wafer using a UV-nano imprint lithography process. 1.5 ml Ormocomp was applied to the Si master, and a PMMA substrate was applied on top in order to planarize the Ormocomp layer. The Ormocomp was then cured by exposure to UV light through the PMMA substrate, using a UV flood exposure source (1000 W Hg(Xe) Oriel Flood Exposure Source, unit 92540). The PMMA substrates were Plexiglas XT 20070 which has a limited but sufficient transmittance in the 260-320 nm wavelength range.

Characterization

The Si samples were characterized using SEM and AFM, as shown in Fig. 4.32. For AFM a high aspect ratio tip was used in order to reach the bottom of the holes (AR10T-NCHR from Nanosensors[121]). The depth of the holes was measured to be 94 nm (measured as the peak-to-peak distance on the height-histogram of the image). The volume fraction of the holes on the master was estimated from SEM and was 46% for the area exposed with a dose of 100 $\mu C\ cm^{-2}$.

One of the Ormocomp replicas was characterized using SEM, after cleaving the sample and depositing a thin gold film using sputter-deposition (Hummer sputter coater, Anatech). The volume fraction was measured to be 43%, and the diameter of the pillars was 111 nm. The height of the pillars was measured to be 93 nm, using AFM. The measured values of the Si master and the Ormocomp replica are compared in Tab. 4.2.

The structures appear larger on the AFM scan, than what is measured from SEM, due to tip convolution. The AR10T-NCHR tips from Nanosensors have a tip diameter of < 30 nm at the apex, which increases to roughly 120 nm at 1.5 μm[1] The diameter (FWHM) of the pillars was measured from the profile of the original AFM image, seen in Fig. 4.32 (f). The diameter was 150 nm, which is roughly 40 nm larger than expected from the SEM images. This corresponds well with the expected size of the AFM tip.
In order to compensate for the tip convolution, a deconvolution of the image was made using the Scanning Probe Imaging Processor software (SPIP 6.2.5 from Image Metrology, Hørsholm, Denmark)[122]. The deconvolution is a blind deconvolution algorithm, which does not require any information about the tip. Normally one scans a surface which has very sharp features, in order to make a good image of the apex of the tip. This image can then be used to deconvolute other AFM images, measured with the same tip. Here we will simply use the deconvolution algorithm to obtain a more accurate image of the surface, while keeping in mind that the deconvolution might not be completely accurate.

A profile of the deconvoluted image is shown in Fig. 4.32(g) and the diameter of the pillars was 106 nm. This suggests that the deconvolution was not entirely accurate, as discussed above. However with the knowledge about the pillar diameter from the SEM data, we establish that the deconvoluted image does indeed give a better representation of the pillar diameter, than the original image. This allows us to calculate a more accurate volume fraction profile of the surface, from which the theoretical reflectance can be calculated, and

[1] Datasheet for the tips is found on Nanosensors' home page.

compared to the measurement.
The volume fraction profile was calculated from the AFM image, and is show in Fig 4.33. The profile is compared to that of an 8th order super-Gaussian profile, and a perfect cylinder. As seen, the fabricated structures are not perfectly binary, but can be estimated by 8th order super-Gaussian shapes.

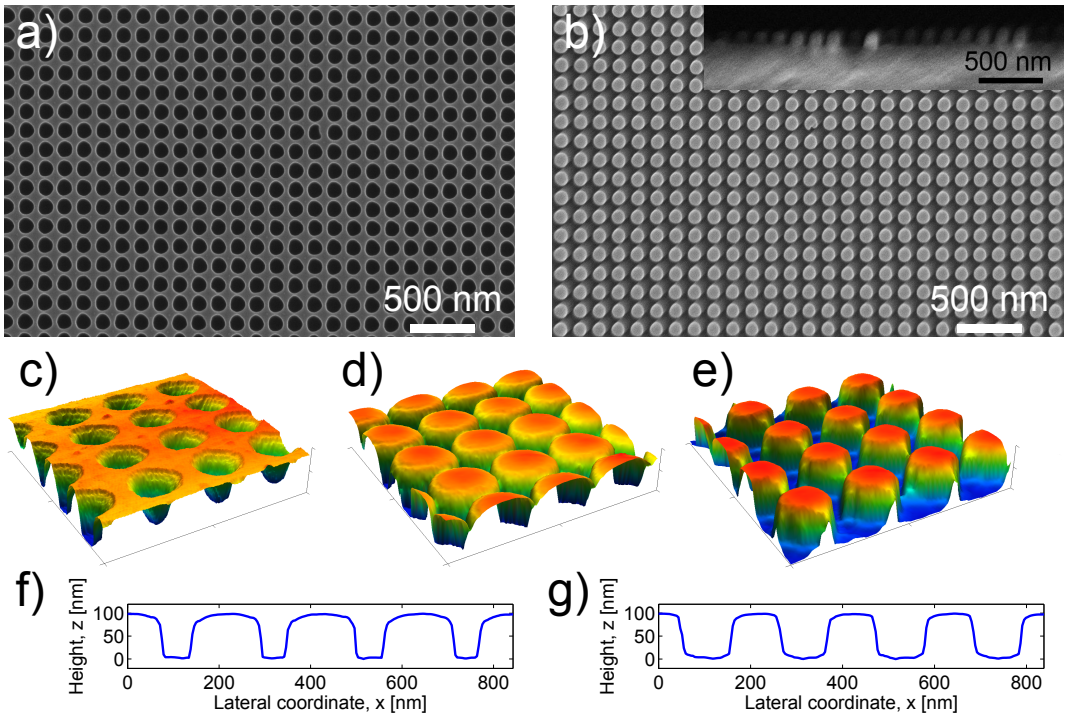

Figure 4.32: Characterization of binary AR structures. a) SEM image of Si master. b) SEM image of Ormocomp replica. The insert shows a sideview of the structures. c) AFM scan of the Si master. d) Original AFM scan of Ormocomp replica. e) Deconvoluted AFM image of Ormocomp replica. f) Profile of original AFM image. g) Profile of the deconvoluted AFM image.

Results and discussion

The reflectance of the binary AR structures in Ormocomp was measured using an integrating sphere and compared to the reflectance of a planar Ormocomp sample. A 100 nm thick Al film on borosilicate float glass, which was deposited using e-beam vapour deposition (Alcatel SCM 600), was used a reference for the measurement. Figure 4.34 shows that the reflectance decreases from roughly 4% for a planar sample, to 0.5% at 400 nm wavelength, and 2% at 700 nm wavelength. The nanostructured area was 0.25 cm^2.

The measured reflectance was compared to the theoretical reflectance calculated from AFM data of the surface topography, showing that the measurement and theory are in very good agreement. At low wavelengths the measured reflectance is slightly larger than that of the theoretical reflectance, which could be due to scattering from irregularities in the structures[30]. The reflectance of the 8th order super-Gaussian profile (not shown) is practically identical to that of the AFM profile, as the absolute deviation in reflectance is less than 0.1% within the visible spectrum.

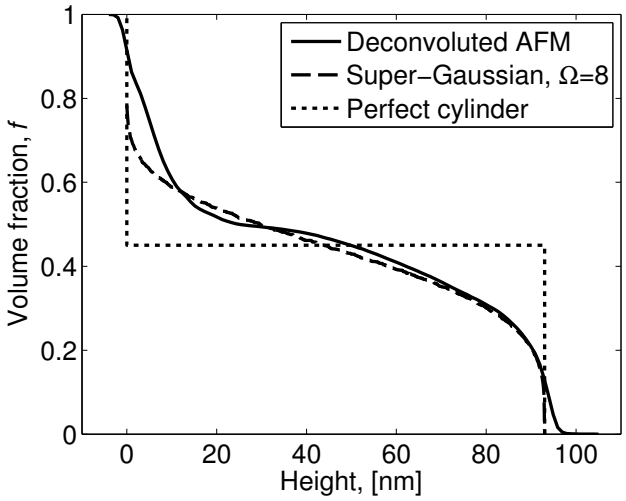

Figure 4.33: Volume fraction profiles of the deconvoluted AFM image of fabricated binary structures, a super-Gaussian profile of 8th order, and an ideal cylinder.

The binary AR structures were designed to have a reflectance below 1% in the visible spectrum, which was not achieved. One reason for this is that the depth of the etch was not accurate, as the etched depth of the Si master was 94 nm instead of the expected 100 nm. From Eq. 4.6.1 it is seen that a decrease in structure height, will cause a shift of the reflectance minimum towards lower wavelengths. A second factor is the non-ideal shape of the fabricated structures, which is not perfectly binary, but is somewhat rounded. The rounding further causes a shift towards lower wavelengths, as the structures start to resemble gradient type AR structures [3].

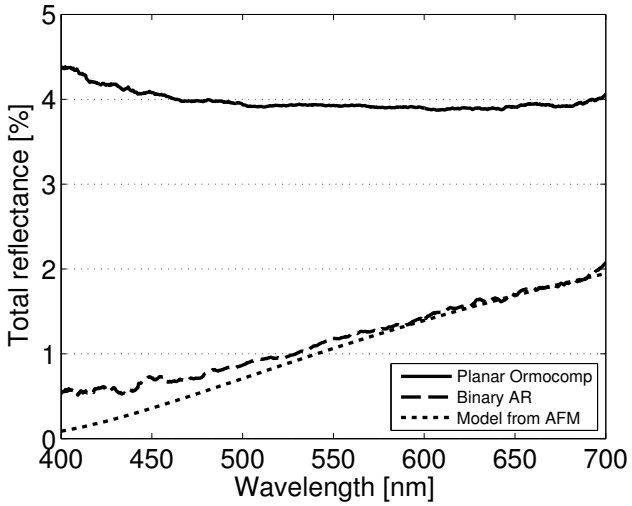

Figure 4.34: Reflectance measurement of Binary AR structures in Ormocomp. The binary structures show a significant reduction in reflectance, compared to a planar Ormocomp film. The measured reflectance compares well to the reflectance calculated from AFM data of the surface topography.

Conclusion

A master for binary AR structures was fabricated using fast e-beam lithography. An Ormocomp replica was made from the master using a UV-nano imprint lithography process. The reflectance was reduced from roughly 4% for a planar sample, to 0.5% at 400 nm wavelength, and 2% at 700 nm wavelength. The nanostructured area was 0.25 cm^2. The results show that it is possible to significantly reduce the reflectance in the visible spectrum, using binary AR nanostructures, and that these can be fabricated using the fast e-beam writing method. The structures are however highly dependent on the precision of the fabrication, as small variations in the shape and the height of the structures can significantly impair the antireflective effect.

It was shown that it is feasible to use the fast EBL method to fabricate large areas of periodically structured surfaces, with feature sizes of 100 nm, and a period of 150 nm. The writing time was approximately 2 hours/cm^2. There are some limitations to the method however. Due to the Gaussian shape of the electron beam, and that each feature is the result of a single spot exposure, the feature size is extremely dependent on the exposure dose. Furthermore the actual beam shape, the focusing of the beam, and variations in the beam focus within the writing field are critical.

4.7 Discussion

The five papers have discussed the feasibility of achieving optical functionality in polymers by nanostructuring using industrial methods such as injection moulding.

Papers I, II and IV discussed the use of BSi structures for achieving colour and AR functionality. It was shown that BSi structures with lateral sizes around 1 μm would scatter incoming light, while smaller structures with a lateral sizes around 160 nm would not scatter visible light significantly. Using BSi nanostructures with a height of 200 nm and aspect ratio of 1.3, it was possible to reduce the reflectance of Ormocomp samples by a factor of 2.

Paper V discussed fabrication of binary AR structures using fast EBL. The structures were fabricated in Ormocomp and resulted in a decrease in reflectance from roughly 4% for a planar sample, to 0.5% at 400 nm wavelength, and 2% at 700 nm wavelength. It is believed that the structures could be optimized further by taking into account that the fabricated structures can be described by 8th order super-Gaussian shapes. This can be compensated for by designing the height of the structures to be 125 nm, as discussed in Sec. 2.6.2.

Paper IV showed that it is possible to fabricate antireflective nanostructures using injection moulding, although complete filling of the structures was not achieved, which impaired the antireflective effect. Despite the imperfect replication, the nanostructured surfaces still showed improved optical properties, compared to planar surfaces. On the black PP samples, the nanostructured surfaces appeared as darker areas. The effects of nanostructures in opaque polymers have been studied further in a recent paper by Clausen *et al.*[115]. Here the nanostructures were fabricated by hot embossing in ABS using a BSi master. The results showed that the nanostructures increased the chroma of blue, green, and red samples, resulting in a more intense colour of the samples. The results of paper IV show that such colour improvements are feasible by injection moulding.

Although it might be possible to further increase the effect of the injection moulded BSi AR structures, by optimising the process in paper IV, there will likely be a trade-off between effect and cycle time. Binary AR structures might prove to be an interesting alternative for injection moulding, as they require lower aspect ratios than the gradient type AR structures. In particular if the masters could be fabricated using interference lithography, or by using APA masters. Even with the fast EBL method discussed here, the fabrication costs for the masters is quite high. Furthermore, it was shown that random structures require a smaller characteristic length scale than periodic structures, in order to avoid scattering. This means that periodic structures have a lower requirement for the resolution of the fabrication process.

The discussion in paper III showed that angle-independent structural colours is not feasible to achieve by nanostructures which can be injection moulded or hot embossed, due to the low reflectance of polymers. Structural colours which are feasible to fabricate in polymers using injection moulding are the diffractive colours from gratings, which were shown in paper III, and the enhancement of colours from antireflective nanostructures discussed by Clausen *et al.*[115]. In order to achieve vivid and angle-independent colours it would be necessary to e.g. use metallization of injection moulded structures, similar to the method discussed by Kumar *et al.*. In Chap. 5 a method for achieving black surfaces by metallization of nanostructured polymer surfaces will be discussed.

5

Black metal

As discussed in the previous chapter, the low refractive index of polymers sets a limit for the colour functionalities which can be realized used nanostructures. In this chapter we discuss how metal films which are deposited on nanostructured polymer surfaces, can be used to create very strong optical effects.

In particular, we will discuss how black films can be fabricated by depositing thin metal films on nanostructured dielectric surfaces. The nanostructures were fabricated using BSi masters, and incidentally resemble the antireflective structures investigated in the previous chapters, and papers. With this simple approach, the reflectance of a 100 nm thick Al film was reduced from 80% to 6%, and the absorbance was increased from 20% to over 90%. Highly absorbing Au, Ag, and Cr films were also shown, on areas with a diameter of 5 cm. The advantage of this approach is that the substrate can in principle be any material, and can thus potentially be manufactured by industrial methods like injection moulding or roll-to-roll imprinting, followed by metal deposition.

5.1 Fabrication

The BSi masters were structured by RIE (Pegasus DRIE, STS). The structures were formed in a single etching cycle with an O_2/SF_6-based etch. Different structures were obtained by varying the O_2 flow[65] (See Tab. 5.1). Note that the structure types A-E discussed in this chapter do not correspond directly to the structure types which were discussed in paper II, Sec. 4.3. As discussed in Sec. 3.1, the O_2 is used to form the $Si_xO_yF_z$ passivation layer which prevents the Si from being etched. As the O_2 flow is decreased, the passivation layer is readily removed by sputtering at the bottom of the structures, and the etch rate in these areas increase. This results in the formation of cone or needle like structures. The spacing between the structures also increases, which could be due to some of the structures being etched away, due to the limited formation of the passivation layer. The different structures are shown in Fig. 5.1 (a).

The BSi masters were coated with FDTS, using molecular vapour deposition. The masters were then used in a UV-NIL process for replicating the structures into Ormocomp, as described in Sec. 3.4. The structures were fabricated by a single replication process. The Ormocomp structures are shown in Fig. 5.1 (b), where they are compared to the structures on the BSi masters.
Figure 5.2 shows top view SEM images of the BSi masters, and the Ormocomp replicas.

	Structure type				
Parameters	A	B	C	D	E
Platen chiller temperature [°C]	-10				
Coil power [W]	2700				
Platen power [W]	30				
Pressure [mTorr]	6				
SF_6 flow [sccm]	70				
O_2 flow [sccm]	110	100	90	80	70
Etch time [min]	8				

Table 5.1: RIE parameters for the BSi masters. Only the oxygen flow was varied, with increments of 10 sccm. Note that the structure types do not correspond to those discussed in paper II, Sec. 4.3.

Type	Height [nm]	Length scale [nm]
A	315 ± 35	150 ± 10
B	450 ± 50	160 ± 10
C	615 ± 80	195 ± 10
D	815 ± 120	230 ± 15
E	880 ± 140	245 ± 15

Table 5.2: Measured height and characteristic length scale of the fabricated BSi masters.

The images show that the density of structures in type A to D is very high, while the density of structures is lower for the type E structures.
Thin metal films with thicknesses ranging from 10 to 100 nm were deposited on the structured Ormocomp samples, using electron beam physical vapour deposition (Alcatel SCM 600), at a rate of 15 Å/s. The thickness of the metal layer was controlled by a piezo-electric crystal in the evaporation chamber. Thermal deposition of Al and Ge was performed with a Wordentec QCL 800 system. An example of a 100 nm thick e-beam evaporated Al film on type C nanostructures is shown in Fig. 5.3. The upper face of the Ormocomp sample on which the metal is deposited is referred to as the air-metal interface. The bottom face is referred to as the Ormocomp-metal interface.

Figure 5.4 shows photographs of the five different structures, on which Al films with thicknesses of 10, 15, 20, 30, 40, 60, 80, and 100 nm were deposited. The photos were taken from the Ormocomp-metal interface. As seen, the nanostructured films become darker with increasing metal thickness, indicating high absorption in the metal layer.

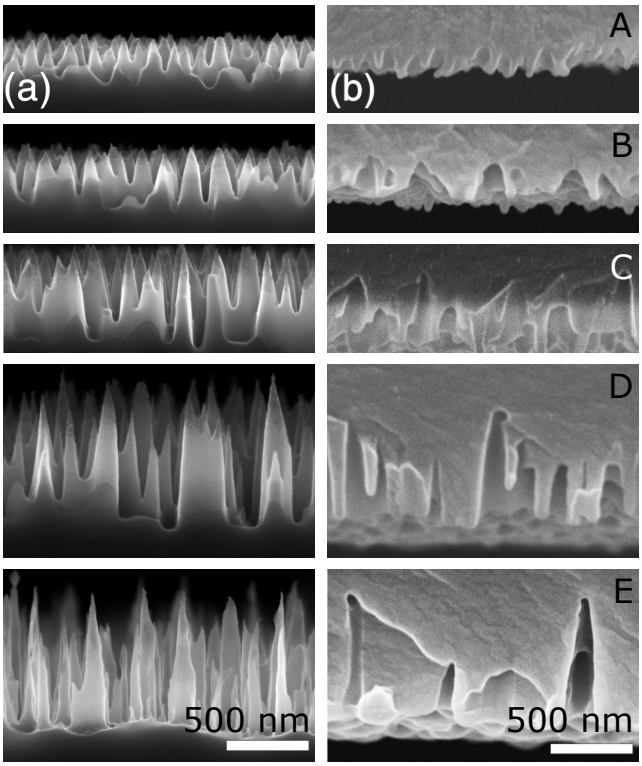

Figure 5.1: Profile view of BSi masters, and Ormocomp replicas. a) SEM images showing the profile of the BSi masters, of type A (top) to E (bottom). b) The Ormocomp replicas of the BSi masters.

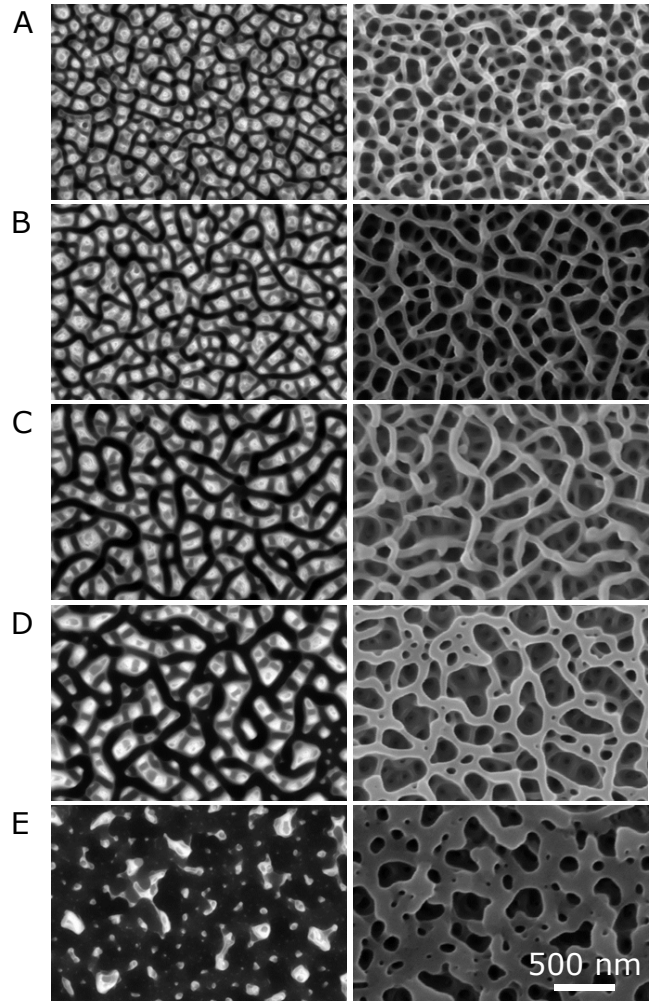

Figure 5.2: Top view of BSi masters, and Ormocomp replics. a) SEM images showing the top view of the BSi masters, of type A (top) to E (bottom). b) The Ormocomp replicas of the BSi masters.

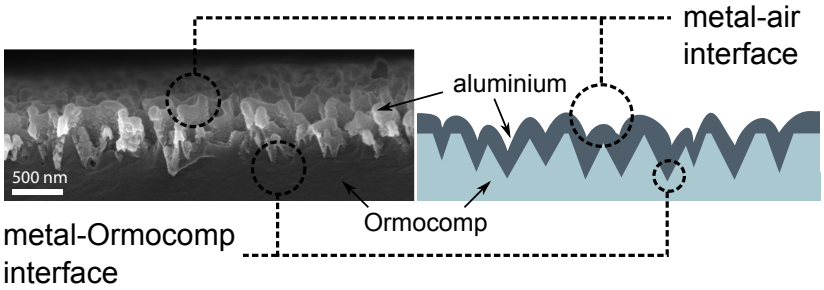

Figure 5.3: Thin metal film deposited on nanostructured Ormocomp surface. 100 nm Al deposited on a type C Ormocomp structure, using e-beam evaporation. The sketch defines the Ormocomp-metal, and air-metal interfaces.

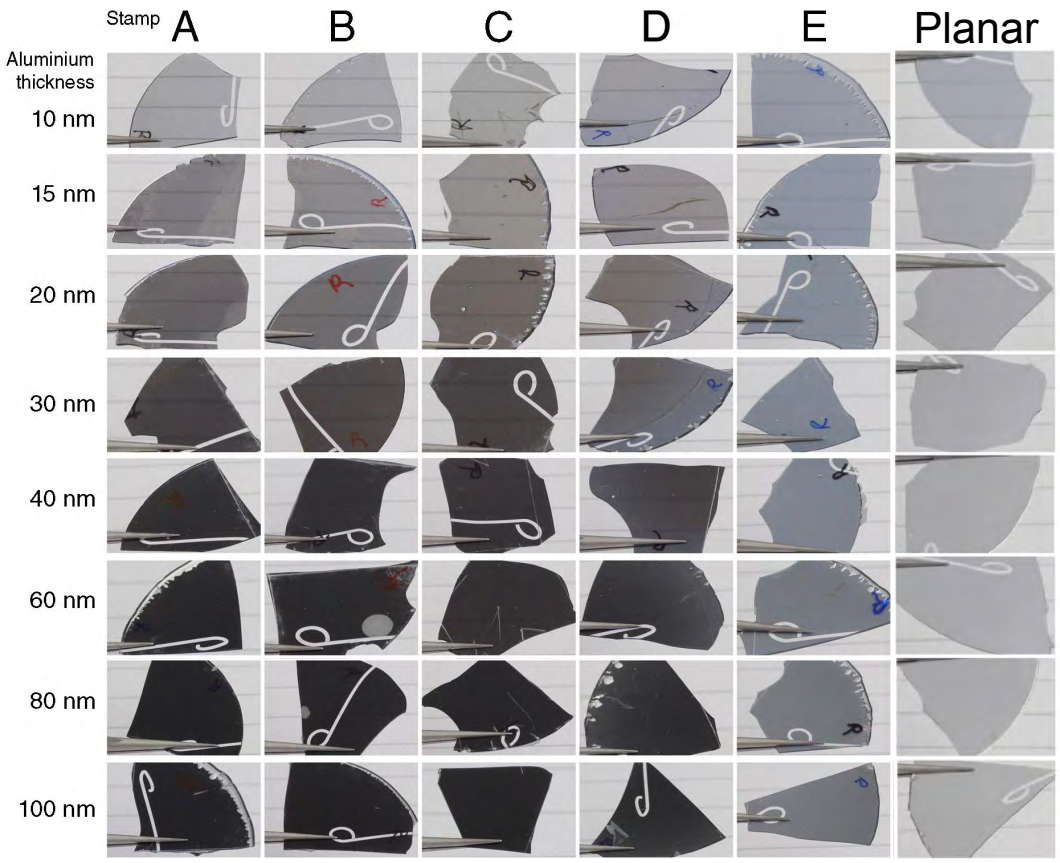

Figure 5.4: Photographs of thin metal films on nanostructured Ormocomp samples. Photos are taken from the Ormocomp-metal interface. Each column shows structures of type A to E, or a planar Ormocomp sample. Each row represents an Al film thickness from 10 to 100 nm.

5.2 Optical measurements

The reflectance of the samples was measured using an integrating sphere, as discussed in Sec. 3.6.2. A 100 nm thick Al film deposited on a borosilicate float glass wafer by e-beam vapour deposition (Alcatel SCM 600), was used as reference. The specular transmission measurements were performed as described in Sec. 3.6.1. The absorption in the metal films was calculated as $A = 1 - R - T$.

5.3 Results

5.3.1 Ormocomp-metal interface

Figure 5.5 (a) and (b) show the measured reflectance of planar and nanostructured thin metal films respectively. The reflectance was measured from the Ormocomp-metal interface. While the reflectance of a planar film increases dramatically with the film thickness (as discussed in Sec. 2.7.1), the nanostructured films show a remarkably low reflectance which virtually does not increase as function of metal film thickness. Furthermore, the dispersion in the reflectance is very small, amounting to below 1% (absolute percentage) within the visible spectrum.

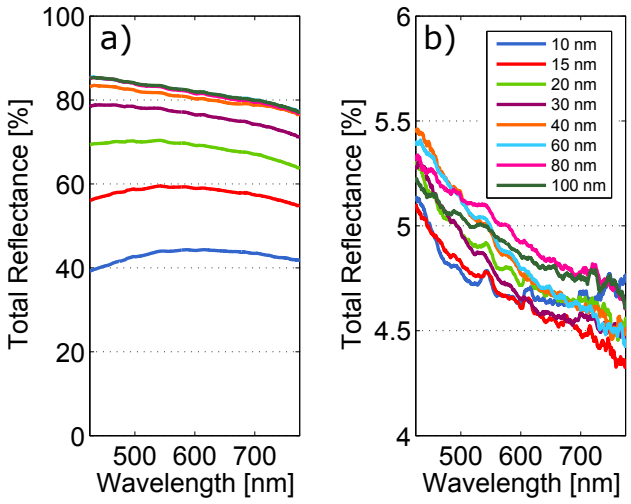

Figure 5.5: Reflectance of planar and nanostructured thin metal films. a) Reflectance of a planar film as function of wavelength, for different thicknesses. b) Reflectance of nanostructured thin metal films (on type B nanostructures).

The measured reflectance and transmittance, and calculated absorbance for all the structures is plotted as a function of film thickness in Fig. 5.6, at 500 nm wavelength. Due to the relatively low dispersion, the optical properties at 500 nm wavelength sufficiently represents the optical properties within the visible spectrum. The reflectance of the nanostructured thin films is changed dramatically, compared to the planar thin film. As discussed above, the reflectance of the planar film increases rapidly, while the nanostructured thin films of type A-D show only a slight increase in reflectance, to a maximum of 6% for a thickness of 100 nm. The transmittance decreases rapidly for both the planar and the structured films although the transmittance of the nanostructured films is significantly larger than the planar. The decay in transmittance is also slower for the nanostructured films, compared to the

planar. The reduced reflectance of the nanostructured films result in a dramatic increase in the absorbance, which increases to 90% for the nanostructured films of type A-D.

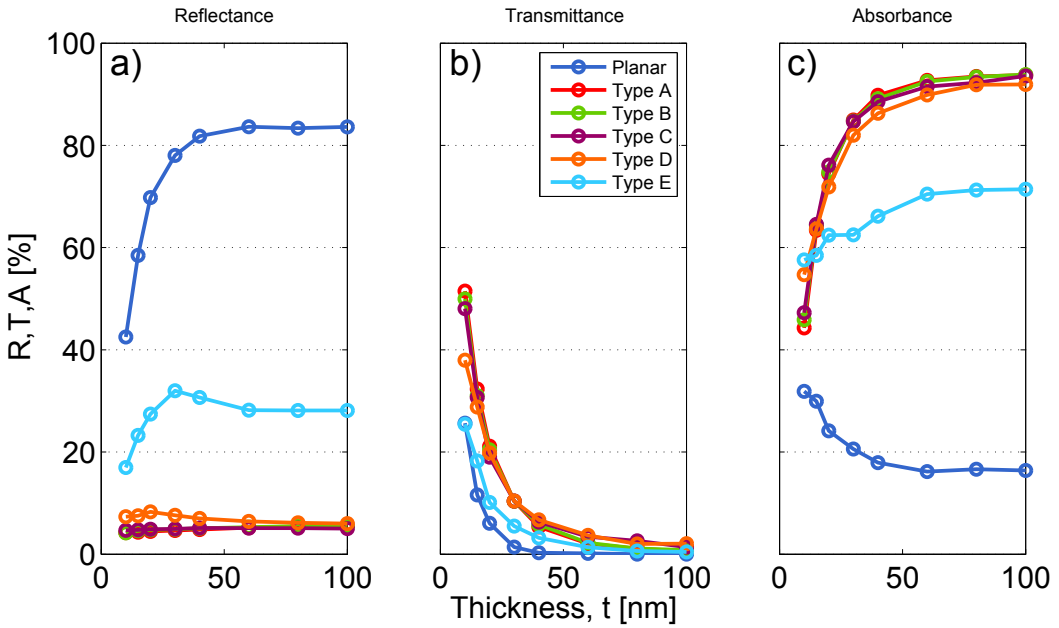

Figure 5.6: Optical measurements of the Ormocomp-metal interface, for different structures and metal thickness at 500 nm wavelength. a) Total reflectance as function of metal thickness. b) Measured transmittance. c) Absorbance calculated as $A = 1 - R - T$.

5.3.2 Air-metal interface

The properties of the air-metal interface is important for metal films deposited on opaque materials, and the difference between the air-metal interface, and the Ormocomp-metal interface might also give a further understanding of which factors are important for fabricating black metal films.

Figure 5.7 shows photos of the air-metal interfaces, i.e. the metal side is facing towards the camera. The samples are held in a distance of a few centimetres from the background, in order to show the transmission properties of the samples. Like the Ormocomp-metal interface shown in Fig. 5.4, the structured Al films are transparent up to a thickness of around 30 nm (the lines in the background is visible through the samples). But where the Ormocomp-metal interfaces got darker for increased metal thickness, the air-metal interface are darkest for thicknesses of 30-40 nm.

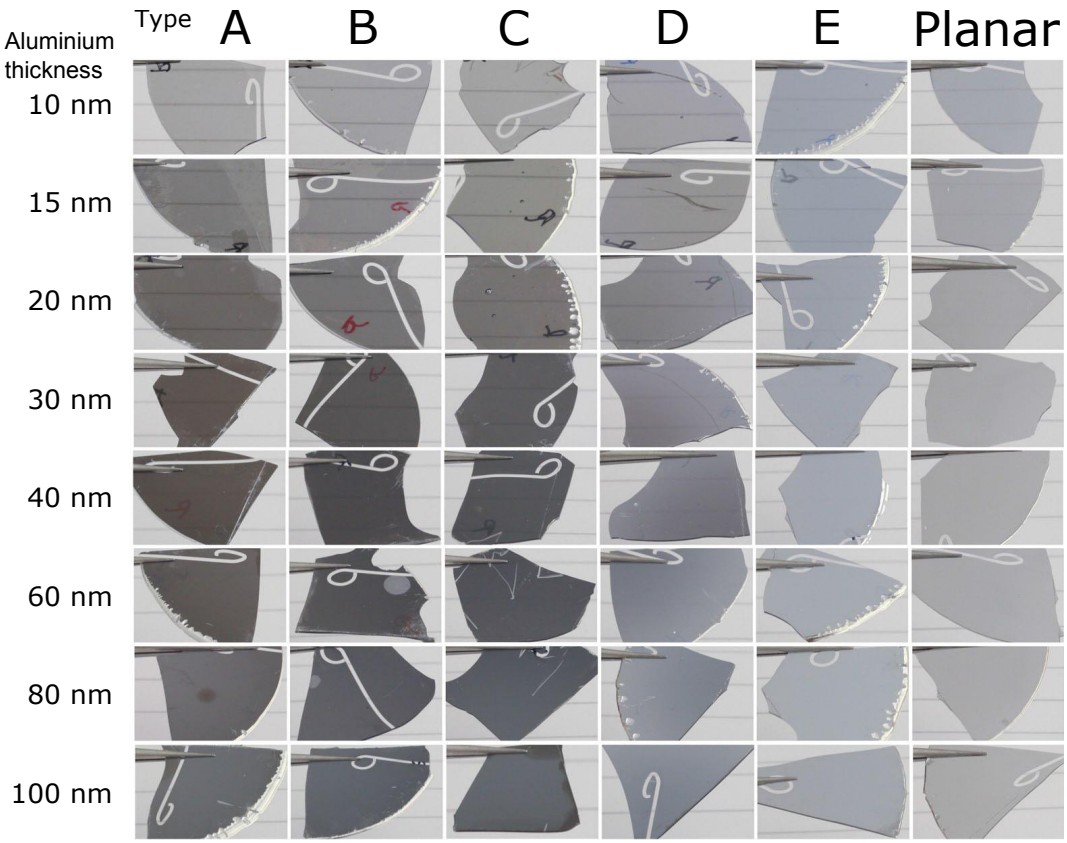

Figure 5.7: Photographs of thin metal films on nanostructured Ormocomp samples. Photos are taken from the air-metal interface. Each column shows structures of type A to E, or a planar Ormocomp sample. Each row represents an Al film thickness from 10 to 100 nm.

Optical measurements of the air-metal interfaces are shown in Fig. 5.8. The structured surfaces still show very different behaviour than the planar films. However, the air-metal interfaces show an increase in reflectance as function of metal thickness. This results in a trade-off between reflectance and transmittance, resulting in an optimum in absorbance for films of 40-60 nm thickness, for structures of type A, B, and C.

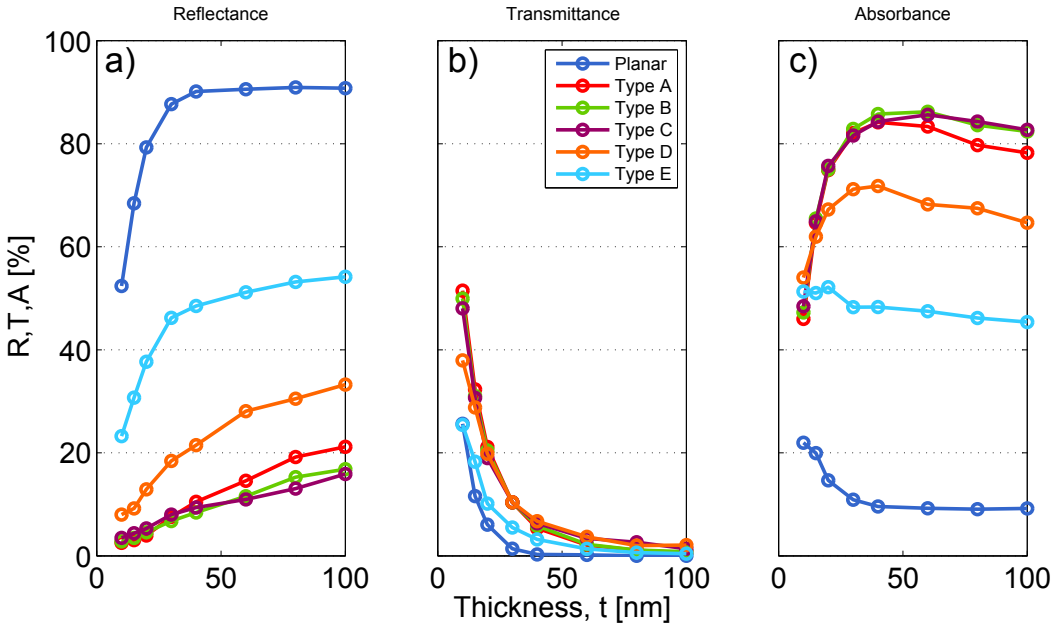

Figure 5.8: Optical measurements of the air-metal interface, for different structures and metal thickness at 500 nm wavelength. a) Total reflectance as function of metal thickness. b) Measured transmittance. c) Calculated absorbance.

5.3.3 Structure polarity and deposition method

The influence of deposition method, and polarity of the nanostructures was tested. Ormocomp samples with structures of the same polarity as on the BSi master were fabricated using a double UV-NIL Ormocomp process, as described in Sec. 3.4. These samples are denoted as having polarity X. Structures with the inverse polarity (polarity Y) were fabricated from the BSi master, using a single replication process. All the samples discussed in this section were type B nanostructures.

Three different metal deposition methods were used: e-beam evaporation, which was discussed previously, thermal deposition (Wordentec QCL 800), and sputter deposition. The latter was done commercially by Axxicon[123], with the scope of testing whether the black metal films could be produced using scalable fabrication methods.

Thermal deposition is, like e-beam evaporation, characterized by being highly directional, and is performed at high vacuum. As a result, both methods have poor step coverage. Sputter deposition is performed at low vacuum, and is less directional, resulting in a better step coverage.
The optical properties of 5 different samples were characterized. Both polarities were tested using e-beam evaporation, and sputter deposition, while thermal deposition was only tested on a Y-polarity sample.

Figure 5.9 (a-c) shows the optical properties of the fabricated samples, comparing the reflectance of the Ormocomp-metal, and air-metal interfaces, and the transmittance. The Ormocomp-metal interface shows very similar reflectance for all samples, although the samples fabricated by sputter deposition shows slightly higher reflectance. For the air-metal interface, the results were very different. The pol. X, sputter deposition sample shows the lowest reflectance of around 5%, while the pol. Y sputter deposition sample shows the highest reflectance of around 15%.

Also the transmission properties vary significantly depending on polarity and deposition method. The pol. X, sputter deposition samples has the largest transmittance, of 10-12%, while the pol. X, e-beam deposition sample is practically opaque.

The results suggest that the geometry of the surface, as well as the deposition method, influence the morphology of the deposited metal films. This change in morphology influences the optical properties, but mainly for the air-metal interface, and the transmission properties. Figure 5.9 (d) shows profile SEM images of the 5 different samples. It is seen that the sputter deposition results in a smooth Al layer over the structures. The e-beam and thermal deposition methods form metal clusters due to the highly directional deposition. The results show that despite the differences between the deposition methods, it is indeed feasible to fabricate the black metal films using commercial deposition methods like sputter deposition.

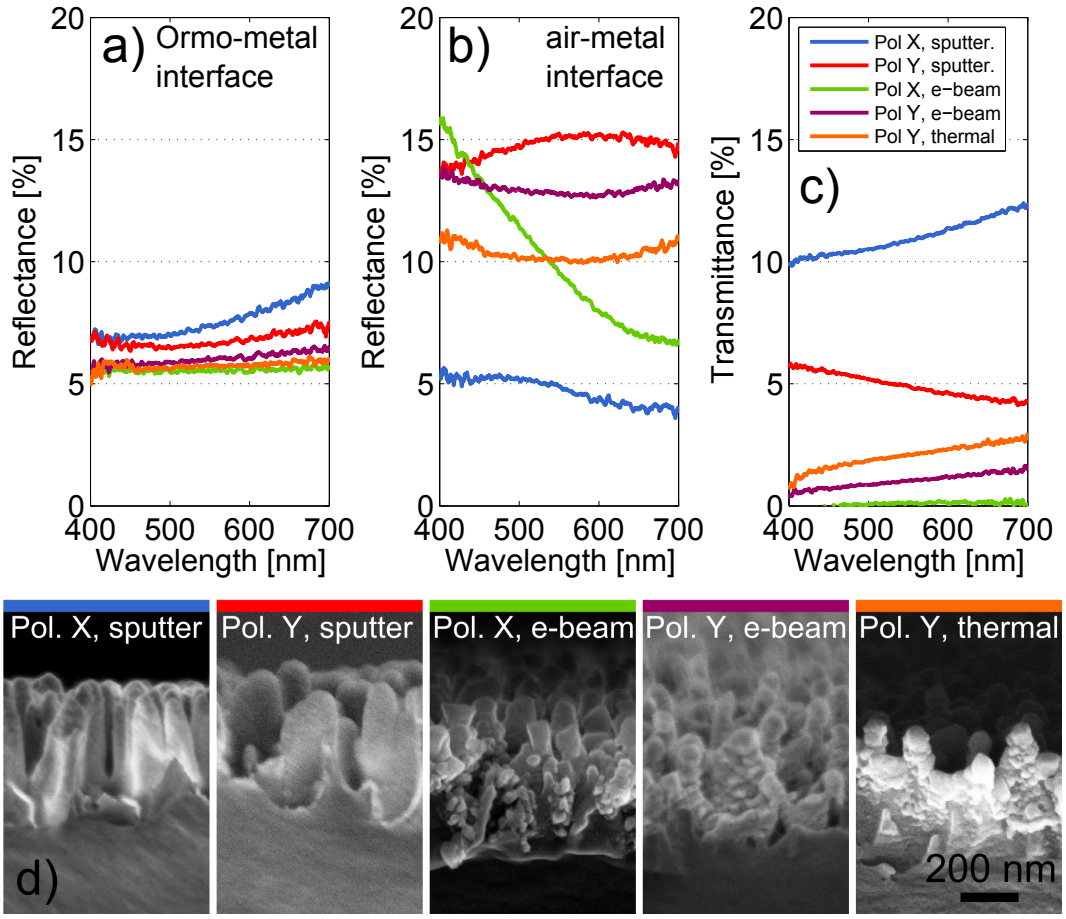

Figure 5.9: Effect of structure polarity and deposition method, for type B nanostructures. a) Reflectance of the air-metal interfaces b) Transmittance. c) Reflectance of the Ormocomp-metal interface. d) Scanning electron micrographs of the three structures with a 100 nm Al thin film.

5.3.4 NSOM measurements

As discussed in Sec. 2.7.2, and by Vorobyev *et al.*[31], the structured surfaces could possibly allow the incoming light to couple to plasmonic modes in the metal surface. In order to investigate if surface plasmons are excited in the metal films, a measurement was made using a near-field scanning optical microscope (NSOM). The measurement was made by Ph.D. student Jeppe S. Clausen from DTU Fotonik, during a visit in the NanoOpto group of Professor Uriel Levy, at the Hebrew University of Jerusalem, with assistance of Dr. Hesham Taha from Nanonics[124].

The measurements were made using an Optometronic 4000 dual probe NSOM system[124], at Nanonics. The NSOM was an aperture operation system, using apertures for both excitation and collection. Both probes were metal coated optical fibers that were placed in close contact to the surface. The excitation fiber had a 100 nm aperture, and the collector an aperture of 200 nm. A laser with a wavelength of 532 nm was used for the measurement. During operation, the exciting fiber was held in a fixed position on the surface, while the collecting fiber was scanned over the surface. Both probes were controlled in tapping mode (or shear force feedback mode). The collecting probe works as a standard AFM probe, as well as an NSOM probe. Thus, two images are recorded at the same time; topographic data and the NSOM signal.

The sample which was investigated was a type A, polarity Y Ormocomp structure, with a 20 nm thick Al film, deposited by e-beam evaporation. As the probes are slightly larger than the nanostructures on the surface, the topographical image must be expected to be significantly convoluted by the probe. This also entails that the NSOM probe will be in close contact to the metal film at the apex of the nanostructures, but will not make close contact to the metal film in the valleys between the structures.

The measurements works by placing the probe in close contact to the surface, at a distance smaller than the wavelength of the light. In the near field region, evanescent waves can couple to surface plasmon polariton (SPP) modes in the surface, as discussed in Sec. 2.7.2. The SPPs will propagate in the metal film. When the collecting probe is placed in contact to the surface, the evanescent field of the SPP, can couple to modes in the fiber, which are then detected.

The topographical AFM image and the simultaneously recorded NSOM signal is shown in Fig. 5.10 (a) and (b) respectively. The exciting probe is placed at the bottom of the image. The NSOM image suggests that surface plasmon polaritons are excited in the metal film. By azimuthal averaging of the NSOM signal around the exciting probe, shows an exponentially decaying signal, as function of distance to the exciting probe, as shown in Fig. 5.10 (c). The propagation constant of the SPP can be calculated as the distance at which the signal has decayed to e^{-1} of the initial signal, and is measured to be roughly 500 nm.

The NSOM signal shows an increase at the apexes of the nanostructures. However, as discussed above, it is not clear if this is due to the varying distance between the probe and the metal surface, or if it could be due concentrations of the electromagnetic fields.

Although the coupling mechanism in the NSOM mechanism is different from that which can happen in free space, the results do indicate that if SPPs are excited on the surface, they will have a propagation length of around 500 nm. The theoretical propagation length of

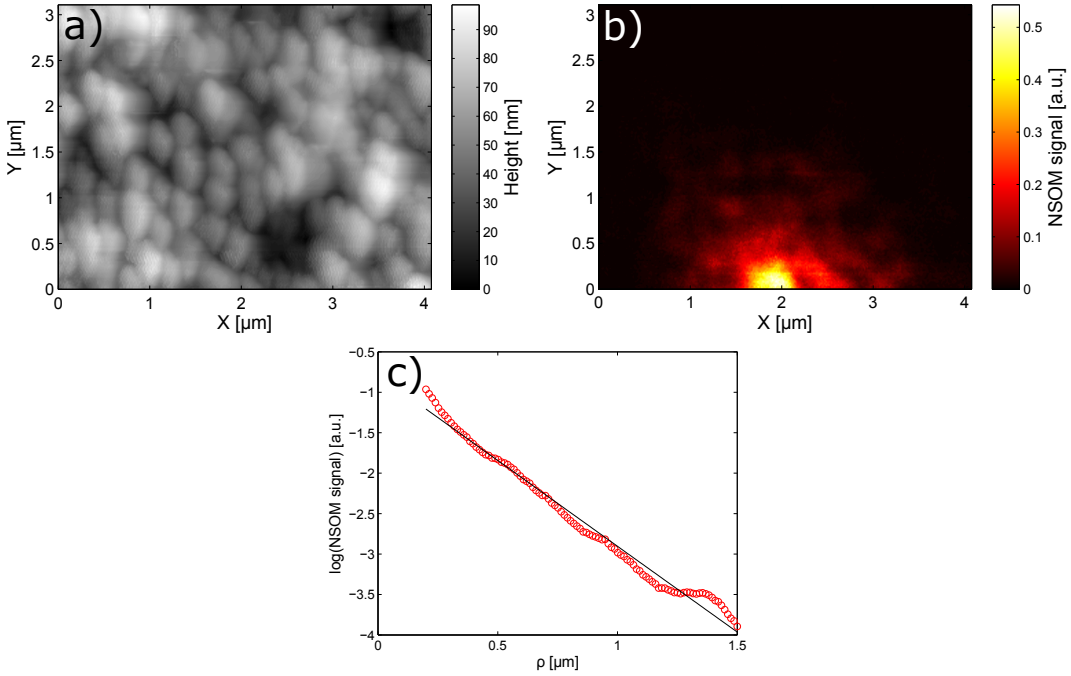

Figure 5.10: NSOM measurements. a) AFM image of type A Ormocomp surface with 20 nm Al. b) NSOM signal from surface in (a). c) Plot of NSOM signal after azimuthal averaging around the excitation probe. The result indicates that surface plasmon polaritons can be excited in the nanostructured Al film, which have a propagation length of around 500 nm.

an infinite, planar Al film can be calculated as discussed in the book by Maier, in chapter 2.3 [60]. For a 20 nm thick film, SPPs on either face of the film can couple, which allows for the existence of two modes: a symmetric and an asymmetric mode. For a 20 nm Al film surrounded by a medium with refractive index $n = 1$ on one side, and $n = 1.5$ on the other side, the SPPs will have propagation lengths of 2.1 µm and 11.2 µm for the symmetrical (in the electric field), and asymmetrical mode respectively. Although the investigated nanostructured surface is vastly different from a planar film, the measured propagation length has a reasonable value. It would be expected that the propagation length is shorter in the nanostructured film, as the structures are likely to increases losses, e.g. by coupling to free space. The preliminary results presented in this section indicate that NSOM measurements could prove a valuable tool in order to characterize the plasmonic properties of the surface.

5.3.5 Metal films on anodized porous alumina substrates

A 20 nm Al film was deposited on APA nanostructures, in order to compare the optical effect to that obtained by BSi nanostructures.

A 1 μm Al film was deposited on a boron doped Si substrate (resistivity < 0.025 Ω cm) using e-beam evaporation. The Al film was anodized at Centro Ricerche Fiat[125] (CRF), a partner in the Plast4Future project. The thickness of the resulting APA layer was measured from the profile SEM image shown in Fig. 5.11 (a), and was around 435 ± 25 nm. The characteristic length scale of the pores was 200 ± 15 nm (calculated using the Fourier method described in Sec. 3.2). 20 nm of Al was deposited on the APA structures using e-beam evaporation. Figure 5.11 (a-b) shows side views of the structures, before and after evaporation of Al. It is seen that the Al deposits partly at the top of the structures, partly at the bottom, on the Si substrate. The SEM images in Fig. 5.11 (a-b) were reconstructed from several images recorded with different contrast settings, due to large variations in contrast over the area. Fig. 5.11 (c) shows a top view image of the APA structure.

Figure 5.11 (d) shows the measured reflectance of the Si, APA on Si, and 20 nm Al on APA. It is seen that the APA layer slightly reduces the reflectance of the Si surface. After depositing 20 nm of Al on the APA, the reflectance of the surface decreases significantly. The reflectance of the Al film on APA structures, is larger than that of the tapered BSi structures, which show flat reflectance spectra of around 5% for the air-metal interface, for 20 nm Al films. The reflectance here also shows strong variation throughout the visible spectrum, resulting in a green colour, suggesting that there is an interference effect due to the 435 nm APA layer (the extremes of the reflectance matches those of APA on Si). Although this optical system includes a Si substrate, and is therefore very different to the dielectric Ormocomp substrates discussed previously, the results still indicate that the APA structures show different behaviour to the gradient BSi structures.

It was attempted to make an Ormocomp replica of the APA structures, by FDTS coating the APA surface using molecular vapour deposition (MVD), and casting Ormocomp from the surface, as described in Sec. 3.4. However, during demoulding the APA structures detached from the Si substrate, due to too low adhesion to the Si substrate, and remained embedded in the Ormocomp.

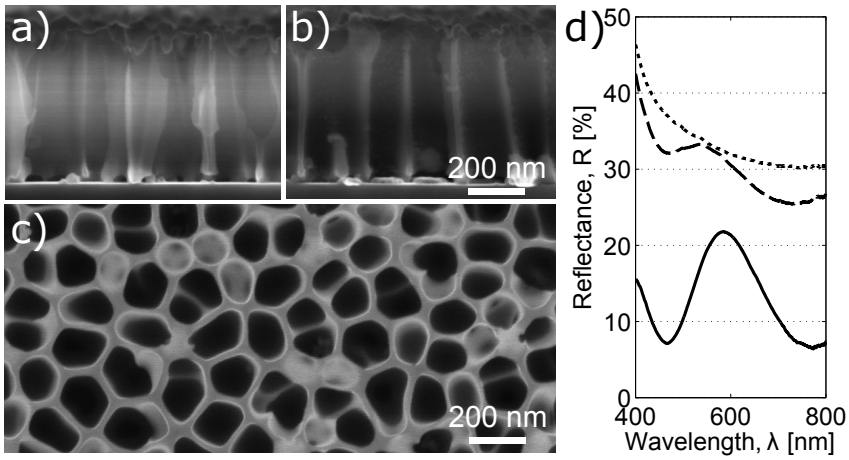

Figure 5.11: Properties of Al thin film on anodized porous alumina. a) SEM image of profile of APA layer on Si. b) SEM image of profile of 20 nm Al deposited on APA. c) SEM top view of APA layer on Si. d) Measured reflectance spectra of Si, APA on Si, and 20 nm Al on APA.

5.3.6 Structural decorations by combining micro- and nanostructures

In order to demonstrate the very different optical properties of nanostructured and rough metal films, a BSi master was powder blasted to remove the nanostructures, as described in Sec. 3.4.
The master was fabricated by RIE, forming type B nanostructures on the Si master. The structured surface was covered with blue tape, and the blue tape was patterned by using a CO_2 laser, forming a mask opening resembling a DTU logo. Using the remaining blue tape as a mask, the wafer was powder blasted using 60 µm beads. The powder blasting removed the nanostructures and formed a rough surface on the Si master. After being cleaned, the Si master was FDTS coated using MVD, and used to cast an Ormocomp replica. A photograph of the replica is shown in Fig. 5.12 (a). The nanostructured areas appear transparent, while the white, translucent area is due to scattering of light from the micro-rough surface, which was replicated from the powder blasted areas of the Si master. Figure 5.12 (b) shows the same sample, after a 100 nm Al film was deposited, using e-beam evaporation. The nanostructured areas now appear black, as discussed in the previous sections. The Al film on the rough surface, remains highly reflective, although light is diffusely scattered from the surface.
Figure 5.12 (c) shows the different length scales involved. At low magnification, the nanostructured surface of the letters “DTU” appears flat and shows a high brightness when imaged with SEM. At higher magnification the powder blasted rough surface is seen, surrounding the brighter letters. At very high magnification, one is able to distinguish the features of the nanostructured surface. The rough microstructured surface is seen as larger “craters”, showcasing the significant difference in the length scale between the two different structures.

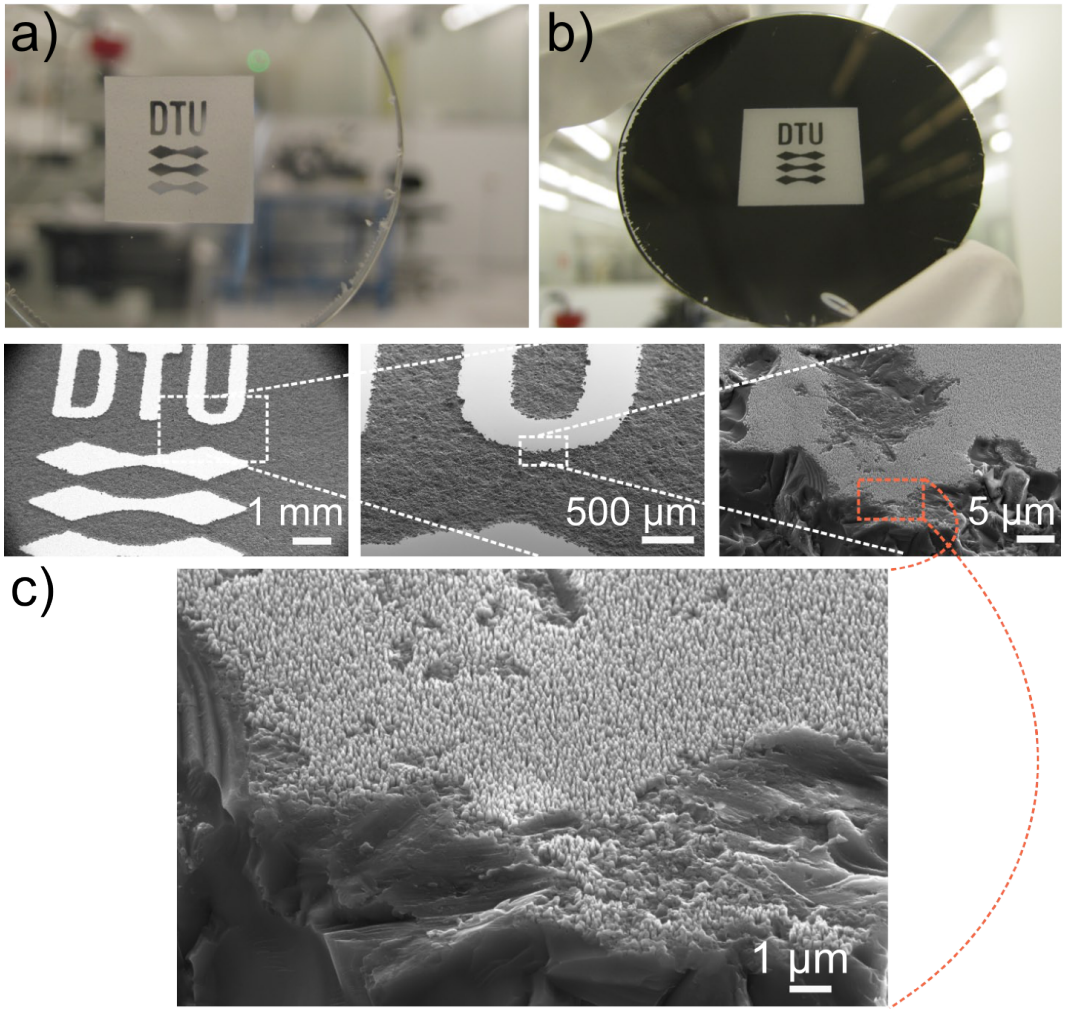

Figure 5.12: Nanostructured and micro-rough metal films. a) Photograph of Ormocomp sample, casted from powder blasted BSi master. b) Ormocomp sample after deposition of 100 nm Al. c) SEM images of the powder blasted and nanostructured areas of the Si master.

5.3.7 Increased absorbance of other materials

Different materials were deposited on type B, polarity Y Ormocomp substrates. The reflectance of the Ormocomp-metal interface of the planar, and nanostructured films is shown in Fig. 5.13. All the films have a thickness of 100 nm. The nanostructures significantly decrease the reflectance of all the materials: Al, Au, Ag, Cr, and Ge.
The nanostructured Ag film is significantly different from the other metals, in that it has a much larger reflectance. Although the planar Ag film has a higher reflectance than the other metals, the nanostructured Ag film appears to behave differently than the other metals.
The planar Cr film has the lowest reflectance of the investigated metals. As discussed by Cho *et al.*[41] the refractive index of Cr gives a rather low reflectance. The nanostructured Cr film also shows the lowest reflectance. The drawback of the intrinsically low reflectance of Cr is that the contrast between a nanostructured and reflecting film is less pronounced than for e.g. Al.
Figure 5.13 (c) shows photographs of the metal films deposited on type B nanostructures, taken from the Ormocomp-metal interface. The samples were fabricated using the powder blasted master discussed in Sec. 5.3.6. The difference between the logo and the rest of the sample thus shows the difference between an absorbing and a diffuse reflecting film.

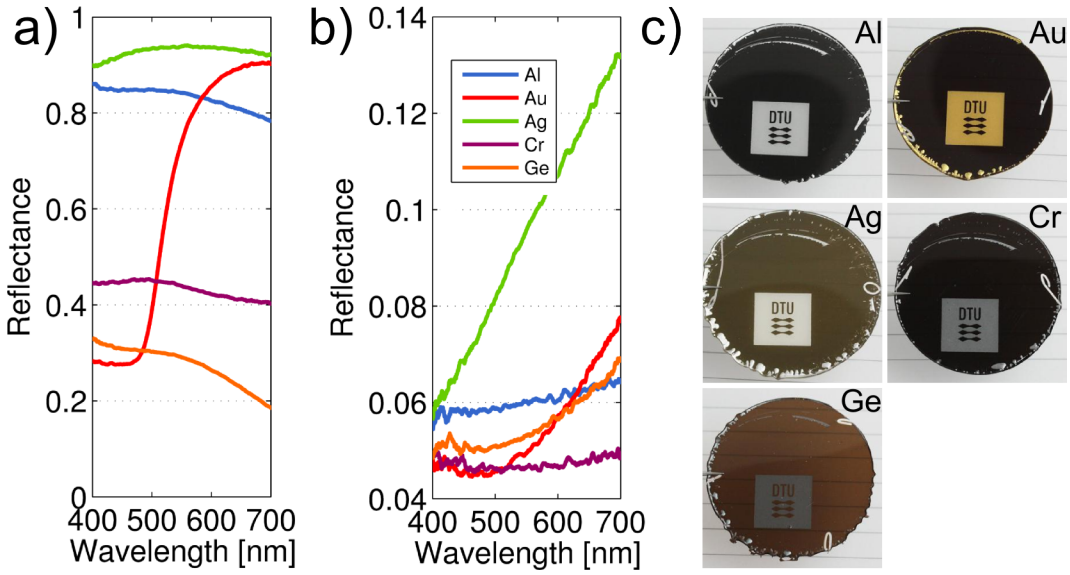

Figure 5.13: Reflectance spectra and photos of planar and nanostructured metals. Total reflectance of planar films (a) and type B, polarity Y nanostructured films (b). The reflectance was measured from Ormocomp-metal side. (c) Photos of Ormocomp samples with Al, Au, Ag, Cr, and Ge deposited. The logo on each sample is where the Si master was powder blasted before the casting. The surface here is not nanostructured, but rather microstructured. The difference between the logo and the rest of the sample thus showcases the difference between an absorbing and a reflecting film.

5.4 Discussion

Here we will discuss the results of the preceding sections, in terms of the geometry of the structures, compared to the absorption effect, and the mechanism leading to lowered reflectance and increase absorbance of the metal films.

It was shown that the reflectance of a 100 nm thick Al film could be reduced from 80% to 6%, and the absorbance was increased from 20% to over 90%. For the Ormocomp-metal interface, the effect was very robust: tapered nanostructures with a height in the range 300-600 nm, and a characteristic inter-distance of 150-200 nm showed very similar results (structures of type A-C). The type D structures with a height of 800 nm and a period of around 230 nm showed slightly different behaviour than A-C, indicating that they are on the border of the optimum substrate geometry. The type E structures, while still lowering reflectance and increasing absorbance, showed significantly worse properties than type A-D structures.

Due to the random nature of the BSi process, it is difficult to pinpoint the exact geometrical criteria for the structures to work as a substrate for black metal films. However, comparing type D and E, the two structures have very similar heights and periods, while the E-type structures are less dense than the D-type, which is best seen in Fig. 5.2. It seems reasonable, that if the surface has regions that are almost planar, the optical properties will be more similar to that of a planar surface.

From this, a few design criteria can be set up. The structures should have a height in the range 300-600 nm, a characteristic length scale of 150-200 nm, and the structures should be closely packed. The APA structures discussed in Sec. 5.3.5 fulfil these geometrical criteria, yet do not show as good an effect as the BSi structures. This adds to the criteria, that the structures should be tapered. If we keep considering only the Ormocomp-metal interface, we have seen in Sec. 5.3.3 that as long as the above criteria are met, the polarity of the structures is not important.

Turning our attention towards the air-metal interface, the results were very different. While the reflectance of the air-metal interface of structured films was still significantly lowered compared to a planar film, the reflectance was seen to increase as the thickness of the metal films increased.

The different properties of the Ormocomp-metal and air-metal interfaces are exemplified in Fig. 5.14, which shows the reflectance of the two interfaces of the type B structures, as function of Al film thickness. For planar films, the reflectance of the Ormocomp-metal interface will be slightly lower than the air-metal interface, due to the different refractive indices of air and Ormocomp. This can e.g. be calculated using the complex Fresnel equation, Eq. 2.7.6. Furthermore, the measured reflectance of the Ormocomp-metal interface, includes the reflectance of the air-Ormocomp interface, which is roughly 4%. These differences however, do not explain the steady increase in reflectance seen for the air-Ormocomp interface, as the metal layer thickness increases.

Inverting the polarity of the structures does not significantly influence the reflectance for the Ormocomp-metal interfaces, which infers that the different behaviour of the air-metal interface is not due to the different polarity of the structures. It must therefore be due to

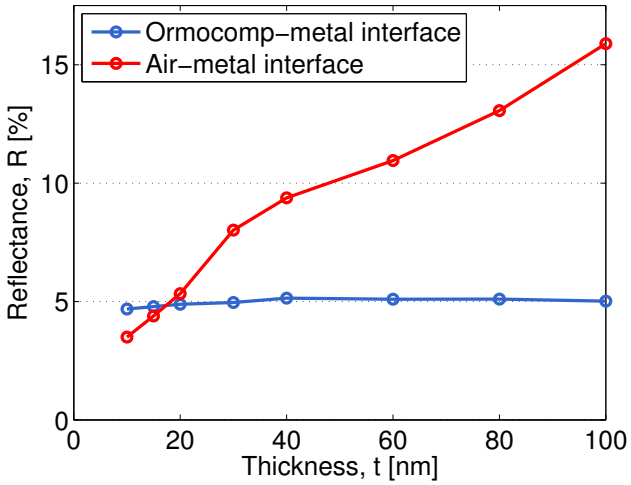

Figure 5.14: Reflectance of the Ormocomp-metal, and air-metal interfaces, of type B, polarity Y structures, as function of Al film thickness.

morphological changes in the metal film surface, as the thickness of the deposited layer increases. While for the Ormocomp-metal interface, the morphology does not change during deposition, the air-metal interface is subject to changes in the upper surface due to the deposition method.

E-beam evaporation is characterized by being very directional, due to the low vacuum during deposition, and the relatively large distance from the target to the substrate. This gives low step coverage. Due to the tall structures, metal that deposits on the apex of the structures can shadow the valleys on the surface. This can lead to formation of metal clusters at the apex of the structures, with less metal being deposited at the bottom. This can cause a flattening of the metal layer, which does not occur on the Ormocomp-metal interface.

Vorobyev *et al.* showed blackening of metals from laser ablation, and discussed four different mechanisms that can increase the absorbance of the structured metal film. These are: a gradient effect, plasmonic coupling to metal particles, plasmonic coupling to fractal like structures, and light trapping due to microstructures. Comparing the discussion of Vorobyev *et al.* to the results presented here, it can be conclude that the trapping effect can be ruled out for the structures presented here, as there are no microstructures present. The gradient effect is present for the BSi structures, and the results from APA indicate that a gradient in the volume fraction of the structures is indeed important.
Plasmonic coupling on the nanostructured surfaces, could indeed play a role in increasing the absorbance of the thin films. Results from NSOM measurements also indicate that SPPs can be excited in the surface, and have a decay length of around 500 nm.

Finally, our results shows that transmittance through the metal films is increased due to the nanostructures, similar to what is observed by Ting *et al.* [43]. The increased transmittance could be due to the lowered reflectance, or the fact that the metal film covers a larger area, due to the nanostructures.

6

Patent

6.1 Introduction

The patent application was filed September 2nd, 2013 at the European patent office, and was made public at the danish patent office (Patent- og Varemærkestyrelsen), November 12th, 2013.
Below follows the patent application in its full length. The figures follow at the end of the application.

6.2 A nanostructured surface for grey scale colouring

6.2.1 Abstract

The invention relates to a nanostructured product with a structurally coloured surface. The structurally coloured surface is obtained by providing a nanostructured surface on a substrate which may be a plastic material, and by providing a covering metal layer on the nanostructured surface. The metal layer generates broad band absorbance of light in a visible spectral range so that the structurally coloured surface appears dark, e.g. appears to have a grey or black colour. [Fig. 1 for publication]

6.2.2 Field of the invention

The invention relates to nanostructured surfaces, specifically to structural colouring by use of such surfaces.

6.2.3 Background of the invention

It is known to decorate plastic objects by painting with a coloured painting material. The painting will adhere to the object after it has dried. Other methods for providing plastic objects with a coloured decoration exist. Normally such methods complicate the manufacturing process of the plastic objects since the process in addition to forming the plastic object includes various steps for applying the decoration.

Furthermore, painted products may complicate recycling of such products since the paint has to be removed before recycling the main object since the paint may otherwise add undesired colouring to the recycling material, e.g. a white colour of a main material will be

polluted by black paint.

Accordingly, there is a need for other colouring processes for decorating objects which may not suffer from the above problems or which offer other advantages.

WO2013039454 discloses an optical arrangement which includes a substrate, and a plurality of spaced apart elongate nanostructures extending from a surface of the substrate, wherein each elongate nanostructure includes a metal layer on the end distal from the surface of the substrate. The present invention also relates to a method of forming the optical arrangement.

6.2.4 Summary of the invention

It would be advantageous to achieve improvements within methods for decorating metal or polymer objects. In particular, it may be seen as an object of the present invention to provide a method that solves the above mentioned problems relating to colouring and/or recycling, or other problems, of the prior art. To better address one or more of these concerns, in a first aspect of the invention a nanostructured product with a structurally coloured surface is presented that comprises -a substrate comprising a nanostructured surface, comprising raised or depressed nanostructures, and -a metal layer at least partially covering the nanostructured surface and at least partially conforming to the nanostructured surface so that the metal layer generates broad band absorbance of light in a visible spectral range.

For example a plastic object such as a toy may comprise the nanostructured product according to the first aspect. The plastic object and the substrate may be made of different materials or of the same material so that only a metal layer need to be added to the object in order to decorate the object with a colouring, here a dark, e.g. grey or black colour. Since only a thin metal layer, but no additional colours, is introduced in the object or substrate to create the desired colouring the object may be recycled many times, e.g. a hundred times or more, without destroying the original colour of the object or substrate.

The metal layer generates absorption in a spectral range of the visible spectral range, i.e. in a range, which covers at least 100 nanometre of the visible range from 380 to 700 nanometre. In practice, the metal layer should generate absorption over the entire or substantially the entire visible range in order to generate broad band absorption.

The nanostructured surface normally covers an area larger than e.g. at least 4 square millimetres. Thus, over a relatively large area, e.g. at least 4 square millimetres the nanostructured surface has the same or substantially the same optical properties with respect to absorption.

The nanostructured colouring may be provided to opaque or transparent substrates. In an embodiment the substrate is a plastic or polymer. In an alternative embodiment the substrate is an oxide layer on a metal. In an embodiment the average broad band absorption of light in a visible spectral range is greater than 20 percent in average over the visible spectral range. Absorption of 20 percent of the power of incident light on the substrate may be sufficient to generate a dark surface.

In an embodiment the metal layer on the nanostructured surface has a reflectance of light in a visible spectral range which is less than 20 percent in average over the visible spectral range. Reflection of less than 20 percent of the power of incident light on the substrate

improves the darkness of the nanostructured surface.

Preferably, the metal layer conforms to the nanostructured surface so that the metal layer comprises a nanostructured surface comprising raised or depressed structures similar to the nanostructured surface of the substrate.

In an embodiment the raised or depressed nanostructures of the substrate projects from a base plane, so that the raised or depressed nanostructures of the conforming metal layer also projects from a base plane of the metal layer, wherein the coverage of the raised or depressed structures of the metal layer relative to the base plane of the metal layer is greater than 30 percent.

In an embodiment the substrate further comprises a scattering surface. The scattering surface may comprise structures having dimensions which are large enough to scatter incoming visible light.

The scattering surface may be located adjacent to nanostructured surface so as to provide a contrast to the dark nanostructured surface.

The substrate may comprise a plurality of the scattering surfaces and a plurality of the nanostructured surfaces arranged in a pattern with alternating scattering surfaces and nanostructured surfaces. Such a pattern may be used for creating a particular level of grey.

In an embodiment the substrate further comprises a non-structured surface covered by the metal layer. The non-structured surface may be used for generating a reflective surface, e.g. adjacent to the nanostructured dark surface.

In an embodiment the substrate is a foil, wherein the metal layer is located on a back face of the foil, and wherein the back face is configured to be connected to an object.

In an embodiment the metal layer is covered with a protective transparent layer. Such a protective layer may advantageously be used for protecting the nanostructures in the substrate and the metal layer.

A second aspect of the invention relates to a process for manufacturing the nanostructured product according to the first aspect, comprising -forming a plastic object by moulding or embossing by use of a mould or embossing tool, wherein a surface of the mould or embossing tool is provided with a nanostructured surface, so that the forming creates a nanostructured surface of the plastic object, -covering the nanostructured surface of the plastic object with a metal layer so that the metal layer at least partially covers the nanostructured surface and at least partially conforms to the nanostructured surface so that the metal layer generates broad band absorption of light in a visible spectral range.

In summary the invention relates to a nanostructured product with a structurally coloured surface. The structurally coloured surface is obtained by providing a nanostructured surface on a substrate which may be a plastic material, and by providing a covering metal layer on the nanostructured surface. The metal layer generates broad band absorbance of light in a visible spectral range so that the structurally coloured surface appears dark, e.g. appears to have a grey or black colour.

In general the various aspects of the invention may be combined and coupled in any way possible within the scope of the invention. These and other aspects, features and/or advantages of the invention will be apparent from and elucidated with reference to the embodiments described hereinafter.

6.2.5 Brief description of the drawings

Embodiments of the invention will be described, by way of example only, with reference to the drawings, in which

Fig. 1 illustrates the nanostructures 103 in nanostructured product 100, Fig. 2 shows measured nanostructured surfaces 102 and metal layers 105,
Fig. 3A illustrates cross-sectional views of different principal shapes of raised nanostructures 103,
Fig. 3B illustrates top views of the cross-sectional views from Fig. 3A for point-like structures 321 and elongate structures 322,
Figs. 4A-C show experimentally obtained absorbance values 401 and reflectance values 402, and
Fig. 5 shows an alternative embodiment of the nanostructured surface 102, wherein the nanostructures are arranged in a binary pattern.

6.2.6 Description of an embodiment

Fig. 1 principally illustrates a nanostructured product 100 with a structurally coloured surface. The product 100 includes a substrate 101 which includes a nanostructured surface 102 having raised or depressed nanostructures 103. The nanostructures 103 may be seen as elongate structures, e.g. pins or holes, protruding out from or into the substrate. The nanostructured surface defines a base plane 104, which may be a generally flat surface or a curved surface, which the nanostructures 103 projects into or out from.

Structural colouring refers to colouring caused by optical effects due to the nanostructures instead of colouring caused by coloured pigments.

The nanostructured surface 102 is provided with a metal layer 105 which at least partially covers the nanostructured surface and at least partially conforms to the nanostructured surface. A metal layer normally absorbs a small amount of the light energy and reflects or scatters a relatively large amount of the light energy. However, when the metal layer 105 is nanostructured according to embodiments herein the absorbance of light increases significantly and the reflectance also decreases significantly so that the metal layer 105 will appear dark. According to embodiments of the invention the nanostructured surface 102 is configured primarily to increase absorbance in the visible spectral range, i.e. in the spectral range from 300 – 700 nm.

Generally, the nanostructured product 100 may be a film, a foil, a part of an end-product or an end-product. Specific examples of a nanostructured product 100 comprise interior parts for cars, toys, household appliances, etc. For example, a surface of an interior part for cars may be provided with structurally coloured decorations, and a toy may be provided with a

decoration by forming a nanostructured surface 102 in surface of the toy.

The substrate may be a polymer, a glass material, an oxide layer (e.g. anodized alumina) or other dielectric material that could be nanostructured. Any metal or other electrically conducting material which can be nanostructured may also be used as the substrate – but in this case the metal layer 105 on the nanostructured electrically conducting surface is not required.. Accordingly, the entire product 100 may be made from the same substrate material where only a thin metal layer 105 is provided and possibly a transparent protective layer. Thus, it may be possible to decorate a product 100 with graphics or text by use of structural colours without a need to print a decoration on the object using pigmented paint. The substrate 101 may be opaque, transparent or semi-transparent.

The product 100 may be formed by moulding, e.g. injection moulding, by use of a mould, wherein a surface of the mould is provided with a nanostructured surface, so that the moulding creates the nanostructured surface 102 of the plastic object. Alternatively, the product 100 may be formed by hot embossing where an embossing tool is provided with a nanostructured surface so that the embossing creates the nanostructured surface 102 of the plastic object. The process for manufacturing the product 100 further comprises covering the nanostructured surface of the plastic object with a metal layer so that the metal layer at least partially covers the nanostructured surface and at least partially conforms to the nanostructured surface so that the metal layer generates broad band absorption of light in a visible spectral range.

The mould or embossing tool may be made using electroplating to make a metal mould from a silicon master or other master. Typically nickel or an alloy hereof is used in the electroplating process to apply a metal layer (e.g. 200 micrometre thick) on the nanostructured silicon master so that a metal layer with a negative pattern of the positive pattern on the silicon master is formed. In an embodiment the master is anodized aluminium where the oxide layer contains the nanostructures 103, or contains black silicon or nano-grass structures.

The process of covering the nanostructured surface of the plastic object with a metal layer may be performed using physical vapour deposition (PVD), e.g. electron beam PVD wherein an electron beam is used to evaporate the metal from solid/liquid phase to gas phase. The gas condenses as a thin film on the nanostructured surface and forms the metal surface 105. Alternatively, the process of covering the nanostructured surface of the plastic object with a metal layer may be performed using sputtering, which may be particularly useful in industrial processes.

In case the substrate 101 is a metal or other electrically conducting material the nanostructured surface 102 is provided in the substrate but without an additional metal layer 105. For example the product 100 may be a metal foil wherein the nanostructured surface 102 is provided, e.g. embossed directly into the metal foil.

Fig. 2 shows examples of nanostructured surfaces 102 with protruding elongate structures covered with a metal layer 105. The cross sectional views in Fig. 2 are obtained by scanning electron microscopy. The thicknesses of the metal layers 105 in the upper, middle and bottom figures are 40, 60 and 100 nanometre, respectively. A 200 nm scale is shown.

Fig. 2 shows that that the metal layer may not fully conform to the nanostructured surface

since the metal may have difficulties in covering narrow valley structures of the nanostructured surface 102 and since metal may have difficulties in covering narrow peak structures of the nanostructured surface 102. Similarly, there may be holes in the metal layer 105 so that some parts of the nanostructured surface 102 is not fully covered with the metal layer. Despite of these issues, it is true that the metal layer at least partially covers the nanostructured and conforms to the nanostructured surface so that the metal layer comprises a nanostructured surface comprising raised or depressed structures corresponding to the raised or depressed structures of the substrate 101, and so that the conforming nanostructured layer exhibits increased absorbance and decrease reflectance relative to metal surfaces that are not nanostructured.

Fig. 2 shows an embodiment of the invention wherein the nanostructures 103 are arranged in a random or at least non-periodic pattern. For example, the randomly arranged nanostructures 103 may be fabricated using methods corresponding to know methods for manufacturing black silicon, also known as nano grass. Other suitable methods includes KOH (potassium hydroxide) wet etching and plasma etching of polymer.

In an embodiment the randomly arranged nanostructures 103 are present in an oxide layer. The oxide layer is present on a metal such as aluminium, titanium, zinc, magnesium or other metal and the oxide layer is obtained by anodizing the metal. The dielectric oxide layer obtained by anodizing has a porous nanostructured surface 102. The metal layer 105 can be a provided on the oxide layer to create e.g. dark or black structures on the oxide layer.

In order to achieve a low reflectance the raised or depressed structures 103 should be packed as densely as possible so that the area of a generally flat surface of the base plane 104 is as small as possible. That is, a generally flat surface will have a relatively high reflectance which may be undesired. In an embodiment the coverage of the raised or depressed structures 103 of the metal layer 105 relative to the base plane of the metal layer is greater than at least 30 percent, but preferably greater than 90 percent. A high coverage, e.g. above 90 percent, is possible when the nanostructures have a tapered shape such as the triangular shaped structures shown in Fig. 3A. A lower coverage of about 50 percent may be feasible when the nanostructures have pillar-like shapes. In general the high coverage of at least about 90 percent applies for tapered periodically or non-periodically nanostructures, whereas a lower coverage less than about 60 percent applies for periodically or non-periodically nanostructures having steep edges like pillar-shaped structures. See Fig. 5 for an embodiment with periodically located nanostructures 103.

Fig. 3A illustrates cross-sectional views of different principal shapes of raised nanostructures 103. Similar depressed nanostructures can be made by forming structures into a substrate 101. The triangular-shaped cross-sectional views in the upper drawing may be obtained by e.g. pyramid-shaped protruding features, the sinusoidal-shaped cross-sectional views in the middle drawing may be obtained by e.g. 3D-parabolic-shaped protruding features, and the rectangular-shaped cross-sectional views in the bottom drawing may be obtained by e.g. protruding cylinders or other pillar-shaped structures. The nanostructures 103 are formed on a plane or curved surface of a substrate 101.

Fig. 3A shows the width 301 and height 302 of the nanostructures and the spacing 303 between nanostructures. For nanostructures of the type shown in the upper and middle drawing the spacing 303 between nanostructures 103 is close to zero, at least at some lo-

cations of neighbour nanostructures and depending on the 3Dshape of the structures. For the nanostructures of the type shown in the upper and middle drawing the period of the nanostructures 103 is the same or substantially the same as the width 301, whereas, for the nanostructures with a spacing 303 between neighbour structures the period is the sum of the width 301 and the spacing 303.

The width 301 may be in the range from 10 to 2000 nm. The absorbance effect seems to be most efficient for widths 301 below 300 nm, although absorbance effects are also present above 300 nm and up to 1 micrometre. Above 1 micrometre the absorbance effect becomes smaller. Widths above e.g. 200 nm, e.g. in the range from 250-750 nm may be preferred due the higher mechanical robustness of compared to smaller widths. The width may be the diameter of a structure 103, a maximum, a minimum or an average width of a protruding or recessed structural feature 103.

The period of the nanostructures may be in the range from 10 to 2000 nm. For periods above 150 nm diffraction effects start to take place for periodically arranged nanostructures. Since some diffraction may be acceptable periods above 150 nm may be acceptable for periodic structures. For non-periodic or random structure diffraction effects are minimal.

The heights 302 may be in the range from 50 to 5000 nm. Heights in the range from 100 to 300 nanometres may be preferred for optimum absorption.

Fig. 3B illustrates top views of the cross-sectional views from Fig. 3A. Fig. 3B also shows the location of line AA of the cross-sectional views in Fig. 3A.

Fig. 3B shows that the nanostructures 103 may be point-like structures 321 having substantially the same extension 301 in two orthogonal planar directions. Alternatively or additionally, the nanostructures 103 may be elongate 322 structures having an extension in one planar direction which is at least twice the width 301. The elongate planar extension may be straight or curved and the length of the planar extension may range from e.g. 100 nm to several micrometre or even several millimetre.

Figs. 4A-C show experimentally obtained absorbance values 401 and reflectance values 402 (along the ordinate) for incident light at 500 nm as a function of the thickness of the metal layer (along the abscissa). The reflectance values 402 include both specular and scattered light from the surface of a metal layer 105. The data in Figs. 4A-C where obtained from non-periodically arranged nanostructures 103 wherein nanostructures 103 have a width of 100 nanometre and a height of 200 nanometre in the results in Fig. 4A, a width of 150 nanometre and a height of 300 nanometre in the results in Fig. 4B, a width of 250 nanometre and a height of 500 nanometre in the results in Fig. 4C. Thus, although the absorbance and reflectance curves 401, 402 depend on the dimension of the nanostructures, the curves in Figs. 4A-C show similar absorbance and reflectance curves from nanostructures with widths in the range 100-250 nanometre and heights in the range 200-500 nanometre. It is believed that similar or at least acceptable absorbance and reflectance values are obtainable from nanostructures with widths in the range 100-2500 nanometre and heights in the range 200-5000 nanometre. For the larger heights and widths, e.g. widths about 1000 nanometre, the ratio of heights and widths may be chosen so that scattering is minimised, e.g. by choosing heights that are approximately twice the widths.

In Figs. 4A-C, the reflectance and absorbance values are obtained for incident light at 500 nm. However, since the reflectance, absorbance and transmittance values substantially do not depend on wavelength in the visible range (300-700 nm), the data in Fig. 4 are also applicable for other wavelengths in the visible range so that the reflectance and absorbance values in Fig. 4 are applicable as average percentages over the visible range.

The curves 401, 402 in Fig. 4 suggest that the thickness of the metal layer is in the range from 10-80 nm, e.g. in the range from 20-50 nm in order to obtain absorbance values above 65 percent and reflectance values below maximum 20 percent in average over the visible spectral range. Such absorbance values may be sufficient for obtaining a surface which appears dark. If the reflectance becomes greater than 30-40 percent the surface will appear reflective and have a mirror-like appearance.

In practice an average broad band absorption of light in a visible spectral range of at least 20 percent in average over the visible spectral range may be sufficient for achieving a dark surface. Particularly, for opaque substrates a relatively low absorbance of 20 percent and a corresponding relatively high transmittance of the metal layer 105 (but still a low reflection of max. 20 percent) may be sufficient for achieving a dark surface since light has to traverse the metal layer 105 twice (i.e. light which is not absorbed in the first traversal of the metal layer and which is reflected at the interface between the metal layer 105 and the nanostructured surface 102 will have to traverse the metal layer 105 a second time and, therefore, be expose to absorption a second time).

The absorbance and reflectance values in Fig. 4 have been obtained with an aluminium layer 105. According to an embodiment, aluminium is preferred for the metal layer 105. Other metals like gold or silver are also applicable, but may be less preferred due to the higher cost of these materials compared to aluminium, which may be important particularly for high volume production using e.g. injection moulding.

The reflectance, absorbance and transmittance values referred to herein are defined as the ratio of incident power of light and reflected, absorbed or transmitted power of light.

By applying a pattern provided with the nanostructured surface 103 and metal layer 105 over a surface of a substrate 101 the product 100 obtains a structurally coloured decoration, e.g. text or other graphics, i.e. a coloured decoration which has a substantially monochrome dark appearance. The dark appearance may be black or grey depending on the absorbance of the nanostructured metal layer 105.

The product 100 may further be configured so that the substrate 101 comprises a scattering surface. As illustrated in Fig. 1 the scattering surface 110 may be embodied as a rough surface with scattering structures 111 having dimensions which are large enough to scatter incoming light. Such scattering structures may have dimensions, i.e. dimensions in the plane of substrate and perpendicular to the substrate, where dimensions in the plane of the substrate (e.g. a diameter of a protruding structure) is in the range from 1 micrometre to 1 millimetre and where dimensions perpendicular to the substrate (e.g. a height of a protruding structure is in the range from 100 nanometre to 200 micrometre. The scattering surface 110 may or may not be covered with a metal layer 105. Particularly if the surface of the substrate has good reflection properties, e.g. if the surface has a light colour, a metal layer 105 may not be required. However, if optimum scattering properties are sought or if

the substrate 101 is not suited for scattering, the scattering surface may be covered with the same metal layer 105 as the nanostructured surface 102.

The rough scattering surface of the substrate may be manufactured by sandblasting areas which should have a scattering effect.

The substrate 101 may exhibit good scattering features in itself in which case the surface need not be configured as a rough surface with scattering structures 111.

The scattering surface may be located adjacent to the nanostructured surface so that a high visual contrast is generated between the dark nanostructured surfaces 102 and the bright scattering surfaces.

In an embodiment the substrate 101 is configured with a plurality of scattering surfaces and a plurality of the nanostructured surfaces 102 arranged in a pattern with alternating scattering surfaces and nanostructured surfaces. The pattern of alternating dark and bright areas may be used for generating surfaces which appear brighter than the dark areas of the nanostructured surfaces 102 and darker than the bright areas of the scattering surfaces, i.e. for generating grey scale colours.

Alternatively or additionally, grey scale colours may be achieved by the geometry of the nanostructures, e.g. by forming nanostructures 103 having heights 302 or equivalent depths which are relatively low (e.g. compared to surrounding nanostructures 103 configured for generating darker surfaces) whereby the reflectance from such structures is increased so that the surface appears more grey.

Additionally or alternatively, the product 100 may further be configured with a specular reflective surface. The specular reflective surface may be embodied by the substrate 101 configured with a non-structured surface covered by the metal layer 105. Such non-structured surface covered by a metal layer will have a high reflectance and a mirror-like appearance. The specular reflective surface may be located adjacent to the nanostructured surface and/or the scattering surface so that a high visual contrast is generated between mirror-like surface and the dark nanostructured surfaces 102 and/or the bright scattering surfaces.

As shown in Fig. 1 the metal layer 105 covering the nanostructured surface 102 may be covered with a transparent protective layer 130. Additionally, other surfaces of the substrate 101 such as the specular reflective surface and/or the scattering surface may also be covered by a transparent protective layer 130. The transparent protective layer 130 may have a scattering effect, e.g. achieved by scattering structures such as scattering spheres/particles or irregularities included in the protective layer or on the surface of the protective layer. Alternatively or additionally, the scattering effect of the transparent protective layer 130 may be achieved using polymer materials which inherently have scattering properties.

The nanostructured product may be in the form of a film or foil configured to be connected to another object, e.g. via an adhesive layer. According to this example the film-substrate is embodied by the substrate 101. A metal layer 105 is provided on a front face of the film-substrate which is provided with the nanostructured surface 102. A back face of the film is configured, e.g. with an adhesive layer, for enabling connection to an object.

Alternatively the film product may be configured so that the metal layer is located on a back face of the foil, and so that the back face is configured to be connected to an object. According to this embodiment the film is transparent so that light is able to propagate through the film to the nanostructured metal surface 105. An adhesive layer may be provided on the back face and thereby on the nanostructured metal surface 105. Since the adhesive layer, which may be a glue or curable polymer, is soft the adhesive layer does not affect the structures of the nanostructured surface 102 significantly.

Fig. 5 illustrates (top view and side view) an embodiment of the nanostructured product 100 wherein the nanostructures 103 of the nanostructured surface 102 are arranged periodically with constant or substantially constant periods 501, 502 in two orthogonal planar directions.

The periodically arranged nanostructures 103 generally have a height in the range of 50-150 nanometre with a preferred height of 100 nanometre. The lateral size, e.g. diameter, of the periodically arranged nanostructures 103 is generally in the range of 10 to 350 nanometre, and the lateral spacing of the nanostructures 103, i.e. distance between neighbour nanostructures 103 along the directions of the periods 501, 502, is generally in the range from 20-400 nanometre. Ideally the period 501, 502 should be maximum 150 nanometre in order to avoid diffraction. However, since some diffraction may be allowed the period may also be greater than 150 nanometre.

The periodically arranged nanostructures 103 may be configured as raised or depressed nanostructures relative to the base plane 104 of the substrate 101. A metal layer 105 (implicitly indicated in Fig. 5) is applied to the nanostructured surface 102 so that the metal layer at least partially covers the nanostructured surface 102 and at least partially conforms to the nanostructured surface so that the metal layer generates broad band absorbance of light in a visible spectral range.

Fig. 5 shows that the nanostructures have a pillar-like shape with steep edges. For the periodically arranged nanostructures 103 having pillar-like shapes the filling factor, i.e. the coverage of the raised or depressed nanostructures of the conforming metal layer relative to the base plane 105 of the metal layer, is greater than 30 percent and preferably about 50 percent.

Instead of having pillar-like shapes, the periodically arranged nanostructures in Fig. 5 may have tapered shapes. In case the periodically arranged nanostructures have tapered shapes the filling factor may be greater than 90 percent.

Accordingly, the periodically arranged nanostructures may have any of the cross-sectional shapes of the non-periodically arranged nanostructures shown in Fig. 3A. Furthermore, the periodically arrange nanostructures may have point like shapes 321 or elongate shapes 322 as shown in Fig. 3B.

While the invention has been illustrated and described in detail in the drawings and foregoing description, such illustration and description are to be considered illustrative or exemplary and not restrictive; the invention is not limited to the disclosed embodiments. Other variations to the disclosed embodiments can be understood and effected by those skilled in the art in practicing the claimed invention, from a study of the drawings, the disclosure, and the appended claims. In the claims, the word "comprising" does not exclude other elements

or steps, and the indefinite article "a" or "an" does not exclude a plurality. The mere fact that certain measures are recited in mutually different dependent claims does not indicate that a combination of these measures cannot be used to advantage. Any reference signs in the claims should not be construed as limiting the scope.

6.2.7 Claims

1. A nanostructured product with a structurally coloured surface, comprising -a substrate comprising a nanostructured surface, comprising raised or depressed nanostructures, - a metal layer at least partially covering the nanostructured surface and at least partially conforming to the nanostructured surface so that the metal layer generates broad band absorbance of light in a visible spectral range.

2. A nanostructured product according to claim 1, wherein the substrate is opaque to visible light.

3. A nanostructured product according to any of the preceding claims, wherein the substrate is an oxide layer on a metal.

4. A nanostructured product according to any of the preceding claims, wherein the average broad band absorption of light in a visible spectral range is greater than 20 percent in average over the visible spectral range.

5. A nanostructured product according to any of the preceding claims, wherein the metal layer on the nanostructured surface has a reflectance of light in a visible spectral range which is less than 20 percent in average over the visible spectral range.

6. A nanostructured product according to any of the preceding claims, where the metal layer conforms to the nanostructured surface so that the metal layer comprises a nanostructured surface comprising raised or depressed structures.

7. A nanostructured product according to claim 6, wherein the raised or depressed nanostructures of the substrate projects from a base plane, so that the raised or depressed nanostructures of the conforming metal layer also projects from a base plane of the metal layer, and wherein the coverage of the raised or depressed structures of the metal layer relative to the base plane of the metal layer is greater than 30 percent.

8. A nanostructured product according to any of the preceding claims, wherein the substrate further comprises a scattering surface.

9. A nanostructured product according to claim 8, wherein the scattering surface comprises structures having dimensions which are large enough to scatter incoming visible light.

10. A nanostructured product according to any of claims 8-9, wherein the scattering surface is located adjacent to nanostructured surface.

11. A nanostructured product according to any of claims 8-10, wherein the substrate comprises a plurality of the scattering surfaces and a plurality the nanostructured surfaces arranged in a pattern with alternating scattering surfaces and nanostructured surfaces.

12. A nanostructured product according to any of the preceding claims, wherein the substrate further comprises a non-structured surface covered by the metal layer.

13. A nanostructured product according to any of the preceding claims, wherein the substrate is a foil, wherein the metal layer is located on a back face of the foil, and wherein the back face is configured to be connected to an object.

14. A nanostructured product according to any of the preceding claims, wherein the metal layer is covered with a protective transparent layer.

15. A process for manufacturing the nanostructured product according to claim 1, comprising -forming a plastic object by moulding or embossing by use of a mould or embossing tool, wherein a surface of the mould or embossing tool is provided with a nanostructured surface, so that the forming creates a nanostructured surface of the plastic object, -covering the nanostructured surface of the plastic object with a metal layer so that the metal layer at least partially covers the nanostructured surface and at least partially conforms to the nanostructured surface so that the metal layer generates broad band absorption of light in a visible spectral range.

1/5

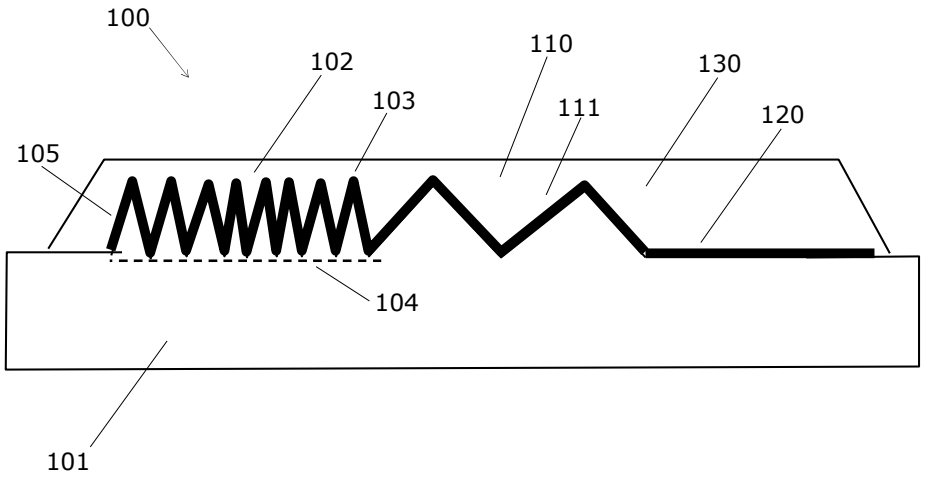

Fig. 1

2/5

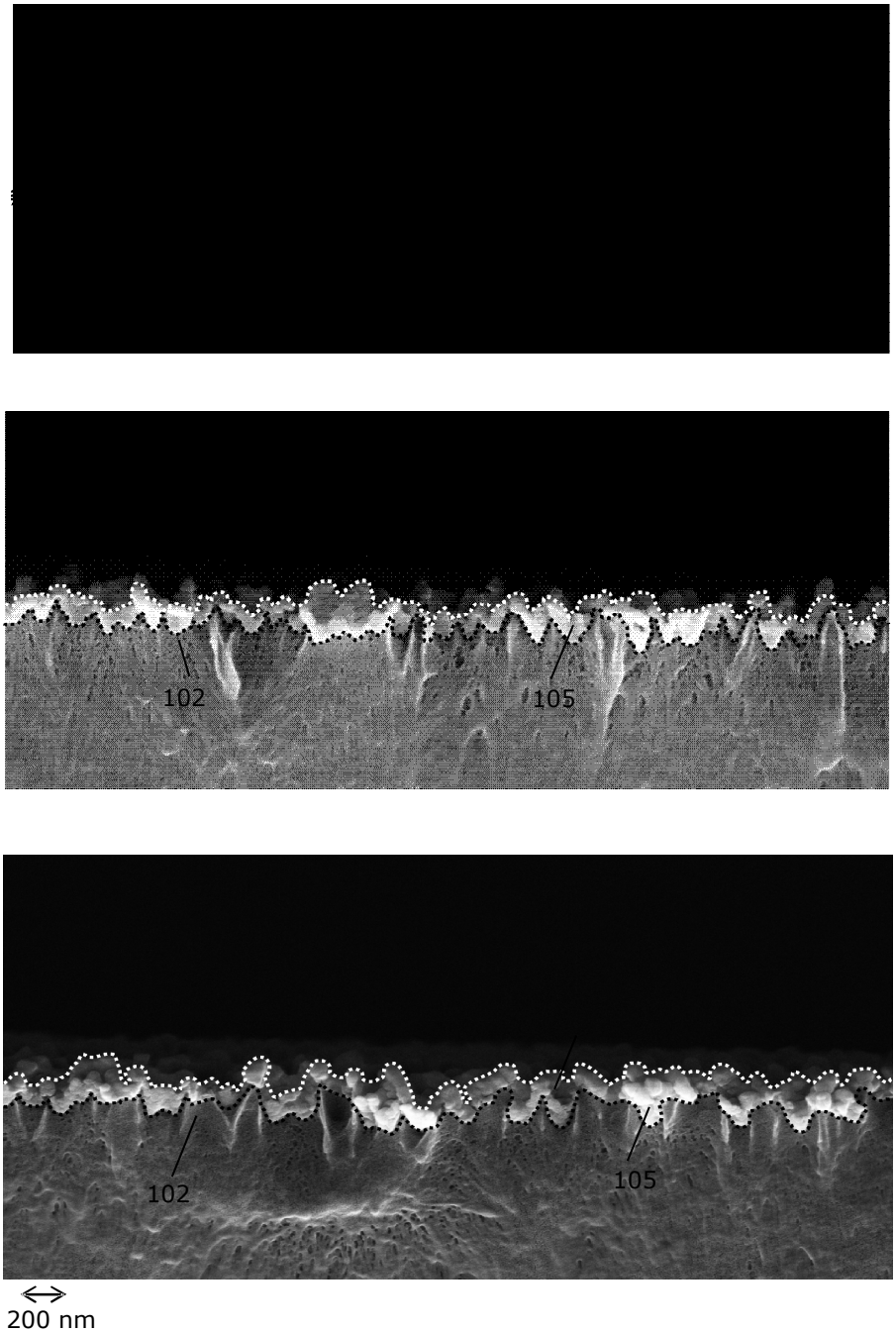

Fig. 2

3/5

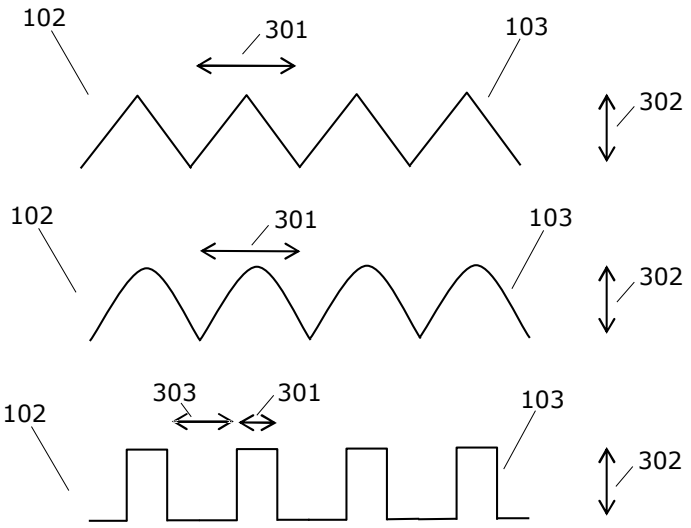

Fig. 3A

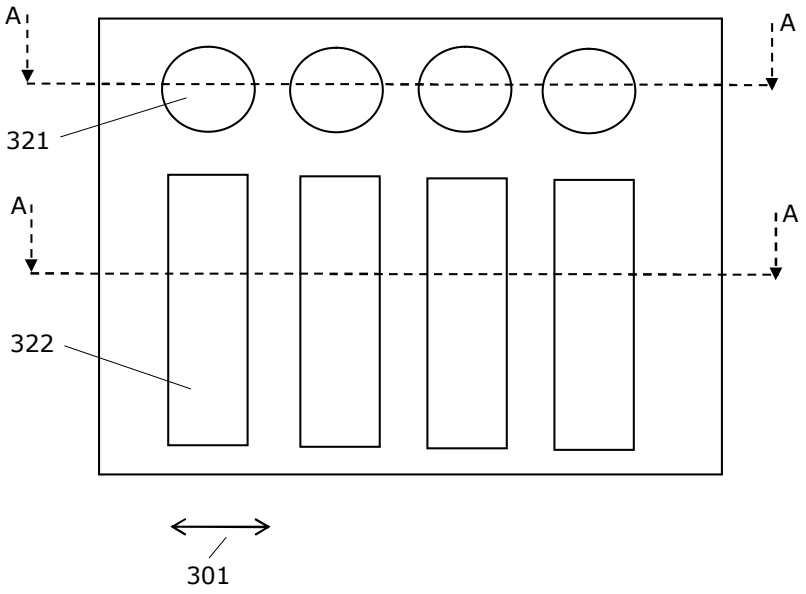

Fig. 3B

4/5

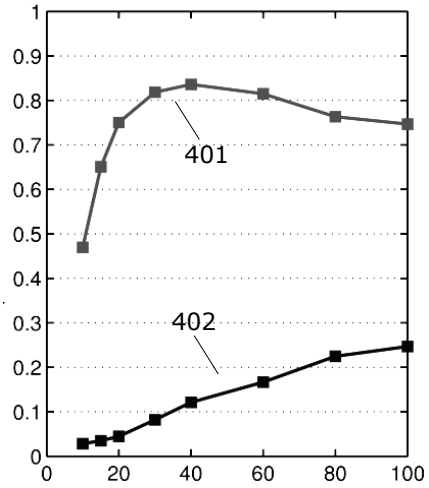

Fig. 4A

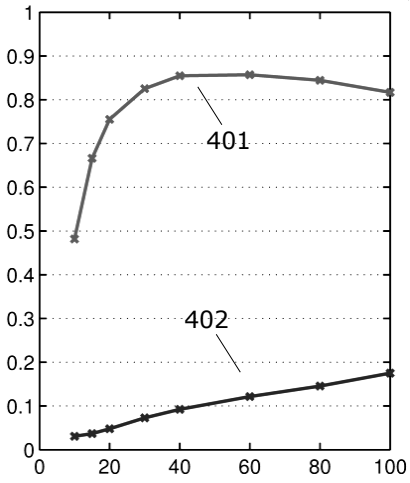

Fig. 4B

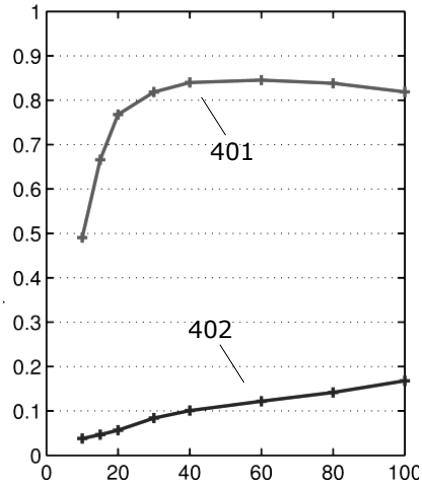

Fig. 4C

5/5

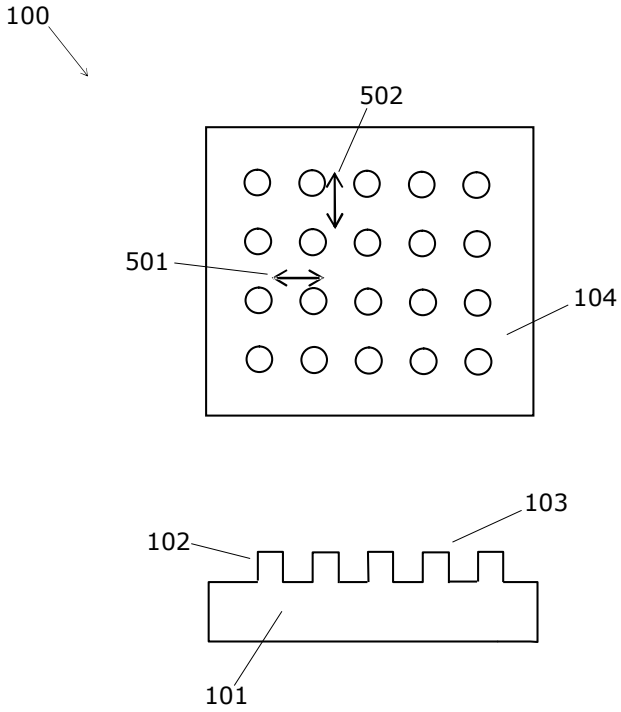

Fig. 5

7

Conclusion

The optical properties of nanostructured dielectric and metallic surfaces have been studied. Focusing on scalable fabrication methods for antireflective nanostructures, large area demonstrators have been shown, which show the dramatic impact that nanostructures can have on the optical properties of both dielectric and metal surfaces.

The investigated nanostructures have for the most part been fabricated using the black silicon (BSi) method; mask less reactive ion etching that result in large areas of nanostructured surfaces. The BSi structures where replicated into the dielectric material Ormocomp, using PDMS stamps for casting structures with lateral size in the micron range, and Ormocomp stamps for casting structures with lateral sizes below 1 μm. Two different regimes of BSi structures have been found; when the lateral size of the structures is in the micron range, the structures heavily scatter visible light. When the lateral size of the structures is below 160 nm, the structures show insignificant scattering of light in the visible range.

The larger BSi structures can in some cases show selective scattering of transmitted light, so that they work as structural colour filters for specularly transmitted light. The transmitted colour will depend on the size and shape of the BSi structures.

BSi structures with a lateral spacing less than 160 nm will show insignificant scattering of visible light. Such structures can therefore be used as antireflective structures. A relation between the lateral size of the structures, and the wavelength below which the scattering was insignificant, was found empirically. This relation can be used as a design parameter for randomly structured, non-scattering antireflective nanostructures. The relation was compared to the minimum period required for zero'th order diffraction, in periodic gratings. The results showed that compared to periodic structures, the random structures require a significantly smaller structural spacing to avoid scattering. For periodic structures, the condition for zero'th order diffraction of light with a wavelength of 500 nm is a period of around 300 nm for transmitted light at normal incidence on a polymer surface, while the characteristic spacing of random structures should be below 160 nm. This presents a trade-off; BSi structures are a cheap way of nanostructuring the masters, but require a better resolution of the methods used to produce the injection moulding tools, and of the injection moulding process itself, compared to using periodic structures.

Antireflective BSi nanostructures were injection moulded in polypropylene, from FDTS coated, electroplated Ni shims, using cycle times of 35 seconds. The resulting structures had

a characteristic length scale of 210 nm, and a height of up to 125 nm. The injection moulded structures showed decent antireflective functionality, as the reflectance of polypropylene was decreased from $4.5 \pm 0.5\%$ to $2.5 \pm 0.5\%$ in the visible spectrum. The reduction in reflectance was sufficient for providing a visible effect on the injection moulded parts. The injection moulded samples were compared to Ormocomp replica of the Ni shim used for injection moulding. For the Ormocomp replica the reflectance was reduced from 4% to 1% in the visible spectrum, and the height of the structures was 210 nm. AFM scans of the surfaces were used to calculate the theoretical reflectance of the structures using effective medium theory. The measured and calculated spectra showed good agreement, and suggest that if the filling of nanostructures during injection moulding could be increased, the antireflective effect could be increased further.

Binary antireflective nanostructures were fabricated from an Si master that was fabricated using fast e-beam lithography. With the fast e-beam lithography method it was possible to achieve a writing time of approximately 2 hours/cm^2. When replicated into Ormocomp, the structures showed a decrease in reflectance from 4% to between 0.5% at 400 nm wavelength, to 2% at 700 nm wavelength. Results from AFM data of the surface showed that the volume fraction profile was similar to an 8th order super-Gaussian geometry. The measured reflectance, and theoretical reflectance calculated from AFM data using effective medium theory showed very similar results. Binary structures could prove to be interesting for injection moulding as they require a lower structure height, compared to gradient type AR structures. Theoretical results showed that an 8th order super-Gaussian structure would have optimum AR properties when the height is roughly 125 nm, with a reflectance lower than 1% in the visible spectrum. The height of gradient AR structures should be around 280 nm for visible light.

Finally, the deposition of thin metal films on nanostructured surfaces was studied. When a 100 nm Al film was deposited on BSi structures in Ormocomp, the reflectance of the Ormocomp-metal interface was reduced from 80% to 6%, and the absorbance increased from 20% to over 90%. In contrast to their reflective planar counterparts, these metal thin films appeared completely black. The results indicate that the nanostructures should have heights in the range 400-600 nm, and the characteristic length scale of the nanostructures should be 150-200 nm. These ranges could possibly be extended though. Furthermore, the structures should be tapered, and closely packed. Demonstrators were shown using both e-beam vapour deposition, and industrial sputter deposition of Al films. The results were similar although small variations in the optical properties were observed, due to the different deposition techniques. Two effects causing the increased absorption were suggested: a gradient effect, causing the metal film to be antireflective, and that the structured surface allows for coupling to surface plasmons in the metal film.

8

Outlook

Injection moulding from Ni shims was shown as a viable method for fabricating antireflective nanostructures. It proved challenging however to achieve good filling of the nanostructured moulds. The process could possibly be improved further by the use of vacuum, or by using varied temperature processes.

Binary AR nanostructures require a lower height than gradient type AR structures, and could therefore be well suited for production processes such as injection moulding. The masters for binary AR structures could possibly be fabricated inexpensively by anodization of aluminium foils to form APA nanostructures. Both the volume fraction and the structure height of APA structures can be controlled in the anodization process, providing good possibilities for optimizing the AR structures.

The use of BSi masters allowed for realizing black metal thin films over large areas. However, the random nature of the BSi process makes it difficult to gain a deeper understanding of the physics of the system, and the different geometrical parameters' influence on the effect. In order to further understand how the structures influence the effect, it would be useful to fabricate well defined structures e.g. using EBL or fast EBL. Tapered structures could be realized by using a RIE process with a low selectivity to the etch mask, so that the masked area decreases during the etching process. In this way it would be possible to fabricate nanostructures that somewhat resemble those of BSi, but with well defined height, period and structure density. This might give more insight into the structures' effect on deposited metal thin films.

Anodic porous alumina is a viable technology for further reducing fabrication costs for some of the applications which were discussed in this thesis, and is a technique which is already used widely in the industry. As discussed above, APA with a uniform porosity could be used for masters for binary type AR structures. APA processes can also be tuned to give gradient porous structures. Gradient APA structures could possibly be used for fabricating gradient type AR structures, and the black metal films discussed in this thesis. In this way, black metal films could be produced by three industrial processes; anodization, injection moulding (or another moulding process), and metal sputter deposition.

Another possibility for large volume production of AR nanostructures, and black metal films could be the use of roll-to-roll systems. Utilizing UV curing in the the R2R system give the possibility for achieving the resolution and replication fidelity needed for the nanostructures discussed in this thesis. If metal deposition could be incorporated in the roll-to-roll machine, black metal films could be manufactured, possibly in combination with plasmonic structural colours.

Bibliography

[1] C. G. Bernhard and W. H. Miller, "A Corneal Nipple Pattern in Insect Compound Eyes," Acta Physiol. Scand. **56**, 385–386 (1962).

[2] C. Bernhard, "Structural and functional adaptation in a visual system," Endeavour **26**, 79 (1967).

[3] P. Clapham and M. Hutley, "Reduction of lens reflexion by the "Moth Eye" principle," Nature **244**, 281–282 (1973).

[4] S. Kinoshita, S. Yoshioka, and K. Kawagoe, "Mechanisms of structural colour in the Morpho butterfly: cooperation of regularity and irregularity in an iridescent scale." Proc. Biol. Sci. **269**, 1417–21 (2002).

[5] P. Vukusic and J. R. Sambles, "Photonic structures in biology," Nature **424**, 852–5 (2003).

[6] S. Kinoshita, S. Yoshioka, and J. Miyazaki, "Physics of structural colors," Reports Prog. Phys. **71**, 076401 (2008).

[7] K. Chung, S. Yu, C.-J. Heo, J. W. Shim, S.-M. Yang, M. G. Han, H.-S. Lee, Y. Jin, S. Y. Lee, N. Park, and J. H. Shin, "Flexible, angle-independent, structural color reflectors inspired by morpho butterfly wings," Adv. Mater. **24**, 2375–9 (2012).

[8] C. Ribot, M.-S. L. Lee, S. Collin, S. Bansropun, P. Plouhinec, D. Thenot, S. Cassette, B. Loiseaux, and P. Lalanne, "Broadband and Efficient Diffraction," Adv. Opt. Mater. **1**, 489–493 (2013).

[9] L. Cao, P. Fan, E. S. Barnard, A. M. Brown, and M. L. Brongersma, "Tuning the color of silicon nanostructures." Nano Lett. **10**, 2649–54 (2010).

[10] J. Walia, N. Dhindsa, M. Khorasaninejad, and S. S. Saini, "Color Generation and Refractive Index Sensing Using Diffraction from 2D Silicon Nanowire Arrays," Small **10**, 144–51 (2014).

[11] T. Ebbesen, H. Lezec, H. Ghaemi, T. Thio, and P. Wolff, "Extraordinary optical transmission through sub-wavelength hole arrays," Nature **86**, 1114–7 (1998), arXiv:0008204 [cond-mat] .

[12] K. Kumar, H. Duan, R. S. Hegde, S. C. W. Koh, J. N. Wei, and J. K. W. Yang, "Printing colour at the optical diffraction limit." Nat. Nanotechnol. **7**, 557–61 (2012).

[13] T. Okuno, "Development of Subwavelength Structure Coating (SWC) and its application to imaging lenses," in *Int. Opt. Des. Conf. Opt. Fabr. Test.*, 1, edited by J. Bentley, A. Gupta, and R. N. Youngworth (2010) p. IMA2.

[14] R. Brunner, O. Sandfuchs, C. Pacholski, C. Morhard, and J. Spatz, "Lessons from nature: biomimetic subwavelength structures for high-performance optics," Laser Photon. Rev. **6**, 641–659 (2012).

[15] K. Tadanaga, N. Katata, and T. Minami, "Formation Process of Super-Water-Repellent Al2O3 Coating Films with High Transparency by the Sol-Gel Method," J. Am. Ceram. Soc. **80**, 3213–3216 (1997).

[16] A. Isurugi, K. Minoura, T. Taguchi, and T. Imaoku, "Die for motheye, and method for producing die for moth-eye and moth-eye structure," (2012).

[17] V. Goodship, *Practical guide to injection moulding* (Rapra Technology, 2004).

[18] H. Schift, C. David, M. Gabriel, J. Gobrecht, L. Heyderman, W. Kaiser, S. Köppel, and L. Scandella, "Nanoreplication in polymers using hot embossing and injection molding," Microelectron. Eng. **53**, 171–174 (2000).

[19] N. Gadegaard, S. Thoms, D. S. Macintyre, K. Mcghee, J. Gallagher, B. Casey, and C. D. W. Wilkinson, "Arrays of nano-dots for cellular engineering," Microelectron. Eng. **68**, 162–168 (2003).

[20] H. K. Raut, V. A. Ganesh, A. S. Nair, and S. Ramakrishna, "Anti-reflective coatings: A critical, in-depth review," Energy Environ. Sci. **4**, 3779 (2011).

[21] C.-J. Ting, M.-C. Huang, H.-Y. Tsai, C.-P. Chou, and C.-C. Fu, "Low cost fabrication of the large-area anti-reflection films from polymer by nanoimprint/hot-embossing technology." Nanotechnology **19**, 205301 (2008).

[22] C.-C. Hong, P. Huang, and J. Shieh, "Fabrication of Morphology-Controlled Sub-20-nm Polymer Nanotip and Nanopore Arrays Using an Identical Nanograss Mold," Macromolecules **43**, 7722–7728 (2010).

[23] H. Deniz, T. Khudiyev, F. Buyukserin, and M. Bayindir, "Room temperature large-area nanoimprinting for broadband biomimetic antireflection surfaces," Appl. Phys. Lett. **99**, 183107 (2011).

[24] U. Schulz, P. Munzert, and N. Kaiser, "Plasma Surface Modification of PMMA for Optical Applications," J. Adhes. Sci. Technol. **24**, 1283–1289 (2010).

[25] K. Park, H. Choi, C. Chang, R. Cohen, G. McKinley, and G. Barbastathis, "Nanotextured silica surfaces with robust superhydrophobicity and omnidirectional broadband supertransmissivity," ACS Nano **6**, 3789–3799 (2012).

[26] H. S. Jang, J. H. Kim, K. S. Kim, G. Y. Jung, J. J. Lee, and G. H. Kim, "Improvement of Transmittance by Fabricating Broadband Subwavelength Anti-Reflection Structures for Polycarbonate," J. Nanosci. Nanotechnol. **11**, 291–295 (2011).

[27] Y. Kanamori, M. Okochi, and K. Hane, "Fabrication of antireflection subwavelength gratings at the tips of optical fibers using UV nanoimprint lithography." Opt. Express **21**, 322–8 (2013).

[28] C. David, P. Häberling, M. Schnieper, J. Söchtig, and C. Zschokke, "Nano-structured anti-reflective surfaces replicated by hot embossing," Microelectron. Eng. **61-62**, 435–440 (2002).

[29] Optics Balzers, "Optics Balzers," (2014).

[30] D. Lehr, M. Helgert, M. Sundermann, C. Morhard, C. Pacholski, J. P. Spatz, and R. Brunner, "Simulating different manufactured antireflective sub-wavelength structures considering the influence of local topographic variations," Opt. Express **18**, 333–342 (2010).

[31] A. Y. Vorobyev and C. Guo, "Direct femtosecond laser surface nano/microstructuring and its applications," Laser Photon. Rev. **7**, 385–407 (2013).

[32] A. Vorobyev and C. Guo, "Effects of nanostructure-covered femtosecond laser-induced periodic surface structures on optical absorptance of metals," Appl. Phys. A **86**, 321–324 (2006).

[33] A. Y. Vorobyev and C. Guo, "Femtosecond laser blackening of platinum," J. Appl. Phys. **104**, 053516 (2008).

[34] A. Y. Vorobyev and C. Guo, "Colorizing metals with femtosecond laser pulses," Appl. Phys. Lett. **92**, 041914 (2008).

[35] A. Y. Vorobyev and C. Guo, "Antireflection effect of femtosecond laser-induced periodic surface structures on silicon." Opt. Express **19, No. S5**, A1031–6 (2011).

[36] G. Tang, A. C. Hourd, and A. Abdolvand, "Nanosecond pulsed laser blackening of copper," Appl. Phys. Lett. **101**, 231902 (2012).

[37] P. Fan, M. Zhong, L. Li, T. Huang, and H. Zhang, "Rapid fabrication of surface micro/nano structures with enhanced broadband absorption on Cu by picosecond laser," Opt. Express **21**, 11628–11637 (2013).

[38] T. Søndergaard, S. M. Novikov, T. Holmgaard, R. L. Eriksen, J. Beermann, Z. Han, K. Pedersen, and S. I. Bozhevolnyi, "Plasmonic black gold by adiabatic nanofocusing and absorption of light in ultra-sharp convex grooves." Nat. Commun. **3**, 969 (2012).

[39] T. Søndergaard and S. I. Bozhevolnyi, "Theoretical analysis of plasmonic black gold: periodic arrays of ultra-sharp grooves," New J. Phys. **15**, 013034 (2013).

[40] Y.-J. Jen, A. Lakhtakia, M.-J. Lin, W.-H. Wang, H.-M. Wu, and H.-S. Liao, "Metal/dielectric/metal sandwich film for broadband reflection reduction." Sci. Rep. **3**, 1672 (2013).

[41] S.-H. Cho, M.-K. Seo, J.-H. Kang, J.-K. Yang, K. Sung-Yong, L. Yong-Hee, H. KyuHwan, L. ByoungDuk, L. Joon-Gu, S. Young-Woo, and L. JongHyuk, "A Black Metal-dielectric Thin Film for High-contrast Displays," J. Korean Phys. Soc. **55**, 501 (2009).

[42] C.-J. Ting, C.-F. Chen, and C. Chou, "Subwavelength structures for broadband antireflection application," Opt. Commun. **282**, 434–438 (2009).

[43] C.-J. Ting, C.-F. Chen, and C.-J. Hsu, "Heat-insulation film with gold layer deposited on antireflection subwavelength-structured surface," Opt. - Int. J. Light Electron Opt. **121**, 1877–1880 (2010).

[44] C.-J. Ting, C.-J. Hsu, Y.-Y. Nieh, and C.-P. Chou, "Nanostructure optical insulating membrane," (2008).

[45] C. J. Ting, H. Y. Tsai, C. P. Chou, H. Y. Lin, and T. C. Wu, "Optical characteristics of silver film on the moth-eye structure," J. Mech. Sci. Technol. **21**, 1752–1755 (2007).

[46] C. Ting, C. Chen, and C. Chou, "Experimental study of a silver layer on an antireflection subwavelength-structured surface," Photonics Technol. Lett. ... **20**, 1196–1198 (2008).

[47] J.-H. Choi, S.-J. Park, J.-H. Lee, C.-H. Kim, J.-H. Jeong, D.-G. Choi, E.-S. Lee, and J.-R. Jeong, "Imprinted Pattern Profile-Dependent Optical Properties of Metal Nanostructures," Jpn. J. Appl. Phys. **51**, 06FJ02 (2012).

[48] F. L. Pedrotti, L. M. Pedrotti, and L. S. Pedrotti, *Introduction to optics*, 3rd ed. (Pearson Prentice Hall, 2007).

[49] M. Born and E. Wolf, *Principles of optics: electromagnetic theory of propagation, interference and diffraction of light* (Oxford, Pergamon Press, 1964).

[50] D. H. Raguin and G. M. Morris, "Analysis of antireflection-structured surfaces with continuous one-dimensional surface profiles." Appl. Opt. **32**, 2582–98 (1993).

[51] P. Jepsen, B. Fischer, A. Thoman, H. Helm, J. Suh, R. Lopez, and R. Haglund, "Metal-insulator phase transition in a VO2 thin film observed with terahertz spectroscopy," Phys. Rev. B **74**, 205103 (2006).

[52] P. Roussel, J. Vanhellemont, and H. Maes, "Numerical aspects of the implementation of effective-medium approximation models in spectroscopic ellipsometry regression software," Thin Solid Films **234**, 423–427 (1993).

[53] S. Bosch, J. Ferré-Borrull, N. Leinfellner, and A. Canillas, "Effective dielectric function of mixtures of three or more materials: a numerical procedure for computations," Surf. Sci. **453**, 9–17 (2000).

[54] IEEE, "IEEE Standard Definitions of Terms for Radio Wave Propagation," IEEE Std 211-1997 (1998), 10.1109/IEEESTD.1998.87897.

[55] TOPAS Advanced Polymers, "TOPAS," .

[56] N. Gadegaard, S. Mosler, and N. B. Larsen, "Biomimetic Polymer Nanostructures by Injection Molding," Macromol. Mater. Eng. **288**, 76–83 (2003).

[57] G. Khanarian, "Optical properties of cyclic olefin copolymers," Opt. Eng. **40**, 1024 (2001).

[58] KJ Innovation, "GD-Calc," (2008).

[59] MathWorks, "Matlab," .

[60] S. A. Maier, *Plasmonics: fundamentals and applications* (Springer, 2007).

[61] A. D. Rakić, "Algorithm for the determination of intrinsic optical constants of metal films: application to aluminum." Appl. Opt. **34**, 4755–67 (1995).

[62] G. Hass and J. E. Waylonis, "Optical Constants and Reflectance and Transmittance of Evaporated aluminum in the visible and ultraviolet," J. Opt. Soc. Am. **51**, 719–722 (1961).

[63] H. Jansen, M. D. Boer, R. Legtenberg, and M. Elwenspoek, "The black silicon method: a universal method for determining the parameter setting of a fluorine-based reactive ion etcher in deep silicon trench etching with profile control," J. Micromechanics Microengineering **5**, 115–120 (1995).

[64] M. Schnell, R. Ludemann, and S. Schaefer, "Plasma surface texturization for multicrystalline silicon solar cells," Conf. Rec. Twenty-Eighth IEEE Photovolt. Spec. Conf. - 2000 (Cat. No.00CH37036) , 367–370 (2000).

[65] G. Kumaravelu, M. M. Alkaisi, and A. Bittar, "Surface texturing for silicon solar cells using reactive ion etching technique," Photovolt. Spec. Conf. 2002. Conf. Rec. Twenty-Ninth IEEE , 258–261 (2002).

[66] S. Schröder, A. Duparré, L. Coriand, A. Tünnermann, D. H. Penalver, and J. E. Harvey, "Modeling of light scattering in different regimes of surface roughness." Opt. Express **19**, 9820–35 (2011).

[67] H. Yoshida, Y. Terada, H. Miyake, and K. Hiramatsu, "Antireflection Effect of Self-Organized GaN Nanotip Structure from Ultraviolet to Visible Region," Jpn. J. Appl. Phys. **41**, L1134–L1136 (2002).

[68] J. R. Taylor, *An introduction to error analysis*, 2nd ed. (University Science Books, 1997).

[69] Microresist Technology GmbH, Berlin, Germany, www.microresist.de.

[70] S. Obi, *Replicated optical microstructures in hybrid polymers:process technology and applications*, Phd thesis, University of Neuchâtel (2006).

[71] M. B. Christiansen, *Nanostructured polymer dye lasers*, Phd thesis, Technical University of Denmark (2009).

[72] K.-H. Haas and H. Wolter, "Synthesis , properties and applications of inorganic - organic copolymers," Curr. Opin. Solid State Mater. Sci. **4**, 571–580 (1999).

[73] H. Takemura, H. Ohki, and H. Nakazawa, "Performance of new E-beam lithography system JBX-9300FS," Microelectron. Eng. **53**, 329–332 (2000).

[74] K. Suzuki, *Microlithography: science and technology* (CRC, 2007).

[75] E. Højlund-Nielsen, T. Greibe, N. A. Mortensen, and A. Kristensen, "Single-spot e-beam lithography for defining large arrays of nano-holes," Microelectron. Eng. **in press** (2014).

[76] Ocean Optics, www.oceanoptics.com.

[77] J. Clausen, A. B. Christiansen, J. Garnaes, N. A. Mortensen, and A. Kristensen, "Color effects from scattering on random surface structures in dielectrics." Opt. Express **20**, 4376–81 (2012).

[78] A. B. Christiansen, J. Clausen, N. A. Mortensen, and A. Kristensen, "Minimizing scattering from antireflective surfaces replicated from low-aspect-ratio black silicon," Appl. Phys. Lett. **101**, 131902 (2012).

[79] A. B. Christiansen, E. Højlund-Nielsen, J. Clausen, G. P. Caringal, N. A. Mortensen, and A. Kristensen, "Imprinted and injection-molded nano-structured optical surfaces," in *Proc. SPIE 8818, Nanostructured Thin Film. VI*, Vol. 8818, edited by T. G. Mackay, A. Lakhtakia, Y.-J. Jen, and M. Suzuki (2013) p. 881803.

[80] A. B. Christiansen, J. S. Clausen, N. A. Mortensen, and A. Kristensen, "Injection moulding antireflective nanostructures," Microelectron. Eng. (2014), http://dx.doi.org/10.1016/j.mee.2014.03.027.

[81] S. N. Kasarova, N. G. Sultanova, C. D. Ivanov, and I. D. Nikolov, "Analysis of the dispersion of optical plastic materials," Opt. Mater. (Amst). **29**, 1481–1490 (2007).

[82] ToolPartners A/S, www.toolpartners.com.

[83] The Lego Group, www.lego.com.

[84] Y.-T. Yoon, H.-S. Lee, S.-S. Lee, S. H. Kim, J.-D. Park, and K.-D. Lee, "Color filter incorporating a subwavelength patterned grating in poly silicon." Opt. Express **16**, 2374–80 (2008).

[85] H.-S. Lee, Y.-T. Yoon, S.-S. Lee, S.-H. Kim, and K.-D. Lee, "Color filter based on a subwavelength patterned metal grating." Opt. Express **15**, 15457–63 (2007).

[86] Y. Kanamori, M. Shimono, and K. Hane, "Fabrication of Transmission Color Filters Using Silicon Subwavelength Gratings on Quartz Substrates," IEEE Photonics Technol. Lett. **18**, 2126–2128 (2006).

[87] Y. Ye, Y. Zhou, H. Zhang, and L. Chen, "Polarizing color filter based on a subwavelength metal-dielectric grating." Appl. Opt. **50**, 1356–63 (2011).

[88] C. Genet and T. W. Ebbesen, "Light in tiny holes," Nature **445**, 39–46 (2007).

[89] X. Hu, L. Zhan, and Y. Xia, "Color filters based on enhanced optical transmission of subwavelength-structured metallic film for multicolor organic light-emitting diode display." Appl. Opt. **47**, 4275–9 (2008).

[90] R. Leitel, A. Kaless, U. Schulz, and N. Kaiser, "Broadband Antireflective Structures on PMMA by Plasma Treatment," Plasma Process. Polym. **4**, S878–S881 (2007).

[91] I. Wendling, P. Munzert, U. Schulz, N. Kaiser, and A. Tünnermann, "Creating Anti-Reflective Nanostructures on Polymers by Initial Layer Deposition before Plasma Etching," Plasma Process. Polym. **6**, S716–S721 (2009).

[92] H. Schift and A. Kristensen, "Nanoimprint lithography - patterning of resists using molding," in *Springer Handb. Technol.*, edited by B. Bhushan (Springer, Berlin, Heidelberg, 2010) pp. 271–312.

[93] L. Sainiemi, V. Jokinen, A. Shah, M. Shpak, S. Aura, P. Suvanto, and S. Franssila, "Non-reflecting silicon and polymer surfaces by plasma etching and replication." Adv. Mater. **23**, 122–6 (2011).

[94] S. Aura, V. Jokinen, L. Sainiemi, M. Baumann, and S. Franssila, "UV-Embossed Inorganic-Organic Hybrid Nanopillars for Bioapplications," J. Nanosci. Nanotechnol. **9**, 6710–6715 (2009).

[95] D. Dominé, F.-J. Haug, C. Battaglia, and C. Ballif, "Modeling of light scattering from micro- and nanotextured surfaces," J. Appl. Phys. **107**, 044504 (2010).

[96] J. Harvey, "Fourier treatment of near-field scalar diffraction theory," Am. J. Phys. **47**, 974 (1979).

[97] J. E. Harvey, C. L. Vernold, a. Krywonos, and P. L. Thompson, "Diffracted radiance: a fundamental quantity in nonparaxial scalar diffraction theory." Appl. Opt. **38**, 6469–81 (1999).

[98] E. B. Grann, M. G. Moharam, and D. A. Pommet, "Artificial uniaxial and biaxial dielectrics with use of two-dimensional subwavelength binary gratings," J. Opt. Soc. Am. A **11**, 2695 (1994).

[99] A. R. Parker and H. E. Townley, "Biomimetics of photonic nanostructures." Nat. Nanotechnol. **2**, 347–53 (2007).

[100] P. Vukusic, J. R. Sambles, and C. R. Lawrence, "Colour mixing in wing scales of a butterfly." Nature **404**, 457 (2000).

[101] R. Stephens and G. Cody, "Optical reflectance and transmission of a textured surface," Thin Solid Films **45**, 19–29 (1977).

[102] Y. Kanamori, M. Sasaki, and K. Hane, "Broadband antireflection gratings fabricated upon silicon substrates." Opt. Lett. **24**, 1422–4 (1999).

[103] R. O. Prum, T. Quinn, and R. H. Torres, "Anatomically diverse butterfly scales all produce structural colours by coherent scattering," J. Exp. Biol. **209**, 748–65 (2006).

[104] G. Bao, D. Dobson, and K. Ramdani, "A constraint on the maximum reflectance of rapidly oscillating dielectric gratings," SIAM J. Control Optim. **40**, 1858–1866 (2002).

[105] J. E. Stewart and W. S. Gallaway, "Diffraction Anomalies in Grating Spectrophotometers," Appl. Opt. **1**, 421 (1962).

[106] A. Hessel and A. A. Oliner, "A New Theory of Wood's Anomalies on Optical Gratings," Appl. Opt. **4**, 1275 (1965).

[107] M. Neviere and E. Popov, *Light Propagation in Periodic Media: Differential Theory and Design*, 1st ed. (CRC Press, 2002) p. 432.

[108] T. Smith and J. Guild, "The C.I.E. colorimetric standards and their use," Trans. Opt. Soc. **33**, 73 (1931).

[109] J. J. Vos, "Colorimetric and Photometric Properties of a 2 Deg Fundamental Observer," Color Res. Appl. **3**, 125–128 (1978).

[110] D. Judd, D. MacAdam, and G. Wyszecki, "Spectral distribution of typical daylight as a function of correlated color temperature," J. Opt. Soc. Am. **54**, 1031–1040 (1964).

[111] M. Stokes, M. Anderson, S. Chandrasekar, and R. Motta, "A Standard Default Color Space for the Internet - sRGB," (1996).

[112] S.-I. Chang, J.-B. Yoon, H. Kim, J.-J. Kim, B.-K. Lee, and D. H. Shin, "Microlens array diffuser for a light-emitting diode backlight system." Opt. Lett. **31**, 3016–8 (2006).

[113] C. Kurtz, "Transmittance characteristics of surface diffusers and the design of nearly band-limited binary diffusers," J. Opt. Soc. Am. **62**, 982–989 (1972).

[114] I. Saarikoski, M. Suvanto, and T. A. Pakkanen, "Modification of polycarbonate surface properties by nano-, micro-, and hierarchical micro-nanostructuring," Appl. Surf. Sci. **255**, 9000–9005 (2009).

[115] J. S. Clausen, A. B. Christiansen, A. Kristensen, and N. A. Mortensen, "Enhancing the chroma of pigmented polymers using antireflective surface structures," Appl. Opt. **52**, 7832–7 (2013).

[116] E. Grann, M. Varga, and D. Pommet, "Optimal design for antireflective tapered two-dimensional subwavelength grating structures," J. Opt. Soc. Am. A **12**, 333–339 (1995).

[117] Y. Zhang, C. Li, and M. Loncar, "Optimal broadband antireflective taper." Opt. Lett. **38**, 646–8 (2013).

[118] S. Hattori, K. Nagato, T. Hamaguchi, and M. Nakao, "Rapid injection molding of high-aspect-ratio nanostructures," Microelectron. Eng. **87**, 1546–1549 (2010).

[119] Y. Yoo, T. Kim, D. Choi, S. Hyun, H. Lee, K. Lee, S. Kim, B. Kim, Y. Seo, H. Lee, and J. Lee, "Injection molding of a nanostructured plate and measurement of its surface properties," Curr. Appl. Phys. **9**, e12–e18 (2009).

[120] M. Matschuk and N. B. Larsen, "Injection molding of high aspect ratio sub-100 nm nanostructures," J. Micromechanics Microengineering **23**, 025003 (2013).

[121] Nanosensors, Neuchatel, Switzerland, www.nanosensors.com.

[122] Image Metrology, "Scanning Probe Imaging Processor software, SPIP," (2013).

[123] Axxicon, www.axxicon.com.

[124] Nanonics Imaging Ltd., Jerusalem, Israel, www.nanonics.co.il.

[125] Centro Ricerche FIAT, www.crf.it.